A METHOD FOR MEASURING INTRUSION INTO CEMENTITIOUS MATERIALS CONTAINING PARAMAGNETIC SUBSTANCES USING μCT WITH A CONTRAST AGENT

By

Patrick Michael Marine

Thesis

Submitted to the Faculty of the

Graduate School of Vanderbilt University

in partial fulfillment of the requirements

for the degree of

MASTER OF SCIENCE

in

Physics and Astronomy

August, 2009

Nashville, Tennessee

Approved:

Professor Michael Stabin

Professor Andrew Garrabrants

To my sweet pea who gave me the opportunity to embrace this endeavor

even though it caused her much grief.

To my faithful animals, Jasmine, Bear, and Samuel

who provided me unconditional love when I really needed it.

and

To Jake and Nightshade

who started this journey with me but passed along the way.

ACKNOWLEDGEMENTS

This work would not have been possible without financial support from the Consortium for Risk Evaluation with Stakeholder Participation (CRESP) and the Cementitious Barrier Project. I am grateful to the staff of the Vanderbilt Civil and Environmental Engineering Department most notably to Dr. James Clarke, Dr. Mark Abkowitz, Dr. Frank Parker, Dr. Andrew Garrabrants and Dr. David Kosson. I am also indebted to my colleague and partner Joshua Arnold whose patience and teaching allowed me to have a firmer grasp on concepts relating to cementitious materials and transport phenomena. Lastly I am grateful to Dr. Michael Stabin Associate Professor of Radiological Sciences at Vanderbilt who mentored me over the last two years, held me to a high standard, and made me feel like a welcome part of the health physics community.

"We exist in a storm of energy, of particles so fine and waves so subtle that we can't perceive them. They rain down from the sky and well up from rocks and dirt, from the desert floor and from the remotest of canyon walls. Radioactive minerals wash into rivers and oceans and concentrate in the seabed; they turn up in yogurt, wheat germ, granola, acorn squash, oranges and soy protein. To avoid radiation, you would have to leave your own body and you would have to leave the universe."[1]

Gwyneth Cravens, Power to Save the World

Figure 1: Aurora borealis by Terry Lutz
Auroras are produced when charged particles originally from the sun interact with atoms and molecules in the earth's upper atmosphere.

TABLE OF CONTENTS

LIST OF TABLES

LIST OF FIGURES

CHAPTER I

INTRODUCTION

In the short fifty years between the discovery of natural radiation and the dropping of the bombs on Hiroshima and Nagasaki mankind has used radionuclides for everything from miracle cures and health enhancers to glow in the dark watch dials[2]. The discovery of x-rays by Roentgen in 1895 quickly revolutionized the practice of medicine [3]. For the first time physicians could use x-ray images to assist in setting broken bones, ensure wounds were completely free of shrapnel or precisely place pins or radioactive seeds inside the body with minimal intrusion. They could detect kidney stones, and diagnose cirrhotic livers [3]. X-rays provided for verification of proper care in many instances and allowed exploration without breaking the protective skin barrier. Bequerrel's discovery of radioactivity in 1896 was no less significant and led to the use of radionuclides in multiple fields not the least of which was in nuclear medicine [4]. This is evidenced by the fact that 16.9 million nuclear medicine procedures were performed in the U.S alone in 2001[5].

This rapid use of a young technology occurred without fully understanding its dangers or how radionuclides interacted with the human body if ingested or inhaled. In the case of early nuclear weapons production which generated a large percentage of our legacy waste, the drive to produce a nuclear weapon in a wartime situation was the

overriding goal and other factors, such as waste storage or long term health affects while not ignored were of secondary importance[6].

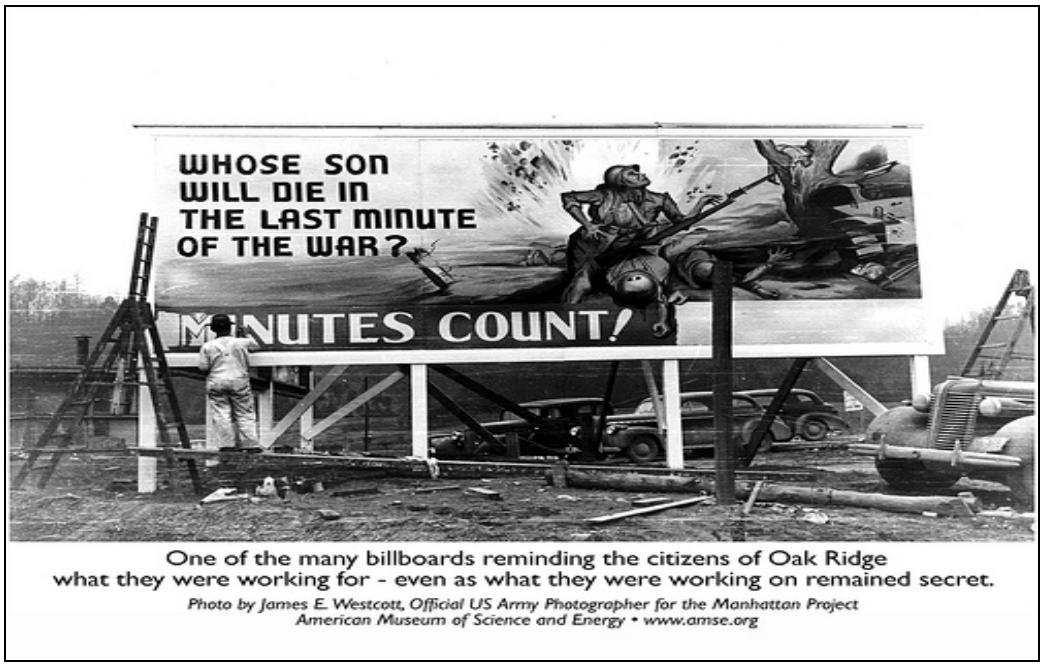

Figure 2: Oak Ridge Billboard

In the early years, radiation and radioactive materials were used in a lax manner by some and were often viewed as a harmless curiosity by the public. This was not because experts did not recognize the need for protection and regulation however. Early on there was an acknowledgement of the need for radiation protection standards and in "1913 the German Radiological Society on X-ray protection outlined nine steps for protection of radiologists from radiation injury."[7] Later in the early 1920s the British X-ray and Radium Protection Committee published a more comprehensive set of protection recommendations. These recommendations are credited as being the 1st comprehensive set of radiation protection documents[7]. Organization and cooperation grew and in 1928 the International Committee on X-ray and Radium Protection was organized. This group later became known as the International Commission on Radiological Protection[7]. While

this group is an advisory group and holds no official regulatory power its recommendations are respected and often enacted into law in various countries. There was still no principle of Justification Optimization and Limitation (JOL) or As Low as Reasonably Achievable (ALARA) as of yet. The fields of radiation biology, radiation safety and regulation, and risk management were still forming. Professionals in the fields constructed working safety codes and disposal protocols but many lacked sufficient understanding of the risks at hand. The exposure of large populations in Japan to radiation from the bombings of 1945 and studies of medical populations exposed to radiation provided significant amounts of data on the effects of radiation on the human body[8].

During the sixty years after WWII the use of radiation and radionuclides expanded greatly. Advances in medicine, industry gauging and analysis, and the commercial nuclear power fields added to our uses of radionuclides. Regulations and enforcement agencies were put in place, and the use of such technologies became commonplace. Radionuclides are now even in consumer products many have in their homes. For example most smoke detectors still use a sealed americium-241 source to detect smoke particles, and some wear watches with tritium illuminated dials, which are a safer alternative to the older radium dials.

Table 1 presents a timeline of important discoveries, events, and legislation relating to radionuclides and is intended to illustrate key points in the use of radioactive materials.

Table 1: Important dates in radioactive material history	
date	event
1789	Uranium discovered by German Chemist Martin Klaproth while examining pitchblende[4]
1896	Becquerel discovers natural radioactivity using potassium uranium sulfate crystals and photographic plates[4]
1898	Marie Curie discovers Polonium and Radium[9]
1901	Henri Alexandre Danlos and Eugene Bloch place radium in contact with a tuberculous skin lesion[3]
1903	Alexander Graham Bell suggested placing sources containing radium in or near tumors[5]
1904	Wickham and Derias perform brachytherapy using sharpened goose quills to perform intratumoral implantations[10]
1920s	Radium Girls draw world-wide attention to the dangers of ingested radium[11]
1924	Lead-210 and Bismuth-210 used as first radiotracer in animals[5]
1928	International Commission on Radiological Protection established[7]
1932	James Chadwick discovers neutrons[12]
1938	Hahn, Straussman and Meitner discover neutron fission[13]
1939, Sept. 1	Germany invades Poland and WWII begins
1939	Germany begins work on the military use of fission[14]
1941	Saul Hertz delivered the first therapeutic dose of I-130 to a patient[5]
1942	The Manhattan Project becomes active[15]
1942, Dec. 2	Enrico Fermi's group create the first self-sustaining nuclear reaction in a squash court below the University of Chicago's Stagg Field[16]
1943-1945	For the first time large quantities of naturally occurring radioactive elements were concentrated, and new elements created[6]
1945 Aug. 6,9	First nuclear bomb dropped on Hiroshima, second bomb dropped on Nagasaki[17]
Mid 1940s	Cold War begins
1946 Aug.	The Atomic Energy Act of 1946 creates the Atomic Energy Commission (AEC) to control nuclear energy development and explore the peaceful uses of nuclear energy[18]
1948	Abbot laboratories begins to distribute radioisotopes to universities, hospitals and industry[5]
1950-present	Industry uses radioisotopes for a wide variety of reasons including material analysis, gauging, sterilization, quality assurance and process tracing[19]
1951	The USFDA approves sodium iodide I-131 for thyroid patients; this is the first "approved" radiopharmaceutical[5]
1954	Atomic Energy act of 1954 amends the 1946 act and provides for the AEC to license private companies' use of nuclear materials and to build and operate nuclear power plants[20]
1955	First nuclear submarine USS Nautilus SSN 571 begins sea trials[21]

1957	First large scale nuclear power plant built in Shippingport PA, providing power to Pittsburgh and western PA[21]
1957	Group at Brookhaven National Laboratory develop I-132 and Tc-99m generators making short lived radionuclides available at distant sites from the production of the parent generators. These became known as "cows"[5]
1958	Hal Anger invents the scintillation camera[5]
1966	Linear No Threshold model (LNT) endorsed by ICRP after UNSCEAR reports of 1962 and 1964 recommended its use for an upper limit to the risk of low-level exposures[22]
1971	The AMA recognizes nuclear medicine as a specialty[5]
1973	H. William Strauss introduces the exercise stress test myocardial scan[5]
1974	Energy Reorganization Act (P.L 93-438) split the AEC into the Nuclear Regulatory Commission (NRC) and the Energy Research and Development Administration (ERDA). The NRC now was responsible for licensing facilities. The ERDA would later become the Department of Energy (DOE)[23]
1975	ALARA dose limitation concept first introduced in 1954 by the National Council on Radiation Protection (NCRP) is adopted into DOE site operation manuals[24]
1976	Resource Conservation Recovery Act (RCRA) enacted by congress, this provided a cradle to grave tracking of hazardous waste from generation to disposal[25]
1977 Apr. 7	Jimmy Carter indefinitely defers reprocessing and recycling of plutonium produced in the U.S. nuclear power program. This effectively kills the Barnwell SC reprocessing plant under construction[26]
1980	Comprehensive Environmental Response, Compensation and Liability Act (CERCLA) establishes a national program for the cleanup of abandoned, uncontrolled hazardous waste disposal sites. CERCLA was amended in 1986 with the superfund ammendments[27]
1982	The Nuclear Waste Policy Act (NWPA) provides for development of repositories for the disposal of high level waste (HLW), establishes nuclear waste fund[28]
1985	Amended Low Level Radioactive Waste Policy Act gave states the responsibility of disposing low level radioactive waste generated within their borders and allowed them to form regional compacts to serve a group of states[29]
1992	Federal Facilities Compliance Act amended RCRA by requiring all federal agencies to meet the same legal requirements governing pollution prevention and cleanup as private companies[30]
Mid 1990s	Cold war ends, between 1944 and the early 1990s the United States produced 114 tons of plutonium in government reactors at Hanford and the Savannah River site[31]
2001	16.9 million nuclear medicine procedures performed in the United States[5]
2008	806,181,935 MWh generated by U.S. nuclear plants; this is 19.6% of all electricity produced commercially in the U.S.[32]

Selected images corresponding to Table 1

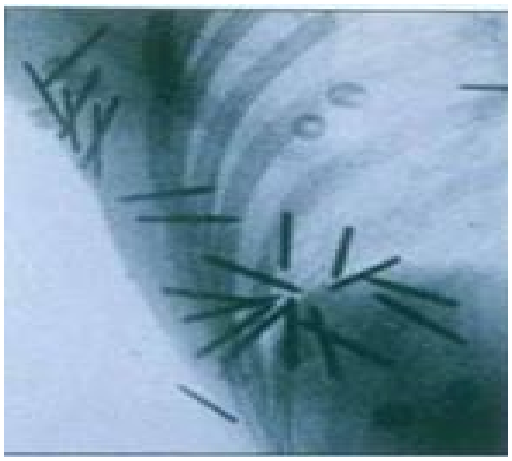

Figure 3: 1920's breast brachytherapy

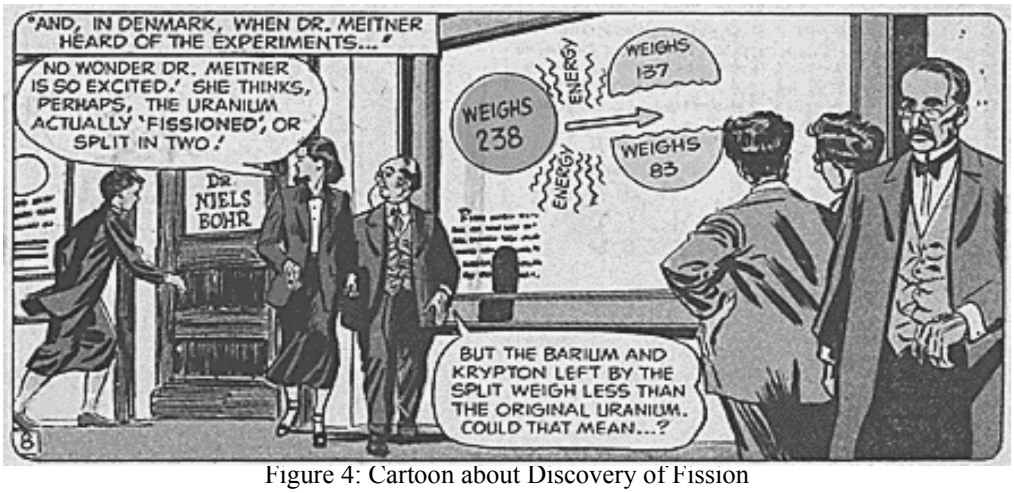

Figure 4: Cartoon about Discovery of Fission

Figure 5: USS Nautilus SSN 571, first nuclear powered submarine

With all these uses of radionuclides, radioactive waste was sure to ensue. The science of control and containment of these wastes has been ongoing and maturing over the last several decades. Cementitious materials are used extensively for encasing radioactive waste (e.g., dry cask storage of spent fuel, or low-level waste vaults), containment (e.g., spent fuel pools or landfill liners and caps) or as an immobilization media in waste treatment. By nature, cementitious materials are created by hydration reactions of pozzolanic binders with water, and properly cured materials exhibit a water-filled pore system. However, during placement or utilization, these materials may lose or gain water from the surrounding environment. The presence of a continuous water phase allows for the release of dissolved ions in the pore solution. In addition, most of the mechanisms that are known to degrade cement-based materials, such as chloride penetration, carbonation, sulfate attack and decalcification, involve the ingress or egress of aggressive ions. Thus, water migration and ionic diffusion into or out of the cementitious barriers are of key concern not only due to possible contaminant escape but also due to destructive processes on concrete support structures.

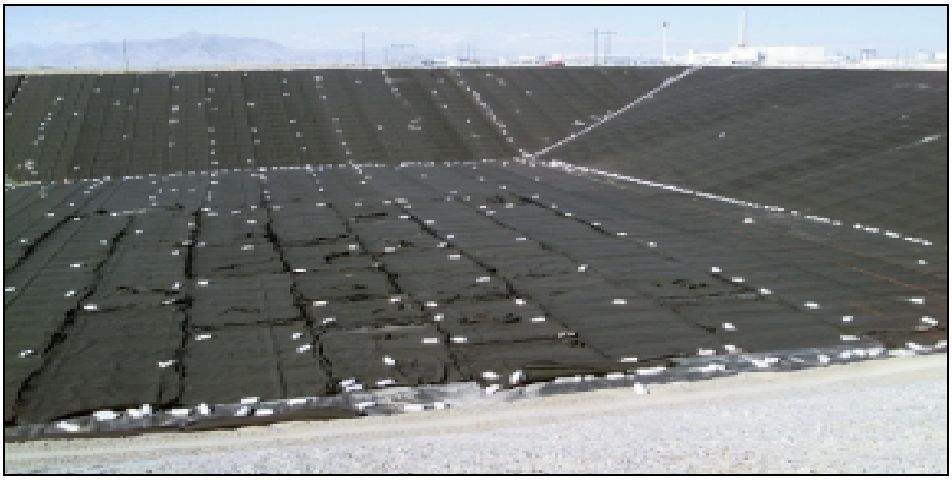

Figure 6: Engineered liner at a CERCLA facility

An ideal intrusion rate determining technique for cementitious materials would:

- allow the reasonably quick determination of intrusion rate for varying cementitious materials
- be cost effective,
- be adapted to quality assurance for batches of materials,
- be able to demonstrate changes in intrusion rate due to carbonation, sulfate attack and other performance degrading conditions,
- require a small footprint,
- be available at multiple locations, and
- be relatively simple to run and interpret (a field tech should be able to perform this analysis)

This investigation will present the development of a practical, inexpensive method to locate solution fronts in various cementitious compounds; with an emphasis on achieving a technique that is implementable with high iron content material. The proposed method uses microComputedTomagraphy (μCT) imaging techniques to identify changes in the material's linear attenuation coefficient (LAC). This change in LAC is associated with the intrusion of water and ionic solutions into the porous material. The location of solution fronts provided by this method can be used as inputs in long-term performance assessment models for cementitious barriers used in radioactive waste management.

CHAPTER II

LITERATURE REVIEW

Types of Radioactive Waste

The DOE defines five main types of nuclear waste[33]. These are:

1. Spent Nuclear Fuel-this is fuel that has been irradiated and removed from a reactor.
2. High-Level Nuclear Waste- this waste is generated from the chemical reprocessing of spent nuclear fuel.
3. Mill Tailings- these are the naturally occurring soil and rock that are byproducts of the uranium mining and milling industry.
4. Transuranic Nuclear Waste- this waste is similar to low-level waste but is contaminated with elements above uranium on the periodic table. These include the elements of neptunium, plutonium, americium, and curium. None of these elements are naturally occurring on our planet and are members of the actinide group. Transuranic waste is almost entirely a product of defense activities.
5. Low-Level Nuclear Waste- this is all other radioactive waste besides spent fuel, high-level waste and transuranic waste.

The United States Nuclear Regulatory Commission (NRC), which regulates the storage and disposal of mainly commercial nuclear wastes, does not have a separate classification for spent fuel and includes spent fuel in their high-level waste category[34].

- Other types of radioactive waste not mentioned above are byproduct material and special nuclear material. Byproduct material is currently regulated by the NRC under the authority of 10 CFR part 30[35].

The definitions of HLW and LLW are not derived directly from the levels of activity or from potential risk to human populations but from the origin of the waste production. As an example medical sources used in High Dose Rate therapy (HDR) to treat cancer patients may be of very high activity, as can blood irradiators used in research[36]. If these sources come into unrestricted contact with the public they could cause significant harm, but are still considered LLW.

Although radioactive wastes are not classified strictly by risk there is an attempt to classify them by hazard level. This is evident by the NRC classification of long lived radioisotopes and short lived radioisotopes in 10CFR61[37]. Since long lived radioisotopes present a hazard (the potential for harm) over a longer time period, they are treated differently than short lived radioisotopes. Yet in many cases short lived radionuclides presents the greater risk (probability of harm occurring). One should not confuse risk and hazard in the technical sense as they are used as distinct concepts in many assessments (Abkowitz M 2009, personal communication 15th May). For example, flying in an airplane is a low risk activity but involves the serious hazard of crashing. Thus in its core form, a hazard is something that has the potential to harm (e.g. flying in an airplane). While risk is the likelihood of the hazard occurring (e.g. the probability the airplane crashes).

Peter Sandman defines risk slightly differently, and breaks risk down into its technical side that he labels hazard, and its remaining influencing factors such as control, trust, dread, voluntariness and responsiveness, which Sandman lumps together and calls 'outrage'[38]. He defines hazard as magnitude times probability (which was previously defined above as risk) but then adds the more subjective component of outrage. Thus to Sandman Risk = Hazard x Outrage[38]. These varying definitions of hazard and risk lead to confusion when discussing imminent danger or the lack thereof, with lay people. The general public understands the concept of imminent danger (e.g. touching a hot stove burner) but is often misinformed of how risk and hazard are used technically and may confuse the concepts as synonyms. These concepts of risk and hazard appear continuously in nuclear waste management where the concept of outrage is a significant factor to consider.

The four classes of low-level radioactive waste according to the NRC are:

1. Class A
2. Class B
3. Class C
4. Greater than Class C

The pamphlet DOE/EM-0195 entitled Low-Level Radioactive Waste Basics[39] describes these classes in the following ways. Class A waste has lower concentrations of radioactivity than classes B and C waste. This waste is mostly composed of discarded clothing, trash, oils, sludges, and biomedical wastes. Class A waste makes up 90 percent of the volume of LLW. This waste is thus high in volume but low in its concentration of radioactivity. Steel drums and plywood boxes are used to contain this waste.

Class B waste is largely composed of materials from nuclear power plants, such as used hardware, filters and purification resins. The concentrations of radioactivity in

this waste are higher than Class A waste. Because of this, Class B waste must be solidified and packaged in "durable" containers that will retain their structural stability and prevent the failure of the disposal unit.

Class C waste is produced in a variety of areas including nuclear power plants, industrial and research activities. This waste may include such materials as sealed radiation sources used in industry or medicine and irradiated reactor parts that contain activation products. Class C waste has higher concentrations of activity and requires engineered barriers to protect from inadvertent intrusion for a minimum of 500 years. "Specially engineered barriers such as concrete caps are placed over the area to prevent the waste from being disturbed"[39].

Greater than Class C low level waste exceeds the limits set by class C but is not high-level waste. "By law, the Federal Government is responsible for disposal of this waste." [28]. The classes of low-level radioactive waste are formally defined in 10CFR 61.55 [37].

Although the NRC does not strictly classify materials by their activity they do take half-life into account when classifying low-level waste[37]. Half-life by definition is the time it takes for half the activity of a radioactive sample to decay away. The NRC divides radionuclides into 2 general groups for LLW waste classification metrics, those with half-lives over 100 years and those with half-lives less than 100 years. The radionuclides included in the long half life category include carbon-14, nickel-59, niobium-94, technetium-99, iodine-129, plutonium-241, and curium-242. In addition to these radionuclides, transuranic alpha emitters with half-lives greater than 5 years are included, as various isotopes of this group may have half-lives of several hundred

thousand years. The short half-life category consists of tritium, cobalt-60, nickel-63, strontium-90, and cesium-137.

A summary of some of the key aspects relating to LLW classification and disposal are presented by Anthony Andrews of the Congressional Research Service in the report entitled "Radioactive Waste Streams: Waste Classification for Disposal[40]." Table 2 below is a condensed recreation of his summary table.

Table 2: Summary of some key features of the LLW classes

	Class A	Class B	Class C	GTCC
Specific Activity	near background to 700 Ci/m^3 (26 TBq/m^3)	0.04 to 700 Ci/ m^3 (1.480 GBq to26 TBq/m^3)	44 to 7000 Ci/m^3 (1.6 to 260 TBq/m^3)	Greater than Class C
Maximum waste concentration basis	100 year decay to acceptable hazard level* to an intruder	100 year decay to acceptable hazard level* to an intruder	100 year decay exceeds acceptable hazard level* to an intruder. 500 year acceptable hazard level reached. 500 year protection provided by deeper disposal or intruder barriers.	Unspecified by regulations.
Waste containers	No special provisions, if waste is buried in a separate disposal cell	Must be designed to be stable for 300 years	Must remain stable for 300 years	Not applicable
Special disposal provisions	Waste stabilization required if buried with Class B or C waste	Not applicable	Barriers to Intrusion required that must remain effective for 500 years where site conditions prevent deeper disposal.	Though generally not deemed acceptable for shallow disposal, regulation does allow for disposal if it is approved by the NRC. Otherwise this waste must be disposed of in a geologic repository.

* acceptable hazard level to an intruder based on the max. annual dose equivalent of 500 mrem (5mSv) to the whole body.

Where Radioactive Waste is Generated

Radioactive waste comes from several major sources including:

1. Hospitals
2. Research facilities, including university, government and private laboratories
3. Industry and Agriculture
4. Nuclear power plants
5. Fuel production, including mining, milling, and enrichment
6. Weapons production waste and naval propulsion waste, which also includes mining milling and enrichment wastes

Hospitals produce a wide range of radioactive waste. These wastes can be classified as radionuclides used for diagnostic/functional imaging or detection, direct therapy, or for use in support instrumentation. For example F-18 in the form of fluorodeoxyglucose (FDG) is used in many metabolic studies as this compound acts as a glucose analog. FDG can also be used in imaging some types of tumors due to their increased glucose uptake. This is an example of functional imaging. Xenon-133 is an example of a radionuclide used in a diagnostic sense and is used to image the lungs and is often used to image blood flow in the brain. Iodine-131 is an example of a use of radionuclide used in therapy. I-131 in the form of sodium iodide is usually introduced by the use of a gelatin pill taken orally. Depending on the dose delivered the radioiodine may correct hyperactive thyroid tissue (0.185-1.11 GBq), shrink an abnormally large thyroid gland otherwise working properly (0.925-2.775 GBq) or destroy thyroid cancer cells (1.11-7.4 GBq)[41]. Cobalt-57 is used in tests for vitamin B-12 absorption; Cr-51 in

the form of sodium chromate is used in determining red blood cell volume or mass, and there are many other radionuclides in general use in nuclear medicine[42]. Approximately one third of all patients admitted to U.S. hospitals are diagnosed or treated using radiopharmaceuticals[43].

Figure 7: NaI I-131 gel capsules for thyroid therapy

Other uses of radionuclides used in medicine are Ir-192 sources used in High Dose Rate Therapy (HDR), sealed Cs-137 sources used in blood irradiators and in radioimmunoassay (RIA) kits[43]. In addition to these primary sources, gloves, needles, gowns, disposables and cleanup supplies become LLW as they become contaminated in these procedures and are often the bulk of the waste that is disposed of.

Universities, government and private labs also use various forms of radionuclides, depending on their mission. For example tritium (H-3) and C-14 are often used as tracers for biological processes and molecular labeling, and O-15 may be used to measure the oxygen carrying capacity of blood substitutes in vivo in a biomedical research

laboratory[44]. Approximately 5% of the total volume of LLW comes from hospitals and universities. This volume composes less than one percent of total radioactivity in all LLW disposed of in commercial facilities[39]. Government agencies contribute 10% of the total volume disposed of in commercial LLW facilities and 5 % of the total radioactivity[39]. This number does not reflect the large amount of LLW disposed of on DOE sites such as Hanford, Idaho National Lab or Savannah River.

Other industries have a long history of using radionuclides. Table 3 on the following page gives an abbreviated list of radionuclides and some of their uses.

Industrial sources account for approximately 50% of the volume of LLW and 10% of the radioactivity[39]

Commercial nuclear power plants produce both LLW and HLW. The LLW waste produced by nuclear plants consists primarily of items such as used hardware and tools, water and air filters, water purification resins, and higher activity wastes such as irradiated components including pipes and valves that have become activated[39]. Commercial nuclear power plants account for 35% of the volume of LLW and 85% of the total radioactivity[39]. Concerning commercial spent nuclear fuel (SNF) the DOE currently has 58,000 metric tons of heavy metal (MTHM) in storage. This waste is from 104 currently operating reactors and 14 shut down reactors and is currently increasing at a rate of 2000 MTHM yearly[45]. Additionally the DOE has 2500 MTHM of spent fuel stored at its facilities [45]. This waste is from experimental reactors and the naval nuclear propulsion program. Currently the only waste increasing from the DOE side of the waste stream is from SNF from nuclear powered naval vessels[45].

Table 3: An abbreviated list of radionuclides used in industry and some of their uses.	
Am-241	Used in smoke detectors, to measure levels of toxic lead in dry paints, thickness gauges such as in rolled steel QA
Cd-109	Used to analyze metal alloys for checking stock and scrap sorting
Ca-47	Aids in the studying of studying cellular function and bone formation in mammals
Cf-252	Used to inspect airline luggage for hidden explosives, and in various moisture gauges
C-14	Many uses, helps to ensure that potential new drugs are metabolized without forming harmful byproducts
Cs-137	Used to measure and control the liquid flow in oil pipelines, to ensure the correct fill level for packages of food or drugs
Co-60	Used in food irradiation, gauges and industrial radiography
Cm-244	Used in mining to analyze material excavated from pits and slurries from drilling operations
Ir-192	Used to test the integrity of pipeline welds, boilers and aircraft parts such as turbine blades
Fe-55	Used to analyze electroplating solutions and to detect the presence of sulfur in the atmosphere
Kr-85	Used in indicator lights in appliances, to gauge the thickness of thin plastics and sheet metal, rubber, textiles and paper
Ni-63	Used in electron capture detectors for gas chromatographs and to detect explosives
Pu-238	Used in radioisotope thermoelectric generators which have powered more than 20 spacecraft since 1972
Po-210	Reduces the static charge in production of some materials
Pm-147	Used in electric blanket thermostats, and as a thickness gauge for thin materials
Ra-226	Makes lighting rods more effective
Na-24	Used to locate leaks in industrial pipelines, and in oil well studies
Tl-204	Measures the dust and pollutant level on filter paper, also used as thickness gauge
Thoriated Tungsten	Used in electric arc welding rods, they produce easier starting, greater arc stability and less metal contamination
Th-229	Helps fluorescent lights last longer
T-230	Provides coloring and fluorescence in colored glazes and glassware
H-3	Used for self-luminous aircraft and commercial exit signs, for watch dials and gun sights, see Figure 8
Ur-234	Used in dental fixtures like crowns and dentures to provide a natural color and brightness

Source 43

.

Figure 8: 20 year tritium exit sign

The remaining waste is legacy waste from the nuclear weapons programs. Legacy waste as used in this text refers to radioactive wastes left to this generation from past generations. For all practical purposes, the vast majority of these wastes came from nuclear weapons production operations, and the legacy left at Hanford is an excellent example of the concept[6]. If all the commercial nuclear plants currently in operation receive extensions and operate for 60 years the total SNF will be 130,000 MTHM[45].

Spent nuclear fuel contains a wide range of fission fragments, which are the main contributor of activity for approximately the first 1000 years. At times much longer than this the long lived actinides dominate the activity. Although fission does produce a wide range of products, it does not produce them with equal probability and the distribution is bimodal with two prominent peaks as shown in Figure 9. Spent fuel from light water reactors (LWR) contains approximately 95.6% uranium with less than 1% being U-235 (the majority is U-238), 2.9% stable fission products, .9 % plutonium with about two thirds being fissile Pu-239 or Pu-241, 0.3 % radiocesium and strontium, 0.1 % radio iodine and technetium, 0.1% other long lived radioactive fission products and 0.1% radioactive actinides such as americium, curium and neptunium[46].

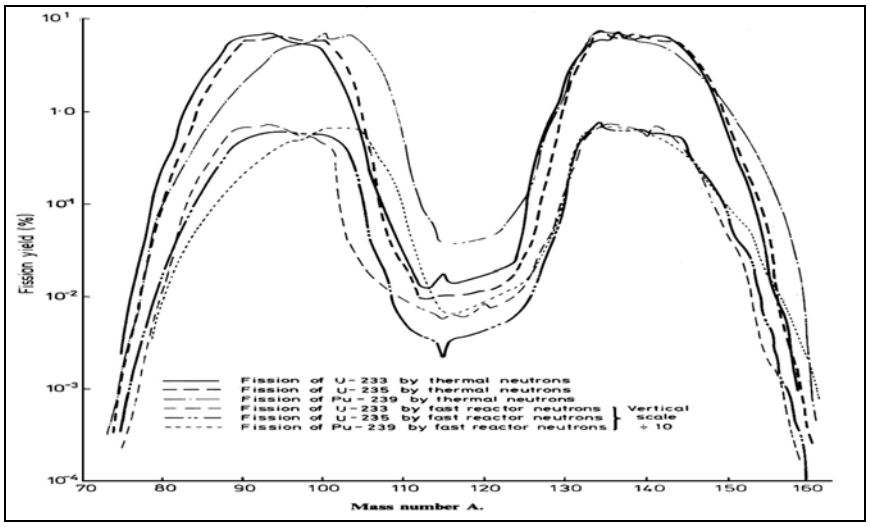

Figure 9: Fission fragment distribution

Currently the U.S. does not reprocess commercial fuel, so this does not currently generate another waste stream, but this may change in the future if reprocessing resumes in this country[47].

Another waste stream comes from the mining, milling and enrichment of uranium ores to produce either nuclear fuel rods or nuclear weapons materials. The steps in the front end of the nuclear fuel cycle are mining, milling, enrichment, and fuel fabrication. Mining in the U.S. is done either physically or chemically. If the actual ore is physically removed by machinery or hand from the earth, it is considered a physical extraction method. Two types of physical uranium extraction that have occurred in the U.S. are open pit mining and underground mining. In open pit mining the uranium ore as well as the overlaying topsoil and rock are stripped away, while in underground mining tunnels are used to extract the uranium ore. Two chemical methods available to extract uranium ore are heap leaching and in situ leaching[48]. In heap leaching a pile of crushed ore bearing rock has extraction chemicals poured over it (often sulfuric acid) and the extracted uranium is reclaimed in drains underneath the heaps[48]. This method is not used

currently in the United States. In situ leaching (see Figure 10) involves treating uranium ore deposits deep underground.

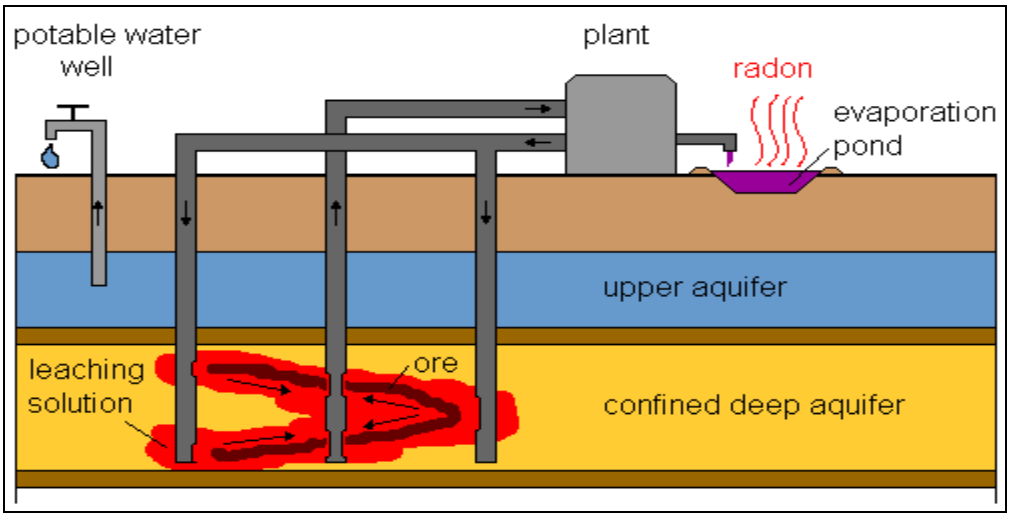

Figure 10: Diagram of in situ leaching for uranium

Water with additional oxygen and sodium bicarbonate (or other leaching agents) are then injected into the uranium ore deposit, which mobilizes the uranium in the rock and dissolves it into the water[49]. The water is then pumped to the surface where the uranium is separated out of the solution[49].

Currently in situ leaching is the extraction method of choice in the U.S., and appears it will remain so in the immediate future. In situ leaching while currently favored in the U.S. can not be used unless uranium deposits are located in an aquifer in permeable rock that is confined by non permeable rock[50]. If the deposits do not meet that condition, traditional mining must be employed, which will generate the larger mill tailings piles instead of the smaller amount of sludge created by in situ leach mining. Although the milling process recovers approximately 95% of the uranium present in ores, the mill tailings will contain several naturally occurring radioactive elements, which include

uranium, thorium, polonium, radium and radon, as well as nonradioactive hazardous elements such as arsenic[48]. This type of radioactive material is called TENORM (Technologically Enhanced Normally Occurring Radioactive Material)[48]. Although this material has less initial radioactivity than its parent ore (approximately 75% of the original ore radioactivity[46]), it has been brought to the surface and is thus more prone to environmental dispersion and contact with humans. At one time these tailings were even used for home site fill before the potential hazards of the practice were fully understood [51]. Much of the mill tailings originating from traditional milling have been remediated under the Uranium Mill Tailings Remedial Action Project (UMTRAP), which was given responsibility to remediate 19 mill tailing disposal sites and thousands of residential properties built on mill tailings[51]. These mill tailing sites are all located in the western U.S., (see Figure 11) except for a lone site in Canonsburg Pennsylvania.

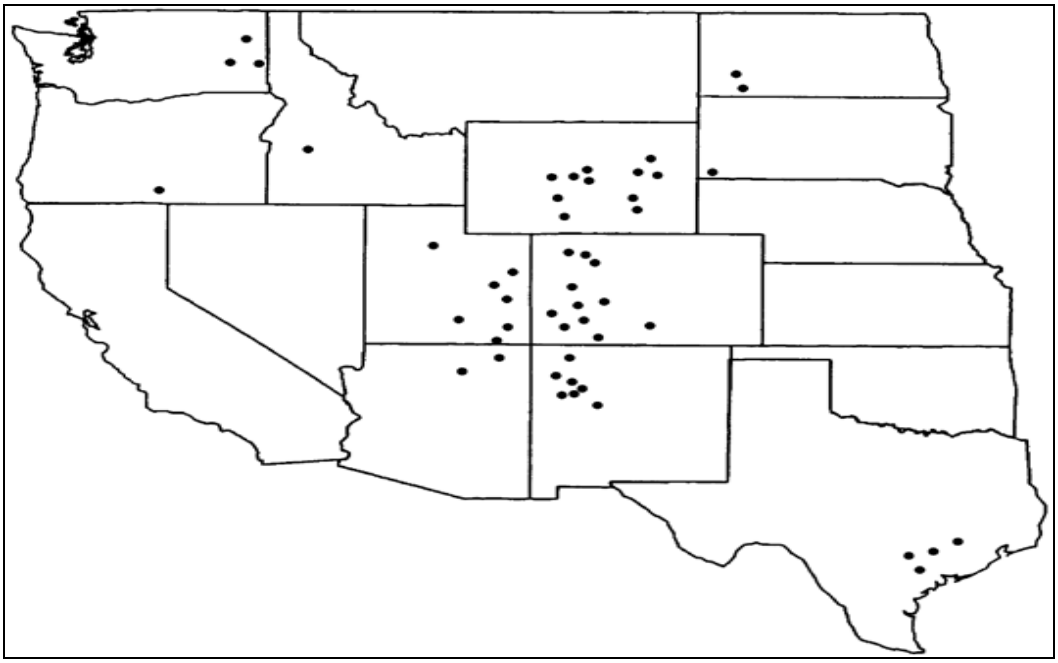

Figure 11: Uranium mill tailings sites

These mill tail pilings ranged from 60,000 to 4.6 million cubic yards of material[49]. Mill tailings have traditionally been capped with an engineered liner of some sort to contain radon gas release and limit intrusion of water, animals and humans.

After milling the natural uranium has been separated from the unwanted excess rock. The natural uranium is composed of 99.2725 % U-238, 0.72% U-235 and 0.0055% U-234[52]. The final product of the milling is a product called yellowcake (see Figure 12) and is primarily composed of U_3O_8 which is packed in casks and shipped to be enriched in U-235.

Figure 12: Cask of yellowcake

The yellowcake is then converted to uranium hexafluoride (UF_6) and is enriched to higher levels of U-235. Previously this was done with diffusion methods but currently the gas centrifuge method is most widely used, however laser separation technologies also exist. The enriched UF_6 is then converted into UO_2 powder containing between 3-5% U-235 the remainder being U-238, pressed into pellets and sintered into a durable ceramic form. This uranium pellet is then loaded into a Zircaloy tube to form a fuel element[53]. The most prominent by-product of enrichment is depleted uranium (DU)[46]. DU has had the majority of its U-235 content removed and thus is considered "depleted"

of fissionable material. DU is often valued due to its high density and is used in ships keels and armor piercing shells [46]. Although DU is slightly radioactive, its primary volume is composed of U-238, which has a half life of 4.47 billion years and is an alpha emitter. Due to this it is not considered particularly hazardous, unless fine dust is inhaled and is treated much like lead due to its chemical toxicity. Depleted uranium is in fact often used as a radiation shield due to its very high density [54].

Other uses of DU include its use in making mixed oxide fuel (MOX) when combined with recycled Pu-239 or for down-blending of highly enriched uranium (HEU)[46]. DU can also be used in breeder reactors to produce Pu-239, but this is not currently being done, as a sufficient weapons stockpile has been achieved.

Legacy weapons production waste and naval propulsion waste comprise a significant volume and activity of waste. Much of the legacy waste was created while making the first nuclear weapons and continued to multiply as the arms race ensued. This entailed waste from mining, milling, enrichment, fuel fabrication, fuel breeding, special nuclear material manufacturing and, most importantly, plutonium extraction from SNF for use in weapons. The scope of the wastes produced at facilities such as Hanford, Oak Ridge, and Savannah River would cover volumes and are outside the depth of this paper. Needless to say the volumes and activities are large. If one just considers LLW from decontamination, decommissioning and remediation of DOE facilities like Hanford, Savannah River, West Valley etc…, the projected needed disposal capacity from 2000-2070 is 9,687,833 cubic meters[55]. In addition to this large volume of LLW, the DOE currently has approximately 2500 MTHM of SNF from naval vessels and 10,300 MTHM of HLW mostly from weapons reprocessing[45]. DOE sites also have large volumes of

buried TRU waste, and interagency agreements have been made to address these wastes. Some of these wastes will be left on site with engineered liners and containment systems while others will be disposed of at the Waste Isolation Pilot Plant (WIPP) in Carlsbad New Mexico[56].

Major Pertinent Legislation

In the early days of plutonium production at Hanford, radioactive cooling water, and waste radioactive materials used in plutonium extraction were often disposed of into the open environment with little restriction on such releases[6]. This lax manner of dealing with radioactive materials no longer exists; the use, possession, transportation and disposal of radionuclides, is now a highly regulated industry. Below are brief summaries of some key pieces of legislation that have determined how radioactive materials are controlled, regulated, stored and disposed of. Due to this increased regulatory framework, materials used in radioactive waste disposal and storage must be carefully characterized so as to ensure their proper performance in the field.

The Atomic Energy act of 1954[20], as amended

This act authorized a program that developed, regulated and oversaw the uses of nuclear materials for military as well as peaceful civilian uses. The original goal of this program was to allow the dissemination of unclassified scientific and technical data while allowing restricted data to be disseminated with certain safeguards in place. This was to be done to encourage scientific and industrial progress on both the civilian and military side. This act allowed licenses to be granted to private industry for such things as

commercial nuclear power generation, medical uses of radioisotopes, and industrial uses, such as industrial radiography. The Atomic Energy act also defined source materials, special nuclear materials and byproduct materials.

The National Environmental Policy Act (NEPA) of 1969, as amended[57,58]

The intention of NEPA was to promote a national environmental policy. Perhaps the most significant aspect of NEPA was that it required the federal government to prepare an Environmental Impact Statement (EIS) for any "major federal actions significantly affecting the quality of the human environment." If this consideration was in doubt then NEPA required an Environmental Assessment (EA) to determine whether a full EIS was needed. In addition so as to not overburden institutions with redundant studies NEPA allowed for "categorical exemptions" for broad categories of activities that it concludes have "no significant impact". NEPA was also significant, as it required any EIS to be filed with the EPA who would then publish them in the Federal Register and seek public input. This allowed for a more transparent process and included stakeholder participation.

President Nixon's Reorganization Plan Number 3[59]

This plan combined "three federal Departments, three Bureaus, three Administrations, two Councils, one Commission, one Service, and many diverse offices" to form the Environmental Protection Agency [60].

Clean Air Act, as amended[61]

Pertaining to the focus of this work, this act authorizes the EPA to establish National Ambient Air Quality Standards (NAAQS) [61]. These standards regulate the emissions of hazardous air pollutants. Under the National Emissions Standards for Hazardous Air Pollutants (NESHAP) the atmospheric release of radioactive materials is regulated. These emission standards are risk based, and attempt to limit the lifetime risk of a fatal cancer to the maximally exposed individual (MEI) to less than a 1 in 10,000[61].

Clean Water Act (CWA) of 1972 as amended[62,63]

This act used a variety of regulatory and non-regulatory tools (such as funding wastewater treatment plants) to reduce point source pollutants. This act made it illegal for anyone to discharge any pollutant from a point source into "navigable water".

"it shall be unlawful to discharge any radiological, chemical, or biological warfare agent, any high-level radioactive waste, or any medical waste into navigable waters" (CWA section 301f)[63]

Safe Drinking Water Act of 1974 as amended[64]

This act authorized the EPA to set "Primary Drinking Water Regulations"[65]. These regulations set mandatory Maximum Contaminant Levels (MCLs) as well as suggested but non-enforceable health goals. These health goals are labeled Maximum Contaminant Level Goals or (MCLGs)[64]. This act limits the dose from drinking water to 4 millirem per year for gamma and beta emitters as well as sets maximum allowable activity for varying alpha emitters in picocuries per liter[60].

Energy Reorganization Act of 1974[23]

This act split the AEC into the Nuclear Regulatory Commission (NRC) and the Energy Research and Development Administration (ERDA). The NRC was now responsible for licensing facilities and provided regulatory structure while the ERDA was tasked with energy research and development. The ERDA would later become the Department of Energy.

Resource Conservation and Recovery Act (RCRA)[25,66,67]

RCRA gave the EPA the authority to implement a "cradle to grave" approach to managing hazardous wastes. This philosophy encompassed tracking wastes from their point of generation through the stages of transportation, treatment, and ultimately to its end disposal. This was the first comprehensive system of waste accounting. While RCRA does not directly regulate radioactive materials as defined in the Atomic Energy Act, it does regulate mixed hazardous waste[60]. "Mixed wastes are wastes that contain both radioactive and chemically hazardous waste[68].

Uranium Mill Tailings Radiation Control Act of 1978 (UMTRCA)[51]

Title I of this act provided for remediation of abandoned mill tailings sites. Title II authorized the NRC to control radiological as well as non-radiological hazards at NRC licensed uranium mill sites. Title II also authorized the EPA to set "generally applicable standards" for both non-radiological and radiological hazards.[49]

Comprehensive Environmental Response, Compensation, and Liability Act (CERCLA) with Superfund Amendments (SARA) of 1986[27,68]

This act deals with uncontrolled or abandoned hazardous waste sites (including those contaminated with radioactive substances) and includes releases due to accidents, spills or other emergency releases[58]. In this act the EPA is authorized to seek out the parties responsible for the pollution, and to ensure they cooperate in the cleanup. The EPA through the Superfund would clean up sites whose responsible parties could not be identified, located, or failed to act. These sites are commonly referred to as "orphan sites". Unlike RCRA which established a "cradle to grave" philosophy for the wastes, CERCLA was legislation concerned with the unattended graveyards of this waste. Of significance in CERCLA are the SARA amendments in which Title III authorized the Emergency Planning and Community Right-to-Know Act (EPCRA)[69]. This act facilitated the development of community emergency response plans and was designed to allow communities to have better access to information concerning hazardous substances. In this amendment facilities are required to report the presence of "extremely hazardous substances" to state or tribal emergency response commissions (SERC/TERC) and Local Emergency Planning Committees (LEPC)[69]. In addition CERCLA allows residents to sue to stop the release of hazardous substances into the environment[58].

Nuclear Waste Policy Act of 1982, as amended[28]

This act provided for the development of repositories for HLW and SNF. It required that locations for these possible disposal sites be identified, studied and the sites characterized. It authorized research into multiple types of disposal media, such as

granitic rock, tuff, salt formations and allowed investigation of deep sea bed disposal of nuclear wastes. This act also authorized the study of Monitored Retrievable Storage (MRS) and Interim Storage (IS) for these nuclear wastes. In the 1987 amendments to the NWPA, study into all the repository sites considered except the Yucca Mountain site in Nevada was halted[70]. Yucca Mountain was limited to 70,000 MTHM until a second repository opened although this limit is not based on any technical data and is arbitrary[45]. In fact independent studies have concluded that Yucca Mountain could easily accommodate 3-4 times the current limit. Some studies have shown it possible to increase up to 9 times the current allowed limit[45]. Needless to say this restriction is a major issue in the disposal of our current and projected inventory of HLW/SNF wastes. Ten percent of this limit was to be allocated to HLW/SNF from defense activities. This left 63,000 MTHM available. Currently Yucca Mountain is at its regulatory limit before it has even opened.

In addition the NWPA created the Nuclear Waste Fund which was to be used to pay for the costs associated with storing commercial SNF in the repository. This fund allocates 0.1 cent per kWh to the fund for electricity produced by the commercial nuclear power industry.

The 1987 amendments also established the Nuclear Waste Technical Review Board. This board was to be composed of 11 members appointed to four year terms by the president from selectees nominated by the National Academy of Sciences. These members would have the responsibility of evaluating the scientific and technical validity of activities relating to site characterization, as well as the activities associated with the packaging and transportation of HLW and SNF.

Low Level Radioactive Waste Policy Act as amended in 1985[29]

This act stated that the states would be responsible for disposing of LLW generated inside the borders of their states. This act also allowed for the formation of interstate compacts (see Figure 13) to ease the burden of disposal.

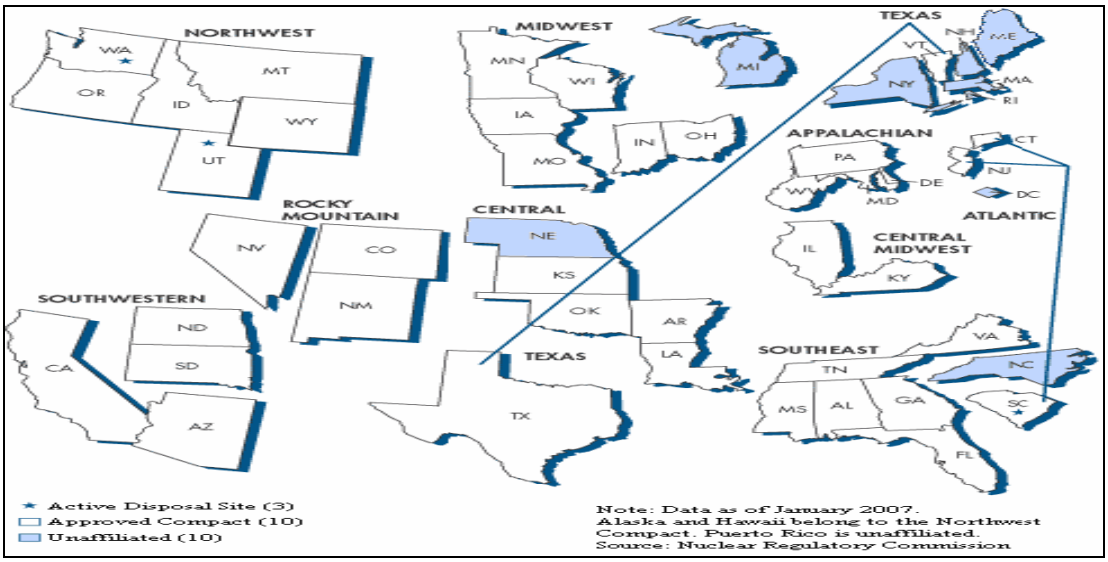

Figure 13: Map of LLW compacts

Federal Facilities Compliance Act of 1992[30]

This act amended RCRA and stated that federal facilities would be subject to the same federal, state and local, laws ,regulations and ordinances, that address solid and hazardous waste[71]. In essence federal facilities would now have to comply with regulations just as a private corporation would. Federal facilities would be required to pay fines and penalties assessed by the states, and must reimburse the EPA for yearly inspections. These stipulations required federal facilities to comply with requirements of such acts as the Clean Air Act and the Atomic Energy Act[58].

Intrusion Rate Measurements in Cementitious Materials

The durability and longevity of cementitious materials used in nuclear waste management is a serious concern, due to long term performance requirements imposed by regulatory agencies such as the EPA and NRC, as well as possible health effects that may result if these requirements are not met. Because of these requirements a series of accelerated testing methodologies such as admixed chlorides and applied anodic current testing have been developed in an attempt to assess future performance; many of these tests are destructive in nature and some critics argue that they are not representative of actual usage or environmental conditions[72, 73].

Common damage mechanisms that may influence cementitious material performance are chloride ingress, sulfate attack, carbonation, decalcification, and cyclic loading combined with freeze-thaw cycles[74,75].

Some key applications of cementitious materials that would benefit from better performance assessment are steel reinforced concretes used in bridges, dams and buildings (including nuclear power plants) as well as cementitious materials used to encapsulate, immobilize, or line nuclear wastes. In all of these applications water and ion intrusion and egress are a key parameter.

Diffusivity is the proportionality constant between a gradient of a substance within a medium and the flux or rate movement in or out of the medium. Hydraulic and ionic diffusivity are often used to characterize water and ionic transport, respectively, in porous materials. A generalized representation water and ion movement can be expressed in terms of a single mathematical form:

$$\frac{\partial X}{\partial t} = \nabla(D_{obs} \nabla X) \qquad \text{Equation 1}$$

where X is the either the water saturation [m^3_{H2O}/m^3] or ionic concentration [mg/m^3], t t is time [s], ∇ represents the differential operator with respect to space, and D_{obs} is the either observed hydraulic or ionic diffusivity [m^2/s]. However, while a single equation form may represent the movement of water and ions mathematically, ionic diffusion is often associated with a gradient in concentration whereas the movement of water within a porous matrix is largely due to bulk transport of liquid water under saturation or capillary pressure gradients[76]. Thus, the term "hydraulic diffusivity" is not truly diffusion in the classic sense.

To better understand why techniques are needed to quantify ingress and egress rates, several material degrading factors are summarized below. Ingress rate is a key factor in determining when a damaging event begins, and ingress and egress rates may be significantly altered after damage occurs, due to one or more of these mechanisms. For example chloride ion transport may occur by advection, ionic diffusion, or some combination of both. Thus a determination of the depth of water ingress or depth of ion penetration into steel reinforced concrete would be beneficial for corrosion modeling. Sulfate ions may also be carried in the same two manners and may cause concrete degradation. Carbonation of a material can change the microstructure by converting an amorphous phase to a crystalline phase, which will change the capillary potential of the material, and in so doing change the ingress and egress rates. Decalcification may also lead to microstructural changes which will affect ingress and egress rates. Lastly ingress of water coupled with freeze-thaw cycles may lead to fracture and microfracture flow which can degrade the material structurally and further change ingress and egress rates.

Regardless of the application, whether it involves nuclear waste encasement, or bridge supports, the measurement of rates of water migration and ionic diffusion are key parameters in predicting material performance before and after a damaging event.

Chloride Ion Ingress

The ingress of chloride ions is of concern in steel reinforced concrete structures, as this is widely considered one of the main causes of deterioration in reinforced concrete structures. Chloride ions penetrate the porous structure of the cementitious material, corroding reinforcing bars and degrading the structural integrity of the surrounding concrete[77]. Damage from chloride ion ingress is characterized by a time of initiation and time to failure. The time of initiation is the time it takes chloride ions to reach the rebar and to achieve a critical threshold[74]. While the time of failure is the time in which the rebar or the structure has deteriorated to an "unacceptable level".

This critical chloride threshold varies depending on the type of rebar used, whether an uninterrupted mill scale exists, and whether the steel has been passivated and contains a protective film around it[72,78,79].

Sulfate Attack

The key to sulfate ions destructive nature in cementitious materials is that their reaction with cementitious minerals tends to produce products that are of greater molar volume than their reactants, resulting in expansion which can cause spalling (see Figure 14), strength loss and severe degradation[74].

Figure 14: Expansion due to sulfate attack

Sulfate ions may interact with dissolved ions in the pore solution and form ettringite, thaumasite and gypsum[74] with ettringite often viewed as the primary expansive phase[80]. These phases precipitate within the confined pore structure resulting in mechanical stress. When the stress exceeds the Young's modulus of the cementitious material, an irreversible strain is experienced that may damage the material through formation of cracks. In general the sulfate attack via ettringite formation in concrete is based on two primary reactions: the reaction of SO_4^{2-} and $Ca(OH)^{+}$ which forms gypsum and the subsequent reaction of gypsum with calcium aluminum hydrates which yields ettringite[80-83].

The resistance to sulfate attack varies in cementitious materials depending upon cement composition and fineness, water to cement ratio, and permeability. The amount of tricalcium aluminate is known to affect the resistance of a cement to sulfate attack such that the amount of tricalcium aluminate is limited in Type II cement under ASTM C150 and AASHTO M85 specifications to less than 8%[80].

Carbonation

The reaction of alkaline pore solution with dissolved carbon dioxide, known as carbonation, has two main effects on concrete: (1) a porosity decrease due to precipitation of carbonate minerals in the pore space and (2) neutralization of the pore solution. Carbonate precipitation is considered to be beneficial to the compressive strength of the material and may possibly even favor the formation of a protective layer at the surface of the concrete[74]. Due to alteration of the pore structure, the rates of ingress and egress for both water and ions will decrease, affecting predictions of durability. The carbonation reaction consumes hydroxides and will neutralize the pH of the pore solution. In reinforced concretes, lowering the pore solution pH may lead to destruction of the passive layer surrounding steel reinforcement allowing for corrosion[74]. In cement-based materials used to immobilize wastes, contaminant solubility may increase or decrease with pH due to carbonation[84]. Thus the rate and depth of carbonation may affect contaminant release rates, the microstructure, durability, and future ingress and egress rates.

Decalcification

Decalcification of cement typically occurs in structures exposed to acidic or pure waters for extended time periods, such as water pipes, dams, and radioactive waste disposal facilities[74]. Decalcification primarily occurs when calcium leaches from a cement material and portlandite mineral, $Ca(OH)_2$, as well as calcium silica hydrates (C-S-H) gels dissolve to replace calcium[74]. Portandite and C-S-H gel make up the majority of cement solid phases and the loss of these common mineral phases leads to an increase in porosity and permeability which can decrease mechanical strength[74,83]. In turn, the

increase in permeability will affect transport rates and may enhance the loss of soluble waste products out of an immobilizing matrix for example.

Freeze-thaw damage

Freeze-thaw damage in concretes occurs when infiltrating water expands during rapid freezing. In a similar manner as sulfate attack, the expansion during freezing creates strain and the material may crack. Repeated cycles of freezing and thaw yields a damaged material and in some cases may lead to spalling (see Figure 15). This damaged material may then be more susceptible to additional kinds of attacks as well as loss of mechanical strength[75]. The ingress of water into the material as well as pore size and ingress of aggressive salts into the pores, can be used to predict damage from freeze-thaw cycles.

Figure 15: Damage from freeze-thaw cycle

Prior Non-Destructive Measurement Techniques Used to Measure Intrusion

Information gathered by non-destructive means is typically preferable to the same data obtained by destructive means. Nondestructive methods have several advantages:

- the sample remains intact and available for subsequent or complimentary analyses;
- the sample may need to be archived and retested after an extended length of time to allow weathering or controlled physical or chemical exposure to occur;
- non-destructive techniques allow a permanent record if a challenge to the test occurs.

While a perfect non-destructive technique would not alter the sample or structure at all, many of these techniques are in actuality minimally intrusive or minimally altering techniques.

In previous studies, imaging modalities using multiple types of radiations as information carriers have been used to locate solution or ionic fronts in cementitious materials. These techniques include radio frequency waves used in nuclear magnetic resonance (NMR) methods, use of x-rays and gamma rays in standard 2D radiography, 3D computed tomography with standard x-ray tube sources and synchrotron sources, radiotracer methods including positron emission tomography (PET), and neutron radiography[85-95].

Standard 2D Radiography

In standard 2D radiography, an x-ray source projects a beam onto an object, most often accomplished with an x-ray tube head assembly (Figure 16).

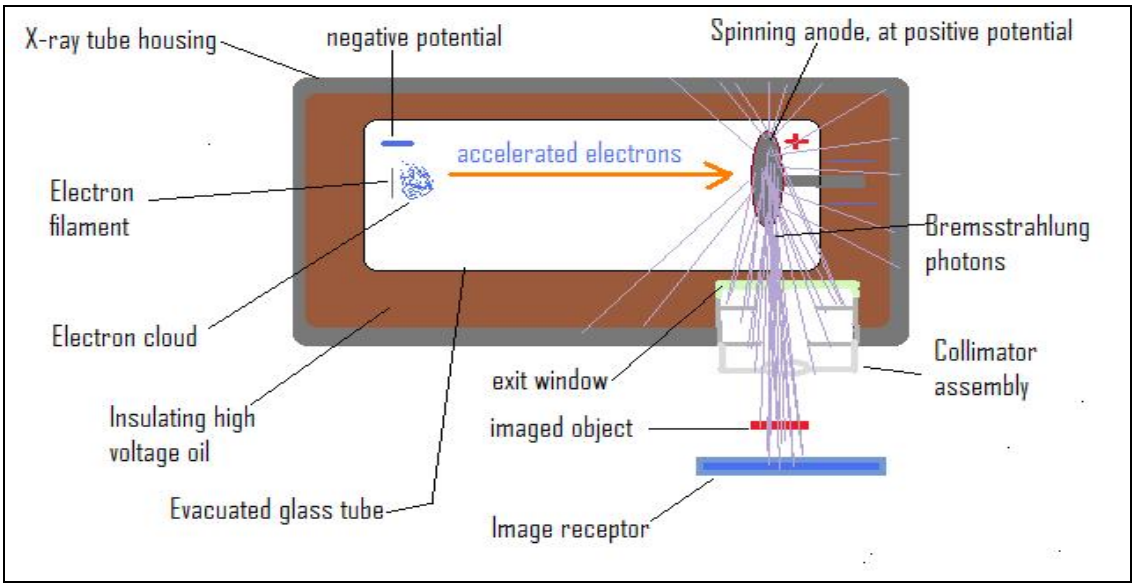

Figure 16: Simplified drawing of x-ray production with a tube

The x-rays then interact with the object through photoelectric absorption and Compton scatter. At this point, some of the x-rays have been absorbed completely, or scattered away from the useable beam, while others have been re-emitted at lower energies after Compton events. The remaining photons exit the object and continue on until they interact with the image recorder.

The image is often described as a shadow of the object because the areas that attenuate to the highest degree, such as bone in medical imaging or metal granules in cement, will absorb most of the photons and will appear on film as bright areas due to the developing process. In contrast, x-rays traveling through less dense media like soft tissue or silicates will preferentially penetrate the less dense media and be displayed as darker areas on film. Thus, in traditional radiography, brighter whites are associated with higher

density materials, while darker grays are correlated to low density materials. With modern digital techniques, this is arbitrary and the contrasts can be reversed. The image of the object is a map of linear attenuation coefficients, which are strongly correlated to the density of the materials. This map of linear attenuation coefficients is transferred onto a film, a digital imaging plate, or an image intensifier with camera system and monitor if dynamic viewing is needed.

This method measures the total attenuation along a path and cannot determine whether less dense, or more dense objects, are in front of each other from a single projection. Thus all information in one axis is summed into a single attenuation coefficient. This lack of a third dimension in which objects in front and behind each other can not be separately resolved is a serious limitation of 2D radiography. Figure 17 illustrates this limitation, which will be referred to as information compression. If an x-ray photon passes through the cementitious sample on its way to detector segment x, it may first pass through a series of material sections (e.g., a thickness of matrix, an air void, an iron sliver, etc). The information from all these objects are projected onto one pixel, since all these objects are in a row, the information about the individual elements cannot be discerned. There is no way of knowing the photon's specific interaction path from this one projection and point x in the diagram will record a linear attenuation coefficient that is the sum of the linear attenuation coefficients for all the different media traversed by the photon. With respect to cement materials, water in a large pore (less dense area) behind a vein of high density material would not be seen in a single projection. Because of this, cement samples used in 2D radiography are often made into thin rectangular slabs, to minimize the loss of such information.

Standard 2D radiography has been used to detect the presence of a migrating fluid that is displacing a volume of air in pores[88,89]. This is possible since the linear attenuation coefficient for the fluid is higher than that of the air it is displacing. Thus the linear attenuation of the representative pixel will increase when the fluid intrudes and displaces the lower density air. Whether this can be detected in actuality depends on the relative volume of the fluid intruding compared to the pixel size. If the medium has a large porous structure and the detection medium has a smaller detection area, then the change in the linear attenuation coefficient per pixel may detectable.

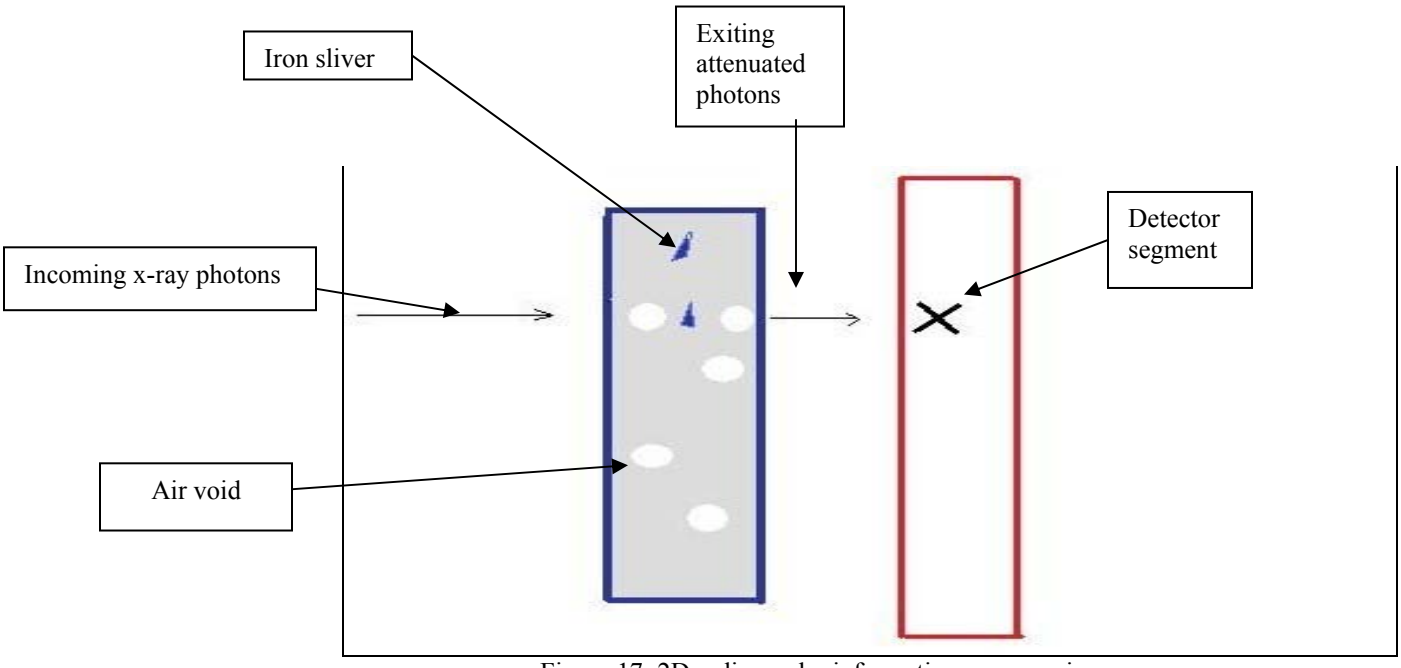

Figure 17: 2D radiography information compression

Another issue with x-rays produced from a tube is that the bremsstrahlung radiation is produced over a large range of energies (see Figure 18). For example if the

maximum accelerating voltage was 70 kVp the highest energy x-ray photon able to be produced would be 70 keV, while the mean energy of the beam will be much lower (see Figure 18).

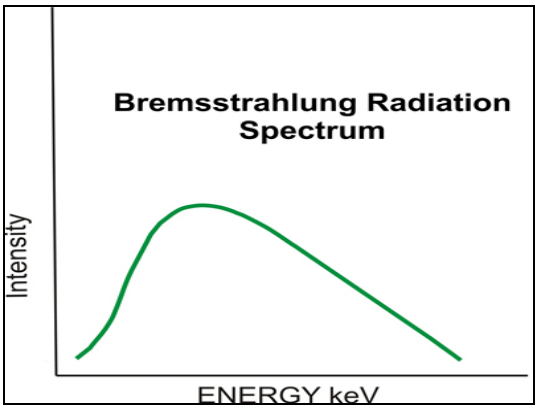

Figure 18: Bremsstrahlung production from x-ray tube

Since the energy spectrum is so broad, and since linear attenuation is strongly correlated to photon energy, a wider than desired absorption band occurs that can degrade resolution. In order to compensate for this, filters designed to narrow the beam energy width by preferentially removing the "softer" (i.e., lower energy) photons are often used. Filters of aluminum and copper are frequently used, this results in what is commonly called "beam hardening" as the remaining beam energies are shifted to the more energetic or "harder" x-ray energy range. Although beam hardening improves resolution, it comes at the cost of reducing photon flux, and more tube output is needed to achieve a given flux. If severe filtering is used, the x-ray tube's life may be shortened significantly due to electron filament burnout and other heat related issues.

Another type of photon produced in an x-ray tube is characteristic x-rays. These x-rays occur when electrons are knocked out of their shells, causing a higher level electron to drop into the shell vacancy. When an electron drops into the vacancy, energy is released in the form of a photon whose energy is the difference between the two shells

energies. This photon energy is thus "characteristic" of the material's energy levels (see Figures 19 and 20). For instance, the photon emitted when an electron drops from the L to the M shell in lead is of different energy than the photon emitted when an electron from the L shell fills a vacant K orbital in copper. Also, since higher level shells often donate an electron to fill a lower shell vacancy, that higher shell vacancy will now need filled, thus a cascade of characteristic x-rays may occur. These characteristic x-rays will be superimposed on the bremsstrahlung spectrum and can be quite prominent (see Figure 21).

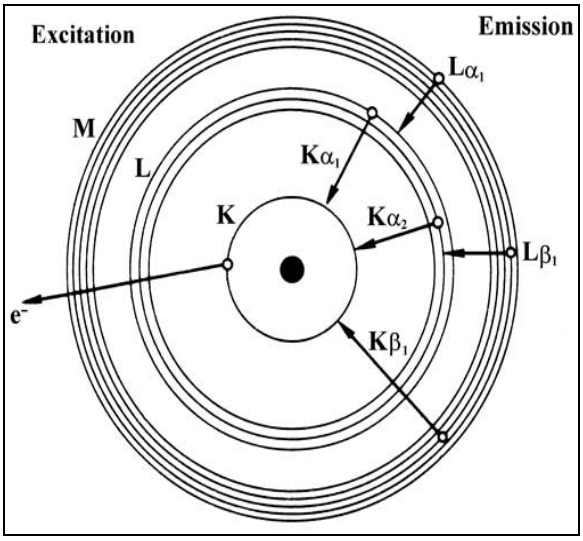

Figure 19: Electron shells

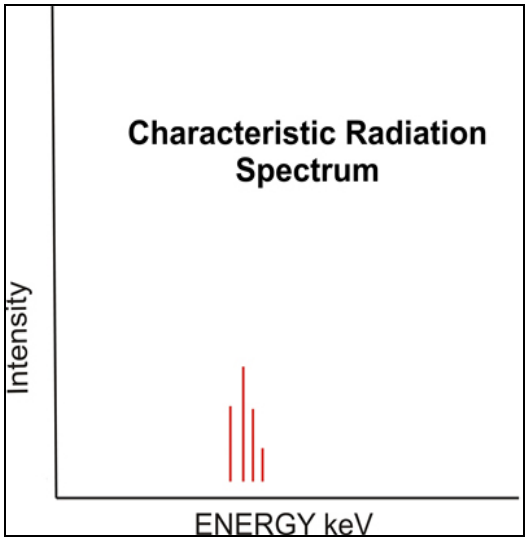

Figure 20: Characteristic spectrum

Additionally, multiple transitions may occur that are from greater than one shell away. For example, a K shell electron vacancy may be filled by an electron in the M shell. This involves a transition of the electron through two energy states. In order to accurately describe the transition taking place, a characteristic x-ray naming system was developed. In this system the shell that has the vacancy to be filled is first named. Next the shell location of where the filling electron came from is named. For example, if we

have a K shell vacancy filled by an L shell electron it is denoted as a Kα x-ray. If a K shell orbital is filled by an M shell electron it is denoted as a Kβ x-ray. Thus if the vacancy is filled from the next shell up it is a alpha, if from two shells up a beta, and so on. Furthermore since different sub-shells exist in which transitions can exist the alpha and beta is described by a numeral such as 1, 2 or 3. Full spectroscopic notation can be complex, and will not be discussed here.

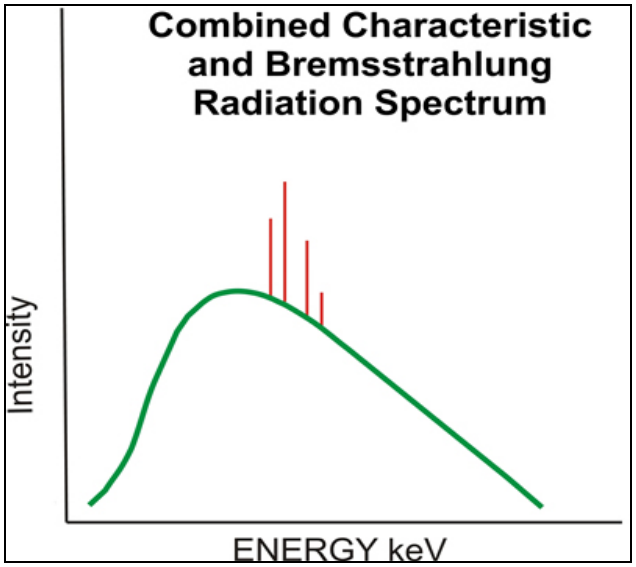

Figure 21: Generic observed x-ray tube spectrum

Due to the issues of wide energy spectra and filtering issues, if higher resolution is needed, an x-ray source with a narrow distribution may be used. This can be achieved by using synchrotron radiation as the source, instead of bremsstrahlung radiation from an x-ray tube.

Synchrotron Radiation Used in 2D Radiography

Synchrotron radiation is given off when charged particles such as electrons and protons are accelerated to high energies and steered by magnetic fields into a curved

path[96,97]. The wavelengths of the photons emitted in high energy electron or positron storage rings range from infra-red to x-rays and if the charged particles are at relativistic speeds the photons are emitted in a narrow cone beam that can be "tapped" and collimated (see Figure 22).

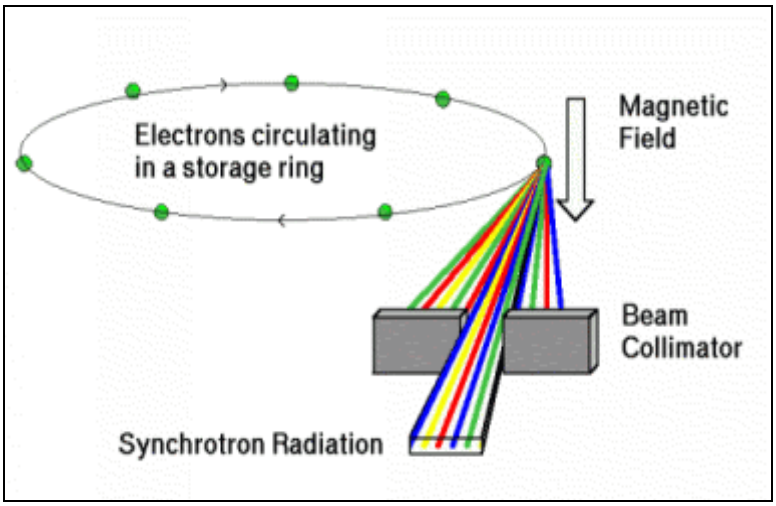

Figure 22: Basic diagram of synchrotron radiation tap

Although the spectrum given off by synchrotron radiation is not narrow initially, its flux is extremely intense and can be hundreds or thousands of times that of a conventional x-ray tube [96]. Because of this high intensity, the beam can be intensively filtered to provide a narrow almost monoenergetic energy width, while still providing adequate x-ray flux. This intense nearly monoenergetic beam provides better imaging resolution. Additionally, if another energy level is desired, the filtering can be changed to produce another near monoenergetic beam of a different energy. Because of the wide range of constituents in cementitious materials with different linear attenuation coefficients this intense monoenergetic beam is preferable to the weaker (lower flux) wider energy beam produced by an x-ray tube. The main disadvantages are that

synchrotron sources are not easily accessible, and are expensive to build and operate. Although the contrast and resolution can be better with a synchrotron x-ray source, allowing for fluids to more easily be seen intruding; if this beam is used in a 2D setup the spatial limitations are the same as with a tube. The third dimension can not be resolved spatially and is flattened out and summed. 3D synchrotron tomography eliminates this problem but is not in widespread use.

2D Radiotracer Techniques

Radiotracer techniques are different than techniques using external x-ray generation sources as the source of the radiation is internal to the sample. This internal source is achieved by allowing a radioactive gas or liquid to intrude into the sample to be imaged. The radionuclide undergoes radioactive decay and emits radiation that penetrates the sample to varying degrees and is recorded by detectors surrounding the sample. In its simplest form, a sheet of film can be wrapped around or placed under the sample to act as a radiation detector. In more complicated setups an array of detectors (such as sodium iodide (NaI)) often surrounds the sample.

The type of radionuclide used as a tracer is important, since different molecules or atoms may be retarded or bound more strongly than others, and some may chemically react with the sample causing unwanted products or structural changes. Additionally different radionuclides emit different types of radiation, which have varying penetrating abilities, even if the radiation energy is constant. For instance, some radionuclides are pure beta emitters while others are beta/gamma emitters, and still others are alpha emitters. Gamma emitters or those that are positron emitters which will eventually release annihilation radiation, are the most commonly used tracers in dense or thick materials

such as cements due to their ability to penetrate deeply into solid materials. In contrast pure beta emitters such as P-32 are often used as tracers in research when the limited range of the beta is not a significant detriment.

As stated previously, degradation due to chloride ions is a significant concern in rebar containing cementitious materials, and thus the location of a chloride front in a cementitious sample is desirable to know. This has been done in the past by using the radionuclide Br-72 as a surrogate for chlorine[91]. Radioisotopes of chlorine could not be used, since no suitable gamma emitting radioisotope of chlorine is present[91]. Bromine was often chosen, since it behaves chemically similarly to chlorine. Gamma emitting radioisotopes of iodine could be used under the same line of reasoning.

In addition to chloride ion ingress, water migration and NaCl solution studies have been performed. Water migration studies have used Tc-99m in the form of the pertechnetate anion in aqueous solution while NaCl solution studies have used Na-22 as the radiotracer[91]. Solutions of NaCl are often used to seal waste placed in underground tunnels by pouring the solution of NaCl over bentonite which has the capacity to swell considerably creating a tight seal[91]. If Na-22 is used as a radiotracer, the depth of the solution's penetration can be approximated and conclusions concerning the quality of the seal can be made. These types of studies can provide good dynamic front information and general diffusivity information, but they provide poor structural information, as the exact location of the radionuclide in 3 dimensions is not known. Improved location of the tracer in 3D can be achieved by using Positron Emission Tomography or PET techniques. These techniques can yield a spatial resolution of around 5 mm in 3D and will be discussed later[98].

2D Neutron Radiography

Neutron radiography has many similarities to x-ray radiography, but has some key differences as well. Both techniques use radiation to probe the target, but x-rays interact with the electrons of an atom while neutrons interact with the nucleus. Photoelectric absorption increases predictably with atomic number for x-rays, while the neutron cross-sections do not depend on atomic number in any monotonic manner and in fact many higher Z metals are effectively transparent to neutrons while low Z materials such as hydrogen and carbon have high scattering cross-sections [94]. Furthermore, desired neutron interactions have the complication of competing with additional absorption, capture, fission and scattering reactions. Although fission is not a concern in cementitious materials, the neutron capture reaction can be especially troublesome as it can produce high energy gamma rays. These neutron capture gamma rays then become unwanted background in the detection system designed to detect charged particles.

$$N + {}^{1}H \rightarrow {}^{2}H + \text{gamma} \qquad \text{(example of neutron capture reaction)}$$

Another difference is that most neutron detectors respond to low energy neutrons and need moderators to reduce the neutrons to energies in which significant detection can occur through charged particle creation. Conveniently hydrogen, water, and carbon are excellent moderators while deuterated water moderates even more effectively than regular water[99]. This is due to regular hydrogen having a high cross section for the neutron capture, while deuterium's cross section for capture is much lower. Detection

after moderation, has been done with helium-3 detectors in which a neutron interacts with the He-3 atom and produces a triton and a proton[95,99]. The charged proton or triton is then detected.

$$n + {}^{3}He \rightarrow {}^{3}H + \text{proton} + 0.764\ \text{MeV}$$

Another common detection reaction for neutrons utilizes B-10 which produces an alpha particle which can be easily detected[100].

$$n + {}^{10}_{5}B \rightarrow \begin{cases} \alpha + {}^{7}_{3}Li + 2.310\ \text{MeV}\ (94\%) \\ \alpha + {}^{7}_{3}Li + 2.792\ \text{MeV}\ (6\%) \end{cases}$$

Others have chosen to detect neutrons with detection setups consisting of neutron scintillators, multichannel plates and a CCD camera[94].

The advantage of using neutron radiography for, aqueous flow or moisture content determination in cementitious materials is that neutron radiography is extremely sensitive to water and hydrogen content while being basically transparent to many metals. This sensitivity is due to the high scattering cross sections of hydrogen and water for thermal neutrons[94]. Because of this high scattering cross section, water can be easily tracked through porous materials (see Figure 23).

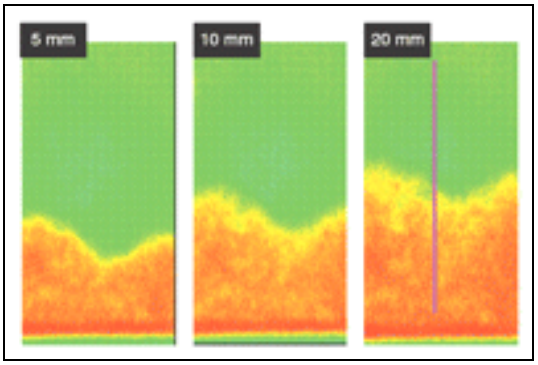

Figure 23: Color enhanced NRAD image of water fronts in a cement sample at varying times

One significant disadvantage of neutron radiography is that it can not distinguish chemically bound water from free water, as NMR systems can, due to the distinction of different relaxation times[95]. To determine moisture content with neutron radiography the macroscopic neutron attenuation coefficient of the material is determined when it is completely dry and when it is completely wet. If the thickness of the sample is known, the moisture content can be determined by measuring the transmission through the sample and solving the equation below for θ[95].

$$I = I_0 \exp[d(\mu_{mat} + \theta\mu_w)] \qquad \text{Equation 2}$$

where I is the transmitted neutron flux, I_0 is the initial neutron flux, d is the sample thickness, μ_{mat} is the dry macroscopic neutron attenuation coefficient, μ_w is the wet macroscopic neutron attenuation coefficient, and θ is the volumetric moisture content.

Positron Emission Tomography (PET)

In PET studies used in medicine, a radiotracer is introduced into the subject and is allowed to concentrate into the organs or mass of interest. The subject is then scanned and the radiations from the subject are detected by a ring or rings of detectors surrounding the patient[101]. PET is unique since the radiotracers it uses are positron emitters. After positron emission, two 511 keV photons are emitted when an electron and the positron annihilate (see Figure 24). The annihilation photons are formed at almost exactly 180 degrees apart, conserving momentum. This 180 degree behavior of the annihilation photons allows for the Line of Response (LOR) to be determined, if both photons reach the detectors unattenuated and undeflected.

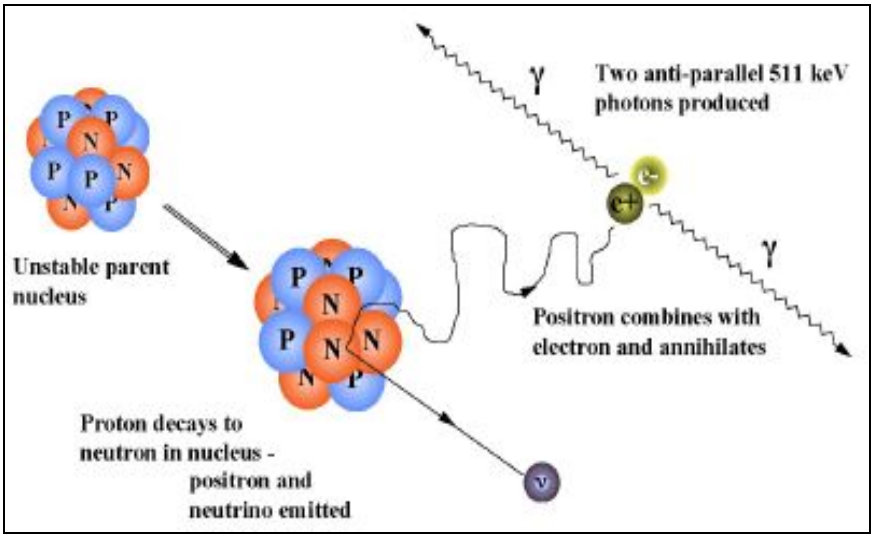

Figure 24: Positron decay and annihilation radiation creation

A count in each detector is only accepted by the circuitry if detection occurs simultaneously in two opposing detectors (see Figure 25) within a time frame of approximately one nanosecond[102]. While clinical studies in humans are currently dominated by the use of F-18 in the form of fluorodeoxyglucose, other positron emitters such as C-11, N-13, O-15 are of great interest in metabolic research[102].

PET's use in cementitious studies is not limited to the short lived positron emitters mentioned above, and since radiation dose is not a primary concern in imaging inanimate objects, more latitude is available in choosing a positron emitter. However, an important issue is that many positron emitters have very short half lives which are not suitable for the time frame of an intrusion study; this significantly limits positron emitter choices if longer term studies are to be done. If long term studies are done with short half life positron emitters, very high starting activities may be required. Cu-64 a positron emitter with a 12.7 hour half life, complexed with EDTA to create a soluble inert form, has successfully been used by UK researchers to monitor water flow in building materials

as well as to measure hydraulic diffusivity in the material[93]. Hydraulic diffusivity was calculated in this experiment by using the one-dimensional solution to the extended Darcy equation and plotting the reduced water content versus $xt^{1/2}$ and then using the method of Bruce and Klute to calculate the unsaturated hydraulic diffusivity[93,103].

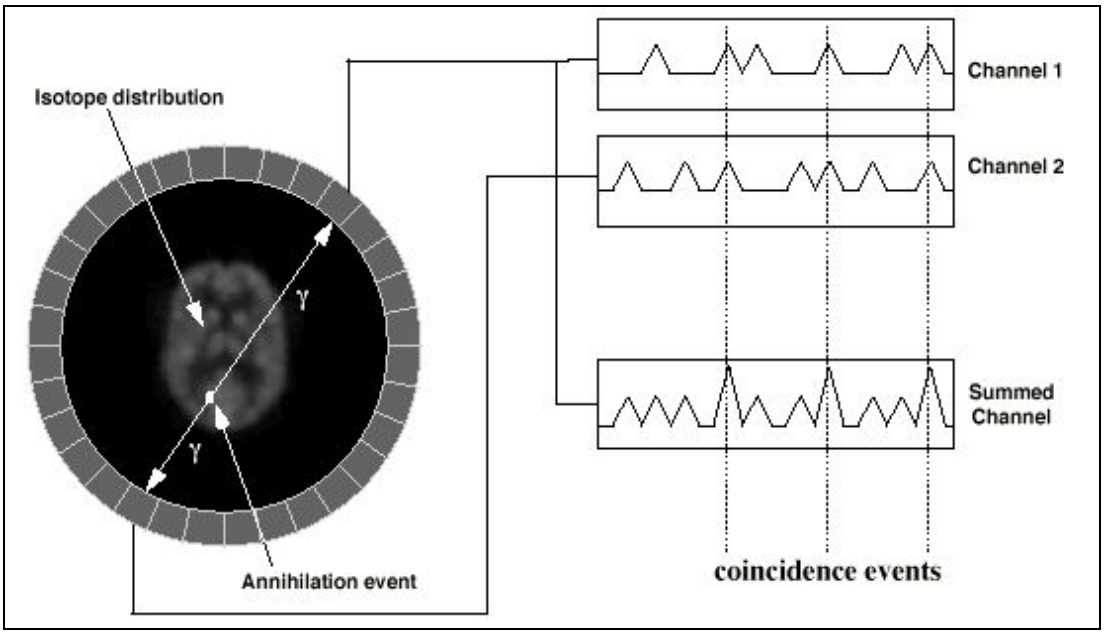

Figure 25: Coincidence event acceptance

Regardless of whether PET is used clinically or for material research, several factors can affect the accuracy of PET reconstructed images. These reconstructed images are achieved through advanced backprojection techniques similar to CT image reconstruction[102]. Of note, is that not all simultaneous detections are from true coincidence events. Because of this false LORs can be recorded which will influence the reconstructed location of the source (see Figure 26). Additionally the positron will move a finite distance in the medium before it annihilates, thus affecting the recorded location of the activity. This distance to annihilation is approximately 1 mm is tissue and will be

less in cementitious materials depending on the density of the material[104]. The size of the detectors and their depth (see Figure 27) will also factor into the precision of the source location as will the non-colinearity of the annihilation radiation emission, as it is not always exactly 180 degrees [104]. Due to these factors, PET is currently limited to a resolution of approximately 5-6 mm in clinical applications[98].

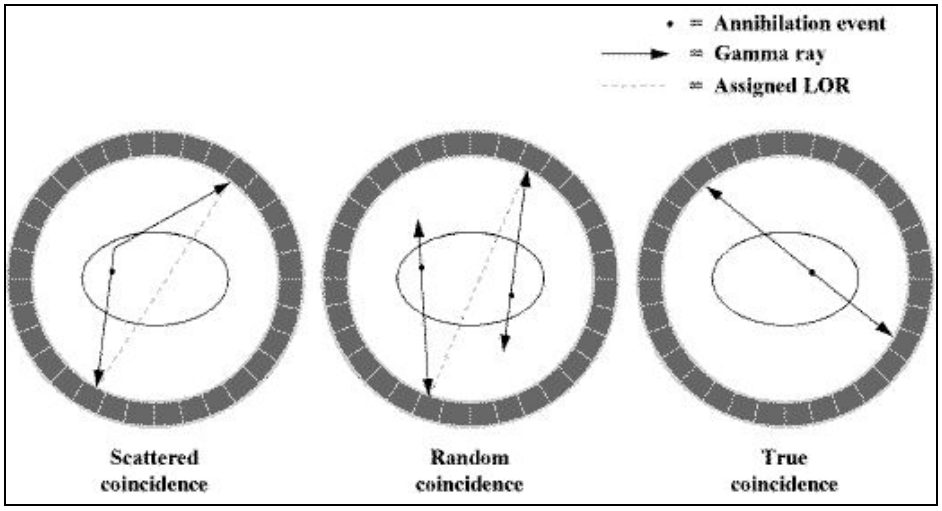

Figure 26: Types of coincidence

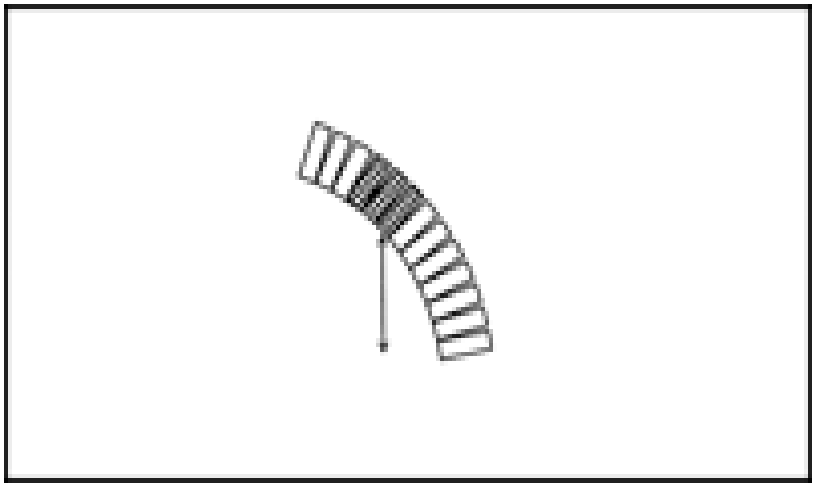
Figure 27: One photon being detected in 3 detectors

Nuclear Magnetic Resonance Techniques (NMR)

NMR has a relatively long history of being used for imaging water flow within porous materials. In 1979 Gummerson et al. first used proton NMR to examine water flow in clay loam and sand samples with good results[85]. This group also examined fired-clay building bricks and concretes but extremely weak signals were generated from these samples. New pulse sequences and reconstruction techniques have alleviated some issues with scanning porous materials but paramagnetic and ferromagnetic materials contained within these materials as well as very short relaxation times still restrict the widespread use of the technique. The paramagnetic and ferromagnetic issues are especially significant as there is a desire to utilize waste blast furnace slag and fly ash in many of these cementitious products. These waste additives are high in iron oxides containing significant amounts of hematite and magnetite. The effect of these components is to shorten the effective T2 time to very short times, making scanning of such materials problematic[102]. Although a significant amount of research has been done using proton NMR to scan cementitious materials many researchers have avoided this problem by using white cement blends or blends that contain low concentrations of paramagnetic and ferromagnetic substances[73,86,87]. Although interesting, these studies do not necessarily represent how cementitious materials with fly ash and blast furnace slag will react to water or ion intrusion. More situation-specific knowledge of water movement and ion ingress into cementitious materials, when used in critical applications such radioactive waste disposal or nuclear power plants, is highly desirable. A basic explanation of how proton NMR works is in order to better understand its uses and its limitations.

In NMR, processes on the quantum and macroscopic level are used to produce an NMR signal. In order to understand the phenomenon, both views are often used. Several types of motion are believed to occur with protons just like macroscopic items such as tops. For example a top rotates around an axis, this is considered a first order motion. Additionally the top may precess; precession is the rotation of the top around an axis other than its axis of rotation and is a second order motion. This precession is evident in the wobble of a rotating top around an axis defined by the earth's gravitational field (see Figure 28). Lastly a top may precess at different angles in reference to this other axis. The changing of this angle of precession is called nutation, and is a third order motion. A proton is believed to exhibit these same motions.

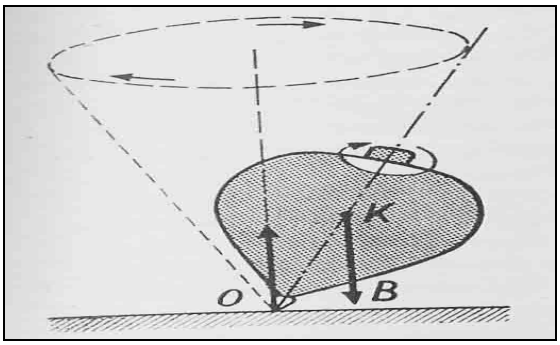

Figure 28: Top exhibiting rotation, precession, and the angle of precession

If viewed in the classical sense, protons behave as small magnets which have magnetic moments with both magnitude and direction. In the absence of a strong magnetic field these proton magnetic moments will be randomly oriented. If a strong magnetic field is then applied, in the Tesla range, the magnetic moments will align with the magnetic field (see Figure 29).

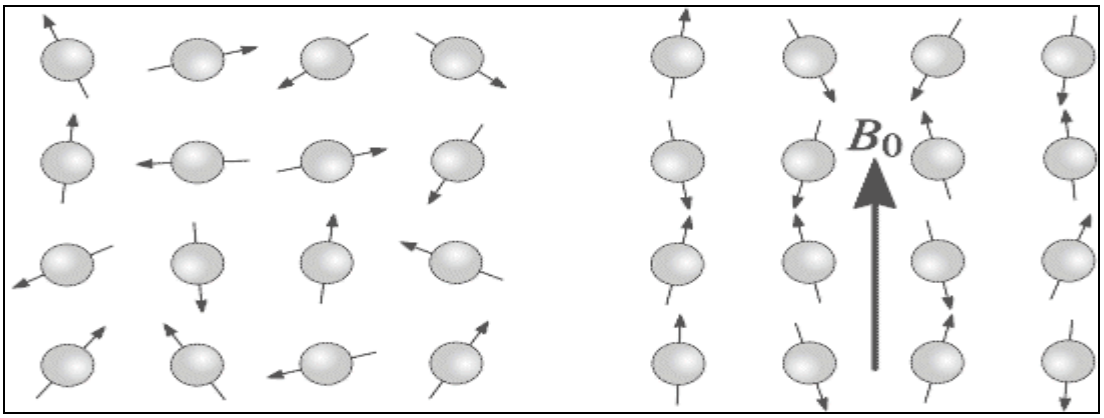

Figure 29: Magnetic moments before and after a strong magnetic field is applied.

Some of the proton magnetic moments will align parallel to the magnetic field while others will align antiparallel to it. These energy states are not the same, however, and the parallel orientation is at a slightly lower energy level than the antiparallel orientation. There will be a very slight excess of protons aligned parallel to the field. These excess magnetic moments are aligned with the field but are not currently in phase. At this point the protons are rotating around an axis as well as precessing around another axis at a frequency determined by the gyromagnetic ratio and the magnetic field strength (see Figure 30).

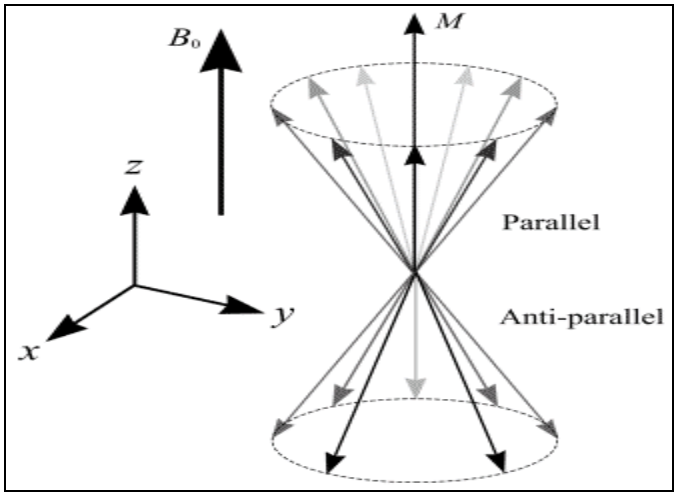

Figure 30: Precession in parallel and antiparallel states

This precesion frequency is determined by the Larmor equation.

$$F=\gamma B \qquad \text{Equation 3}$$

where F is the precessional frequency in MHz, γ is the gyromatic ratio in MHz/Tesla and B is the magnetic field strength in Tesla[102]. For magnetic field strengths used in standard proton NMR this frequency is in the radio wave range of the electromagnetic spectrum, which is why the terminology of Radio Frequency (RF) pulses in used when discussing NMR.

If a radio wave of the resonance frequency, i.e. one that matches the Larmor frequency, is applied to the protons, the protons will absorb energy and be promoted to the higher energy antiparallel state; as well as have their precessing magnetic moments synchronize in phase and thus reinforce each other[105]. Classically the "cone of precession" is said to flip from the parallel to the antiparallel orientation. At this point the affected protons are said to be in resonance. This is where the term resonance comes from in MRI. In the quantum interpretation this radio wave provides photons of just the right energy to promote protons from the lower energy parallel alignment state to the higher energy antiparallel alignment state. In the macroscopic world this absorption of energy by a large number of individual protons (as viewed from a rotating reference frame) appears to tip or nutate the bulk magnetization vector down into the xy plane (see Figure 31).

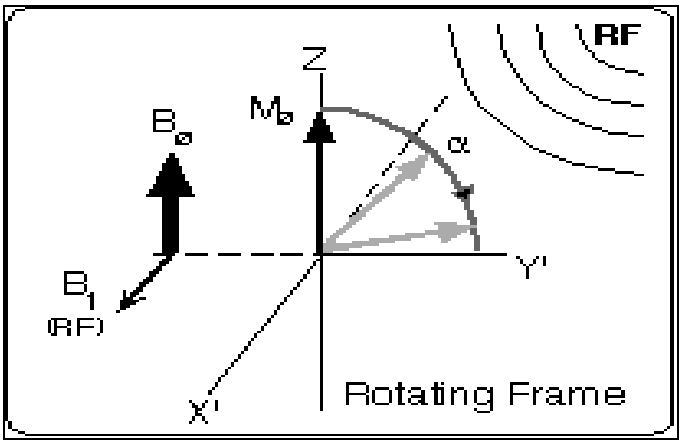

Figure 31: Tipping of bulk magnetization into xy plane

The degree of tipping is dependent on the amplitude and duration of the RF pulse. At this point the bulk magnetization vector has been tipped into the xy plane and is still precessing around the static magnetic field. This rotating magnetic vector will produce electromagnetic radiation (see Figure 32). This energy is emitted as protons transition from the higher energy state back down to the lower energy state, and will be in the radiofrequency range in this instance. If a receiving coil is placed in a plane perpendicular to the protons precessing magnetic moments the maximum signal will be induced or received.

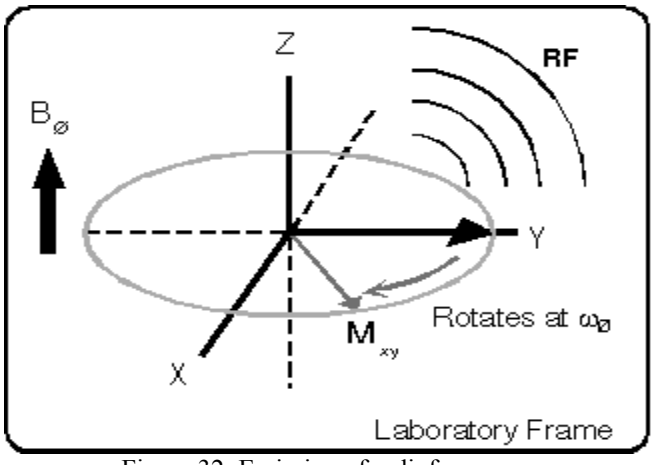

Figure 32: Emission of radiofrequency

When the RF pulse is turned off three actions occur.

1. The absorbed RF energy will be re-emitted at the resonance frequency
2. The excited protons magnetic moments begin to return to their pre-tipped orientation along the z axis.
3. The excited protons magnetic moments begin to dephase.

Points 2 and 3 are called relaxation processes and occur independently of each other while simultaneously contributing to the loss of MR signal intensity. Both of these actions can be modeled as exponential decay processes and are described by time constants T1 and T2 respectively. The act of the realignment of the bulk magnetization with the z axis occurs through spin-lattice interactions, which is to say from interactions involving resonance protons and the rest of the material the "lattice". While the dephasing of the protons magnetic moments is regarded as a spin-spin interaction, which is to say interactions involving two or more resonance protons. Specifically the T1 time, is the time it takes for the original MR signal to decay to ~ 37 % of its initial value solely by spin-lattice relaxation. T2 is similarly defined as the time for the initial MR signal to decay to ~37% of its initial value solely by spin-spin interactions. In reality, the calculated T2 time is not observed in samples due to magnetic inhomogeneities in the field. Because of these inhomogeneities all the protons will not be precessing at exactly the same frequency which will cause more rapid dephasing than if caused by purely random spin-spin interactions. Furthermore some materials in the sample will exhibit differences in magnetic susceptibility which will cause localized perturbations in the magnetic field, again causing rapid dephasing. Because of this an effective T2 time is

observed and is denoted by T2*. It should be noted that spin-spin relaxation is always less than spin lattice relaxation. If T2* is similar to T1, then T1 may have a significant impact on the signal at time t. However in cementitious materials, T2* times are usually much shorter than T1 times and the signal strength becomes dominated by spin-spin interactions.

In cementitious materials, especially those using fly ash and blast furnace slag, paramagnetic and ferromagnetic iron oxides cause rapid dephasing, and T2* times under 100 μs occur, that tend to decrease with increasing iron content[106]. This extremely short T2* time makes imaging cementitious materials with high iron contents difficult and often precludes normal imaging sequences.

Although MR of cementitious materials with high iron content has its issues, MR has the advantage of being able to distinguish bound water from free water as the two have different resonance frequencies. Additionally many ions such as ions of lithium and chlorine can be tracked with MRI and magnetic resonance spectroscopy (MRS) as they have distinct resonance frequencies[76,90]. Even atoms of the same type but different bonding states can often be distinguished due to the chemical shift in resonance that occurs[102]. MRI and MRS have become extremely versatile tools in materials science research, and researchers are currently attempting to improve techniques and electronics so materials containing higher levels of paramagnetic and ferromagnetic materials can be inspected with MR.

Micro-Computed Tomography (μCT)

Computed tomography is the 3D analogue of 2D radiography. Where 2D radiography failed to show depth, CT achieves this by taking multiple 2D projections in one plane at different orientations and then using reconstruction algorithms to form the 3D representation (see Figure 33).

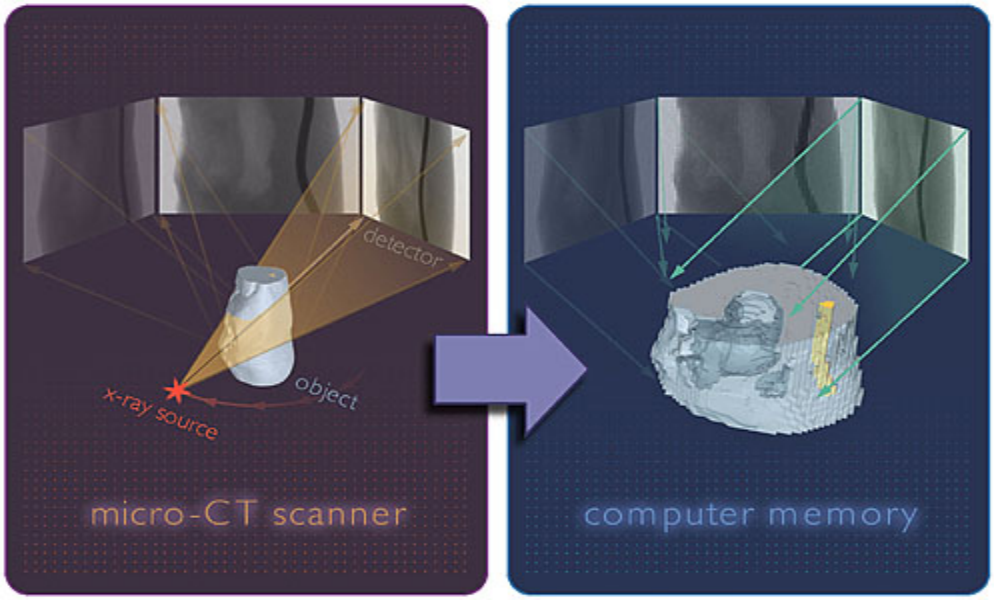

Figure 33: How microCT takes an image

Unlike modern full size medical CT units that use an x-ray source that moves around a ring of detectors with a stationary subject at the center of a ring, many microCT units (but not all) do the opposite. That is they rotate the sample and use a stationary source (Figure 33 is ambiguous in that detail). This rotation is usually performed with a precision stepper as each movement needs to be precise for proper image reconstruction.

Like 2D radiography, CT uses maps of linear attenuation coefficients to form images, and may use either a tube or a synchrotron for its x-ray source, although filtered tube sources are much more common. Volume elements called voxels are constructed in

CT, with each voxel having an associated linear attenuation coefficient assigned to it. These linear attenuation coefficients are correlated to gray-scale values and are displayed on a computer screen. Traditionally CT has used Hounsfield units (aka CT numbers) to perform this scaling. Originally the Hounsfield scale was based on a scale that ranged from -1000 to + 1000 with the linear attenuation coefficient of water being set to zero, air to -1000, and compact bone to + 1000. Many modern systems have extended this range but the concept is the same. The formula for determining Hounsfield number is below.

$$\frac{\mu_x - \mu_{H2O}}{\mu_{H2O}} x1000 \qquad \text{Equation 4}$$

where μ_x is the linear attenuation coefficient of the substance x, and μ_{H2O} is the linear attenuation coefficient of water.

In microCT, which was used in this investigation, very small focal spots on the order of 2-5 microns can be achieved that can produce effective pixel sizes of a few microns[107]. These tiny focal spots are necessary to produce the extremely high resolution images desired. This concept can be illustrated by a simple ray diagram (Figure 34) located on the top of the next page. The lack of sharpness caused by finite sized focal spots is called ‘penumbra’.

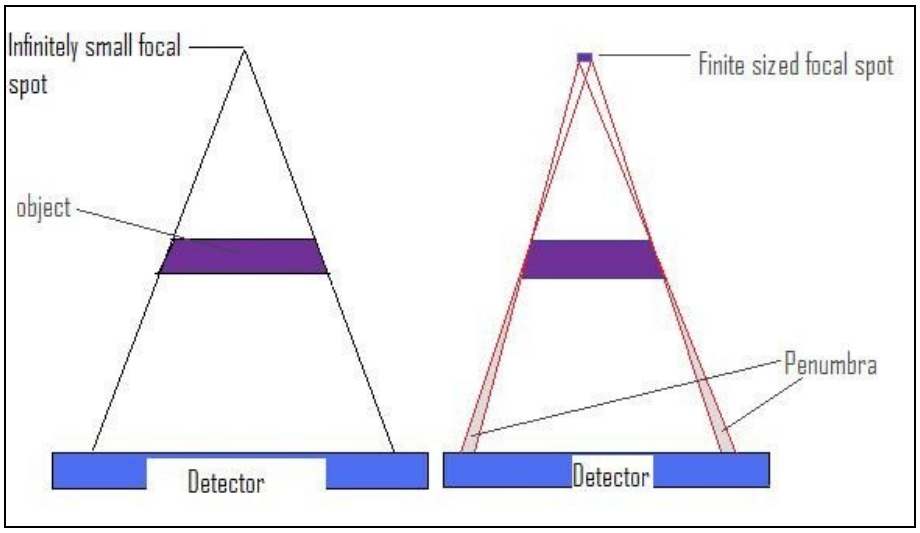

Figure 34: Penumbra caused by a finite sized focal spot

MicroCT has been used to track moisture distribution by several researchers. Some of these uses included tracking moisture redistribution from prewetted light weight aggregate in curing concrete and fluid flow through methane hydrate bearing sands[90,108]. Although this has been somewhat successful, even after careful selection of x-ray technique (mas, kVp) significant postprocessing is usually needed to clearly see fluid in porous media. CT is more often used to estimate fluid flow or distribution by changes in linear attenuation coefficients from reference samples, i.e. dry then wet comparisons. In low to moderate porosity materials, or materials with a small average pore size, this change is often not seen by the unaided eye.

Although microCT has shown it is not ideal for visualizing water without significant postprocessing it does have numerous other advantages. These include:

- The ability to define and map a wide range of structures even if significant iron content is present, this is not true of MRI as its performance suffers with increases in iron content. Neutron radiography, while highly sensitive to water, is only sensitive to a limited number of atoms, the others appear

virtually transparent. PET is also inferior in this manner, as it shows poor contrast due to the high energy of the annihilation radiation and poor spatial locating ability due to uncertainties.

- Resolution that is often superior to MRI, and always to PET (microns vs mm resolution)[102]
- The sample is non-radioactive, unlike with PET or other radiotracer techniques, which contaminate the sample and add handling and disposal restrictions.
- The ability to use contrast tracers to aid in water detection and to simulate ion intrusion. For example chloride ion transport is of concern and can be modeled with iodine salt solutions. Since iodine is in the same column of the periodic table as chlorine it should react similarly, and is an excellent contrast agent for low energy x-ray applications.

CHAPTER III

EXPERIMENTAL APPROACH

The purpose of this investigation was to develop a methodology for tracing intrusion profiles for water and ionic species in cementitious materials using μCT. Since this method involved a significant amount of technique development, a "scoping study" was implemented to parameterize the μCT settings, to determine appropriate sample sizes and to develop a statistical method of locating intrusion fronts. Additionally a later "proof of concept" study was initiated to investigate the potential use of potassium iodide (KI) as a contrast agent to improve front location and image definition and to further refine post-scan data processing procedures. Once these preliminary studies were completed subsequent demonstration experiments were conducted in the following three phases:

- an ionic transport study measuring the intrusion rate of I^- from a 3 M KI solution into saturated cementitious samples,
- an ionic intrusion study measuring the rate of iodine diffusion into samples held at 70% relative humidity (RH), and
- a water intrusion study measuring the rate of intrusion of a 3 M and 1 M, KI solution into samples equilibrated to 32% RH.

The general procedure for all demonstration experiments was to condition samples of Portland cement-based materials to various levels of RH or saturation (e.g., oven dry, 32% RH,70 %RH, or, fully saturated), add the appropriate intruding media to the

attached reservoir, scan the samples on the Scanco Medical μCT 40, and post-process the raw x-ray attenuation data to provide a series of 2D slice images and intrusion profiles.

In the first demonstration experiment, iodine from a 3M solution of KI in water was allowed to intrude into a fully saturated sample. This scenario was intended to simulate the penetration of dissolved ions (e.g., chloride) into the material. μCT scans for this first scenario were taken at 2 hours after introduction of the KI and then at cumulative intrusion times of 60, 108, 204, 252, 300, 348, and 816 hours. This experiment was run in triplicate with samples of 1A, 1B and 1C.

The second demonstration study was designed to illustrate the ionic diffusion of a pulse of ions, by adding a very thin layer (0.25 ml) of saturated (7.71 M) KI solution onto a sample equilibrated to 70 % relative humidity. Since the volume of KI solution added to the reservoir was small, it was assumed that only transport of iodide ion (I^-) through connected water phase in the pore system was responsible for changes in attenuation The I^- was allowed to penetrate into the sample for 840 hrs (35 days) and scans were performed at 2 hrs after KI introduction and then at cumulative intrusion times of 57, 105, 153, 201, 369, and 840 hours. This experiment was run in duplicate with samples 2A and 2B.

The last demonstration involved the intrusion of 3M (sample 3A) and 1M (sample 3B) solutions of KI into samples conditioned at 32% RH. This study was used to determine the sensitivity of the shape of the water intrusion curve to the concentration of the contrast agent, and to simulate the intrusion of water into a partially-saturated matrix. Scans were taken at 2.5 hours after introduction of the KI solution and then at cumulative

intrusion times of 48, 91,168, 216, 280, 360, and 451 hours. Exact times matching the times for other experiments were not possible due to instrument scheduling conflicts.

CHAPTER IV

EXPERIMENTAL MATERIALS AND METHODS

Cementitious Materials and Sample Preparation

The early test samples produced for use in the scoping study were composed of an ordinary Portland cement paste mixed with a 0.4 water-to-cement ratio (w/c ratio). The samples were originally cast in 60 mL air-tight test tubes and allowed to cure for 28 days at room temperature (20±2°C). The samples were dried in ambient conditions for 2 weeks before scoping experiments commenced. During the scoping study distilled deionized water was used as the intruding fluid into an initially dry sample. Cylindrical samples of 35-mm diameter and less than 75-mm length were dry cut from the cured material with a diamond-bladed tile saw. The sample width and length were limited by the size of the μCT sample holder. The sides of each scoping sample were sealed with paraffin wax to limit capillary action along the edges. A water reservoir of approximately 1 cm depth was created by wrapping electrical tape around the circumference of one edge of the sample. The sample with reservoir was placed into the sample holder for μCT scanning; thus, "real time" scans could be made during the water intrusion phase.

When these first scoping samples proved to be too thick to adequately penetrate with the maximum settings available on the μCT (70 kVp tube voltage, 113 μA tube current), smaller samples were made in one of two ways. A sintered core bit was used to core samples with a diameter of approximately 18.0 mm from various mixes poured into small rectangular plastic boxes (see Figures 35 and 36).

Figure 35: cores and core-bit

Figure 36: plastic pour box

The sides were then sealed with a high-viscosity marine grade epoxy, increasing the diameter to approximately 18.4 mm. A sample length of 3.5 cm was chosen, as this would provide adequate intrusion depth for all experiments, and allowed for a reservoir of approximately 3 times the expected available pore volume of the sample. An acrylic reservoir of approximately 9 mL volume with a wall thickness of 2 mm was then secured to the sample with the same marine epoxy used to seal the sides.

The second method for providing a smaller sample was to mold the samples in a custom book-mold (see Figure 37). The book mold was created from high density polyethylene and enabled multiple samples to be molded at once. The samples obtained from this were 9.2 mm in diameter and approximately 70 mm long.

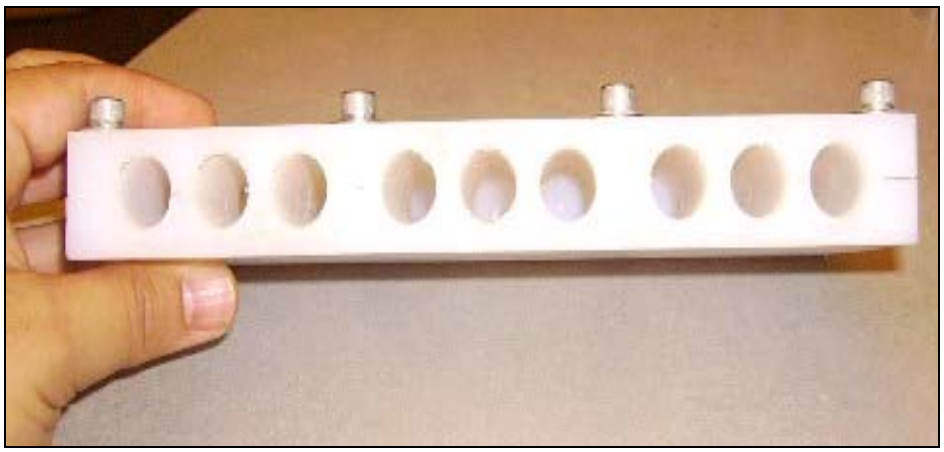

Figure 37: small sample book-mold

Once extracted, these cylinders were cut in half and coated with marine epoxy, as was done with the larger 18.0 mm samples. The reservoirs on these were made from a simple electrical tape wrapping as in the first trial.

The smaller 9 mm samples were scanned dry, and penetration and flux was deemed sufficient, as the reported values in the central pixels did not exceed the linear attenuation coefficient scale of the instrument. Detailed three dimensional images were formed, and individual slices as thin as 10 μm were produced and visually examined.

When the 18.4 mm samples were scanned dry, the penetrating power and the photon flux were also sufficient to reconstruct clean error free images. Once the 18.4 mm samples proved viable the 9 mm samples were removed from consideration as test samples. This was due to large amounts of air entrained in the 9mm samples as well as concerns that they were not representative of larger cementitious slabs.

This air was likely due to the book mold samples not being vibrated during initial mixing. However, the book mold method could be used with larger samples if the samples were properly vibrated, and this would produce much less waste than using bulk disposable molds and cored samples.

For the demonstration studies, a bulk material was composed of Type I/II cement plus blast furnace slag, fly ash and 20-30 mesh Ottawa sand. The components were mixed at a w/c ratio of 0.48 in the proportions in Table 4.

Table 4: Cement sample composition

Components	**Type I/II Ternary Blend 2 [5] kg/m^3 (lbs/cu yd)**	**Composition [%]**
Type I/II Cement (ASTM C 150)	109.8 (185)	**6.33**
Grade 100 Blast Furnace Slag (ASTM C 989)	163.2 (275)	**9.40**
Type F Fly Ash (ASTM C 618)	344.2 (580)	**19.83**
Quartz Sand (ASTM C 33)	1118.7 (1885)	**64.44**
No. 8 Granite Aggregate (maximum 3/8 in) (ASTM C 33)	0 (0)	**0**

The second column in Table 4 shows the approximate composition of a proposed reference grout used in DOE nuclear waste management. The composition of test samples for this project was considered representative of the composition of DOE grouts.

The grout mixture was then allowed to cure in sealed plastic containers for a minimum of 60 days at room temperature (20±2°C). When cured, the samples were cored with a diamond sintered core bit, which produced the seven 18.0 mm samples previously discussed. Prior to moisture conditioning, the sides and bottom of the demonstration samples were sealed with the marine grade epoxy, the acrylic reservoir was attached and the epoxy was allowed to cure overnight.

Samples 1A, 1B and 1C were saturated under vacuum in a water-filled Erlenmeyer flask (see Figure 38). The vacuum was cycled in 30 minutes intervals during the day for approximately 48 hours to remove as much air from the samples as possible.

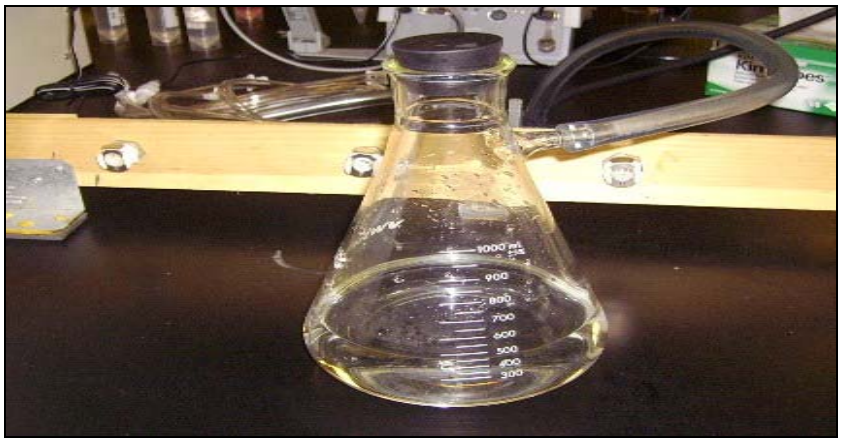

Figure 38: Vacuum apparatus

Partially-saturated samples were allowed to equilibrate at controlled relative humidity for several weeks in environmental chambers at 25 °C with normal atmospheric gas. Samples 2A and 2B were conditioned at 70±2% RH while samples 3A and 3B were conditioned at 32±2 % RH.

µCT Instrumentation and Parameters

The machine used in all scans was a Scanco Medical µCT 40 (see Figure 39). This instrument had been previously purchased to image rodent bones, which are much thinner, and less dense than the proposed cementitious samples. Due to this, higher levels of kVp and tube currents were required to scan the cementitious materials, than those routinely used on the instrument.

Figure 39: Scanco µCT 40

After early scoping study failures involving lower energy techniques a 70 kVp , 113 µA, 200 µs integration time imaging technique was chosen for all remaining scoping, proof of concept and demonstration scans. These kVp and tube current settings were the maximum permitted by the instrument. Although the peak voltage was set to 70 kVp, the mean energy of the x-rays was closer to 35 keV (this was found after several initial experiments had been run) due to minimal beam filtering by the manufacturer.

Method Refinements from the Scoping and Concept of Proof Studies

Water Intrusion Scans (without contrast)

Multiple water intrusion scans were taken on air dried 18.4 mm samples as part of the scoping study with the same maximum x-ray technique used above. The mean linear attenuation coefficient of each slice on the intruding water sample was compared to the mean LAC of the same spatially correlated slice on the same sample, which was previously scanned dry. Slices were considered to contain intruded substances if the slice values were more than 3 standard deviations greater than the corresponding mean slice

value of the dry cores. Because the standard deviation of the mean linear attenuation coefficient of all of the slices was very small (a few hundredths cm^{-1} or less) front location by this means was theorized to be possible.

Several challenges became apparent while attempting to locate water fronts statistically with the above described method. These challenges are related to the unequal distribution of air voids and metal flecks in the nominally homogenous sample. Since air has a very low linear attention coefficient, this would bias the linear attenuation coefficient low, as some slices would have more or bigger air voids than others, creating statistically significant variations in a medium that should be relatively uniform in terms of its linear attenuation coefficient. Conversely, the presence of sizable metallic flecks in the OPC sample would bias the results of a slice to an uncharacteristically high value, as these metallic flecks have very high linear attenuation coefficients. Because of variations caused by metal flecks and voids, seeing the small changes in linear attenuation coefficient caused by water intrusion in a statistically significant manner was impeded.

Another complication arose when the μCT scanner would finish a stack of scans. At this point, the scanner would continue to scan, but a noticeable discontinuity in linear attenuation coefficient might be seen on the first slice of a new scan stack. When the linear attenuation coefficient was plotted versus the slice number, all slices after a stack were shifted either up or down. The cause of this discontinuity however was not verified by the company, but was discussed with other users who have encountered the same issue (Perrien D, personal communication May 2009). This is most likely due to an electronics issue, and may be due to a recalibration of the detector after each stack. Yet another limitation of the statistical technique arose when it was discovered that the linear

attenuation coefficient is accurate to within approximately one percent, this means that changes of less than ~ 0.025 cm^{-1} may not be significant.

Filtering to remove pixels representing low-density air and/or high-density metallic particles was expected to decrease the bias due to heterogeneity. The remaining pixels would represent a more uniform cement paste matrix and its smaller capillary and gel pores. Ranges of linear attenuation coefficients belonging to these features were determined and an Image Processing Language (IPL) script was written to threshold out these features and analyze the remaining pixels.

When the IPL threshold was applied to scans of 18.4 mm samples, the water front appeared to be located on several samples. However, the method was deemed too unreliable due to the very small shift in linear attenuation coefficients between wet and dry samples, and the ~ 1% accuracy of the recorded attenuation coefficient. A greater difference in attenuation between the wet and dry samples was required to conclusively identify wetting fronts.

Contrast Agent and Proof of Concept Scan

Although the linear attenuation coefficient of water is significantly higher than that of air, this alone does not guarantee observance of the front. Since the pixel size used was 30 μm and the majority of the water containing pores is smaller than this, very few pixels would have been detected as pure water. The effect of partial volume averaging then occurs. Partial volume averaging is defined[109] as:

> "whenever a structure is only partly within the imaging section, pixel or voxel. The consequence is that the signals (MR), densities (CT) or count densities (SPECT and PET) of the structure and the adjacent or surrounding structures present in the section, pixel or voxel are

> averaged. As a result erroneous pixel or voxel signal values result. This can lead to diagnostic misinterpretations."

If water did intrude, it would in fact increase the apparent density of the pixel, but since only a small percentage of that pixel may actually contain water, the difference might be smaller than expected. Additionally since the x-ray beam was much less filtered than expected, the broad range of energies contained in the beam caused a broad range of attenuation, further degrading delineation of the front.

A contrast agent was thus sought that would more strongly attenuate the x-ray spectrum from the imaging device. When working with a matrix with so many constituents, it becomes difficult to predict chemical interactions or provide a contrast agent that is completely nonreactive. An ideal tracer would not bind to the matrix, would not react with any matrix constituents, would be miscible and would have a high solubility in the chosen solvent. Furthermore since the energies comprising the x-ray beam are low, the dominant photon interaction is photoelectric absorption. Thus the tracer should have a large cross section for photoelectric absorption around the mean energy of the beam, which was around 35 keV.

A standard bound iodine CT contrast agent, "Opitray 320", was considered, as its K-edge is at ~33.2 keV (see Figure 40), which was very close to the estimated mean beam energy. The chemical formula of the Optiray contrast agent is N,N'-Bis (2,3-dihydroxypropyl)-5-[N-(2-hydroxyethyl)–glycolamido]-2,4,6-tri-iodoisophthalamide. Optiray is nonionic and is not considered to dissolve in aqueous solution[110].

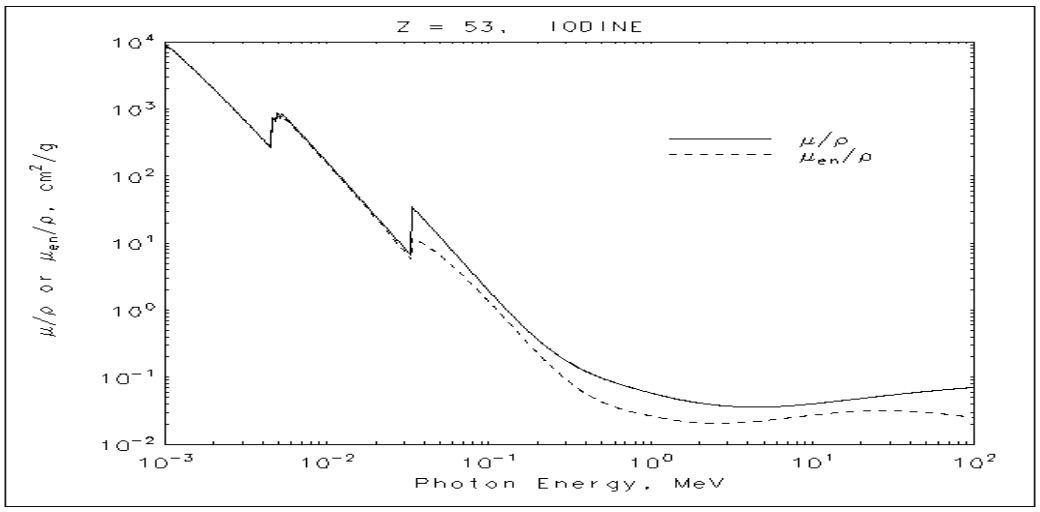

Figure 40: NIST mass attenuation and absorption curves for iodine.

Tests were run with Optiray and the solution, as expected, contrasted well with the concrete. Optiray however is not miscible with water, and its thick viscosity and large molecular weight of 807.11 amu excluded it as a practical contrast agent for imaging small water filled pores[110].

Since plain diatomic iodine exhibits low aqueous solubility, iodine salts, namely sodium iodide (NaI) and potassium iodide (KI), were considered. Sodium iodide has a higher solubility and a higher percentage of molecular weight in iodine, while KI is widely available and inexpensive, while still maintaining a large solubility and reasonable percentage of iodine in its molecular weight. Trials with different molar solutions of KI showed that a 3 molar solution was more than adequate to provide the desired contrast. This concentration of KI represents less than half the maximum molarity possible in a saturated water solution at STP, which is approximately 7.71 M.

An air dried 18.4 mm "proof of concept" sample was scanned while a 3M KI solution was allowed to intrude over a 2 week period. The curves of the mean linear attenuation coefficient per slice were plotted against slice number. The first proof-of-

concept curves are displayed in Figure 41 and exhibit some peculiarities that will be explained. In this figure the intrusion front appears to be bimodal which is likely explained by the rapid filling of smaller connected capillary pores, followed by the slower infilling of larger pores (or less well connected pores) behind the front. The curves recorded at the last two time steps (i.e., 497 minutes and 689 minutes) show a decrease in attenuation behavior in the first ~100 slices. This is due to the fact that the small crude electrical tape reservoir used in the "proof of concept" scan was insufficient for the extended scan times due to its small size (allowing concentration instability), and evaporation undoubtedly occurring. It is believed these later graphs actually show a pulse of iodine passing through the sample as the reservoir dried. The stack discontinuity discussed previously is clearly shown in the attenuation profile taken at 60 minutes.

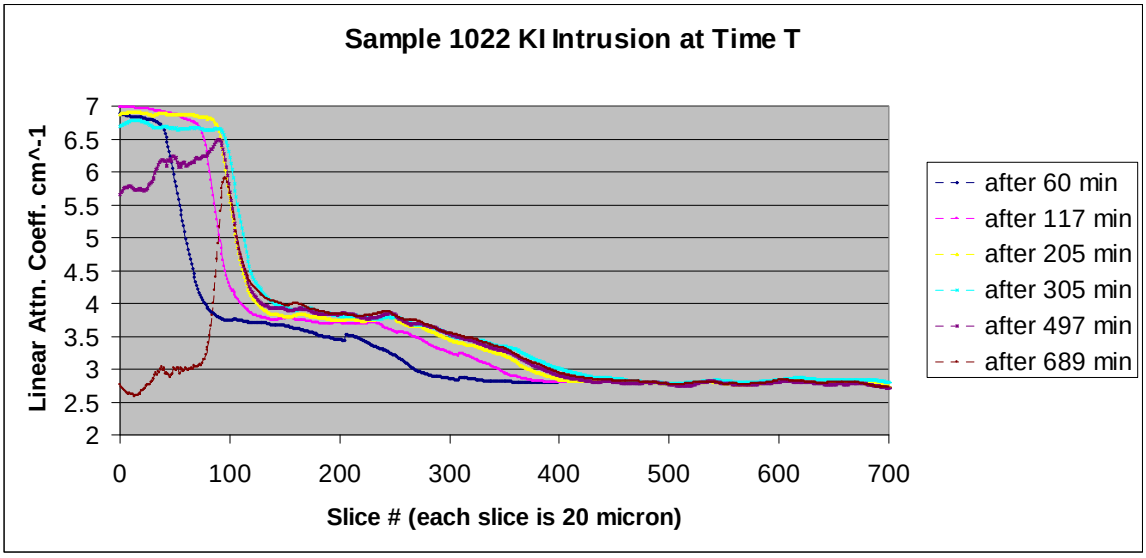

Figure 41: 1st proof of concept trial with 3M KI solution

The shortcomings observed during the proof-of-concept scans were addressed by developing a larger acrylic reservoir capped with Parafilm M, and stabilizing the iodine solution by raising the pH above the pH need to reduce volatility of iodine in solution. pH

adjustment was made by adding small amounts of sodium hydroxide until the solutions pH was ~12.5 which was chosen to approximate the pore solution of Portland cement paste[111].

Front Location Methodology

For all μCT scans, the depth of the penetration front was found by finding the steepest significant slope of the curve and passing a linear trendline along this slope, through the point where the slope decreases (changes shape and shallows), and to the baseline as shown in Figures 42 and 43. For the purposes of this study, the point at which the baseline is intersected by this linear trendline is considered to be the depth of the intrusion front.

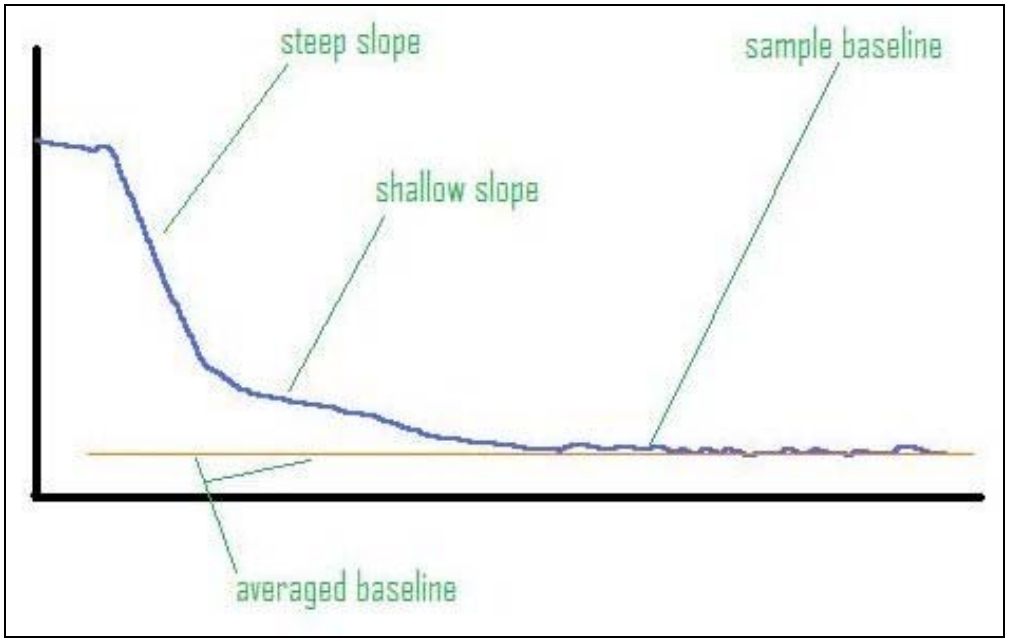

Figure 42: Curve features.

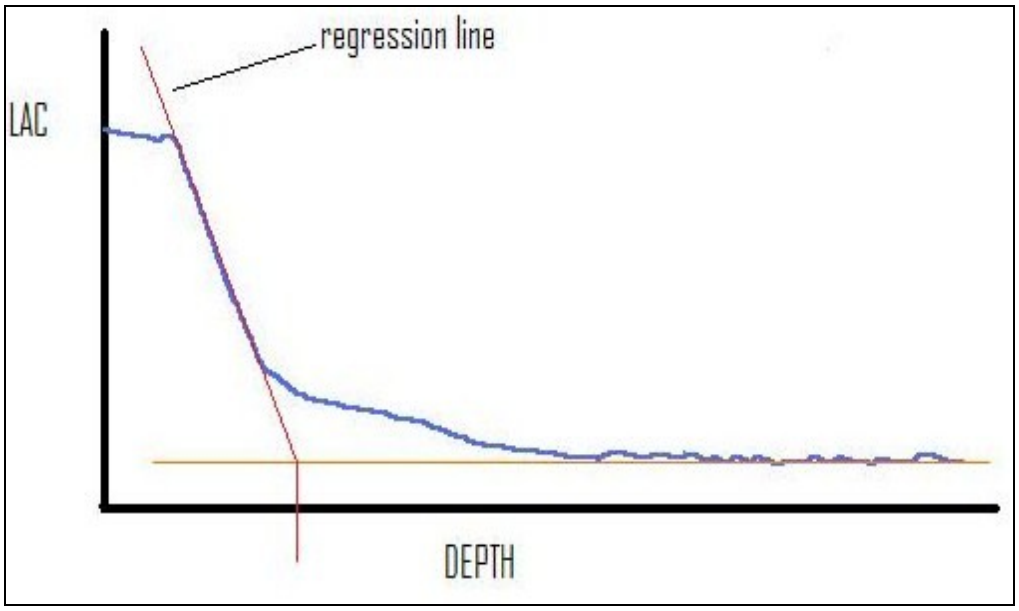

Figure 43: Depth determination with steep slope method.

Depth points were plotted against the square root of time, which is consistent with the generalized transport equation (Equation 1) and the diffusion into a semi-infinite medium with constant boundary conditions[112]. R^2 values were fitted to see if the empirical data followed this mathematical prediction.

This "steep slope" method was chosen over merely following the curves across the baseline (i.e., "shallow slope" method) for several reasons.

- The baselines were observed to vary in attenuation by as much as 0.2 cm^{-1} such that the slope of the curve near the baseline was not consistent from scan to scan. The "shallow slope" method would show the inconsistencies in depth versus time leading to errors in data interpretation (e.g. a scan taken at 8.5-days of cumulative intrusion scan may appear to have a deeper front than a 10-day scan). The 2D images clearly displayed a ragged nonplanar edge (fingering front) that varied from sample to sample, which is most likely indicative of capillary suction ahead of the

main intrusion front. Thus the degree of intrusion front fingering between samples and scans would significantly change the depth prediction if any method utilizing points within 0.4 cm^{-1} were used (i.e., “shallow slope” method).

- Additionally, the response of the instrument is known to be temperature sensitive, and room temperature during the different times of day that scans were conducted varied by as much as 5°C. Thermal issues were believed to be the reason for the baseline shift from scan to scan. The steepest slope method also ensured that a front with a significant volume of water was located, not merely a thin projection of water. This method is somewhat conservative as it will always predict a front less than the extreme intrusion depth while still showing a leading trend.

CHAPTER V

RESULTS AND DISCUSSION

Ionic Intrusion into Saturated Cement Material

This experiment was represented by samples 1A, 1B and 1C in which a 3M solution of KI was allowed to intrude into completely saturated samples. As there was no water gradient, this experiment's purpose was to measure depth intrusion profiles caused by purely ionic diffusion. Graphs associated with these three replicates are displayed in figures 44-52. Each "plot set" belonging to a sample shows in order:

1. the original intrusion profiles
2. a modified intrusion curve showing only the "steep slope" part of the curve, and a regression to baseline for depth determination, and
3. intrusion front profiles plotted as a function of $t^{1/2}$

Total depth penetration over 816 hours was 3.48, 3.36 and 2.79 mm for samples 1A, 1B and 1C, respectively. There was a noteworthy spread in recorded intrusion depths between samples 1C and 1A. This difference was the largest observed between any experimental set, and represented a 0.69 mm discrepancy in depth prediction over 816 hours. The cause of this discrepancy is not currently known. It is interesting to note that the other two samples 1A and 1B agreed very closely with each other, within 0.12 mm over 816 hours. The variance of depth in relation to 1C may be anomalous, or may be a true indication of how different; intrusion rates can be (even in samples from a small

batch) due to differences in microstructure. The average R^2 value for the three "intrusion as a function of $t^{1/2}$" plots is 0.956. Sample 1C which showed the slowest intrusion rate has an R^2 value of ~ 0.96 and thus follows the generalized diffusion behavior at least as well as the other two replicates. Because of this it is suspected that there are real microstructural differences between sample 1A and 1C that contributed to the difference in intrusion rate. Patch microstructure was observed in all images, and Diamond has shown that such patchy microstructure persists even after 30 minutes of mixing[113]. Differences in this patch microstructure may explain the differences between intrusion rates for samples 1A and 1C. When the 3 replicates are plotted together in Figure 53, it appears that the intrusion rates of samples1A and 1B can be described adequately by a single function, but the intrusion rate into sample 1C clearly deviates from this fitted function. Further replicates would be needed before any reliable conclusions could be made.

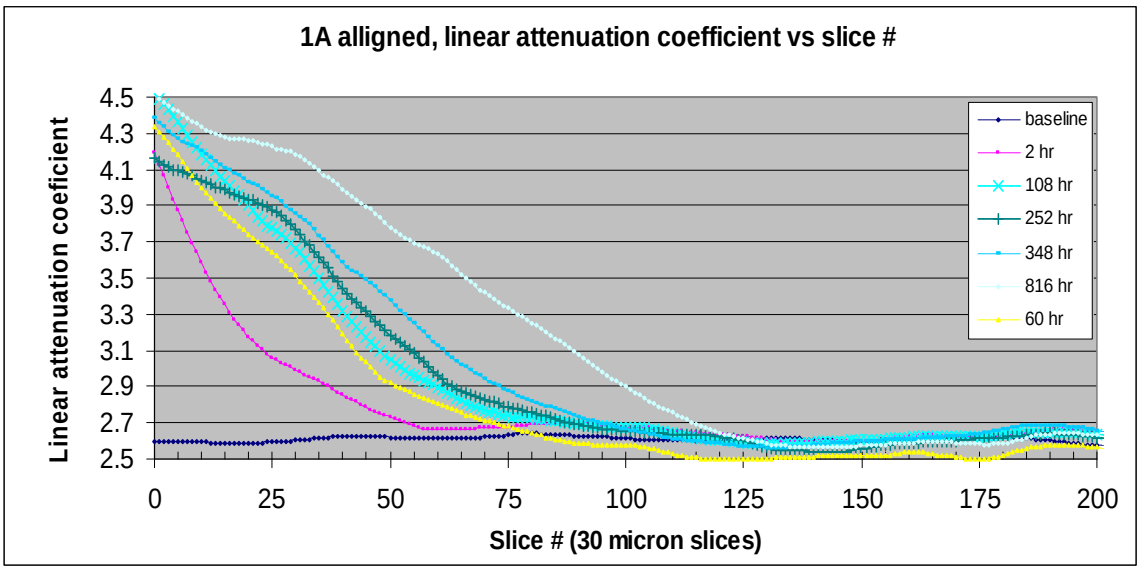

Figure 44: 3M KI intrusion into saturated sample 1A.

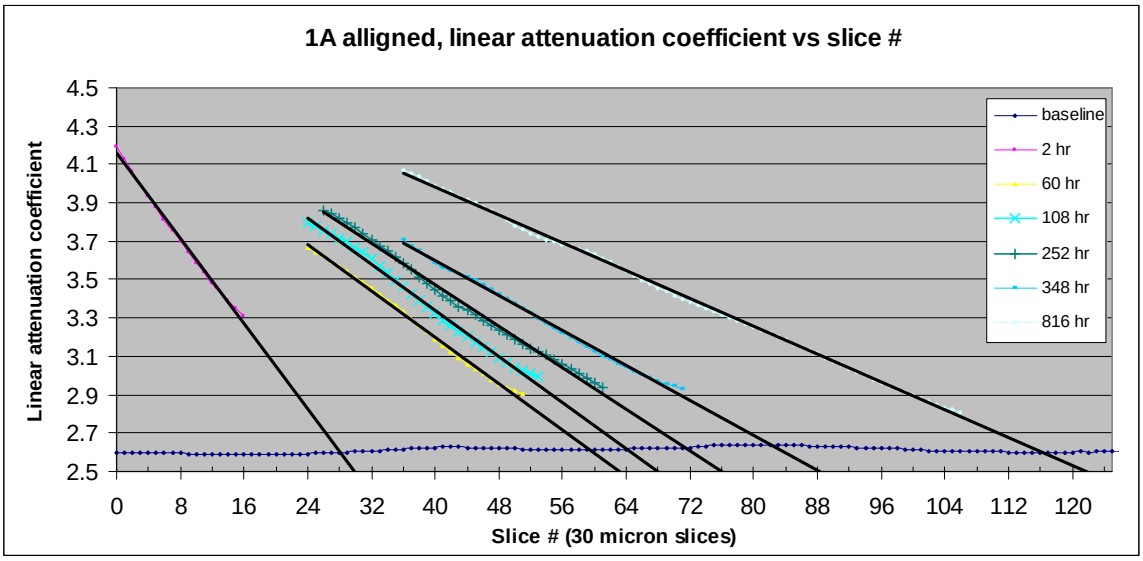

Figure 45: Intrusion profile determination for sample 1A.

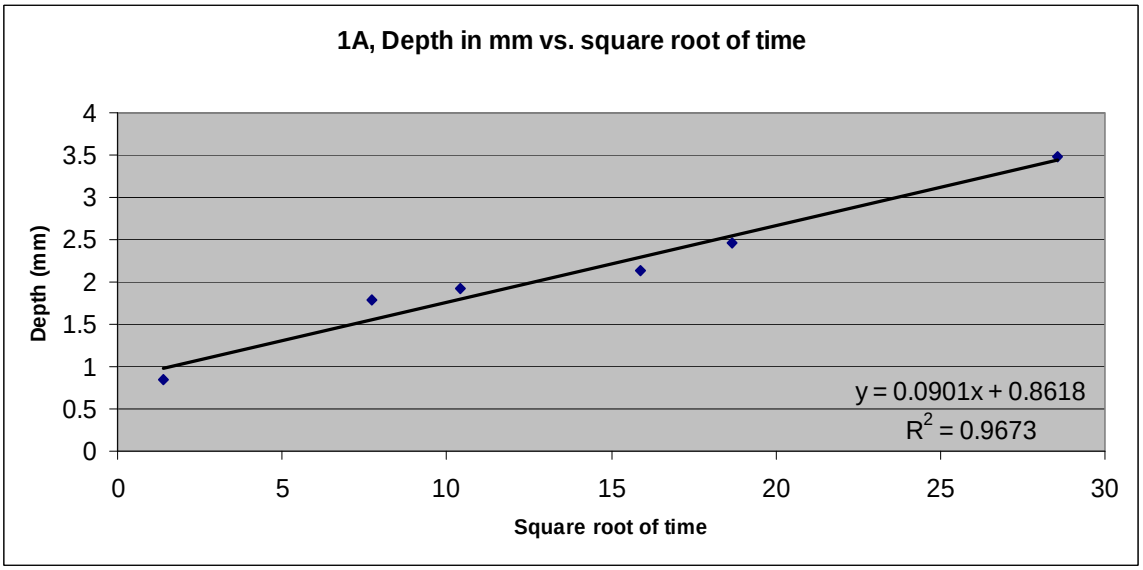

Figure 46 : Intrusion front penetration as a function of $t^{1/2}$ for sample 1A.

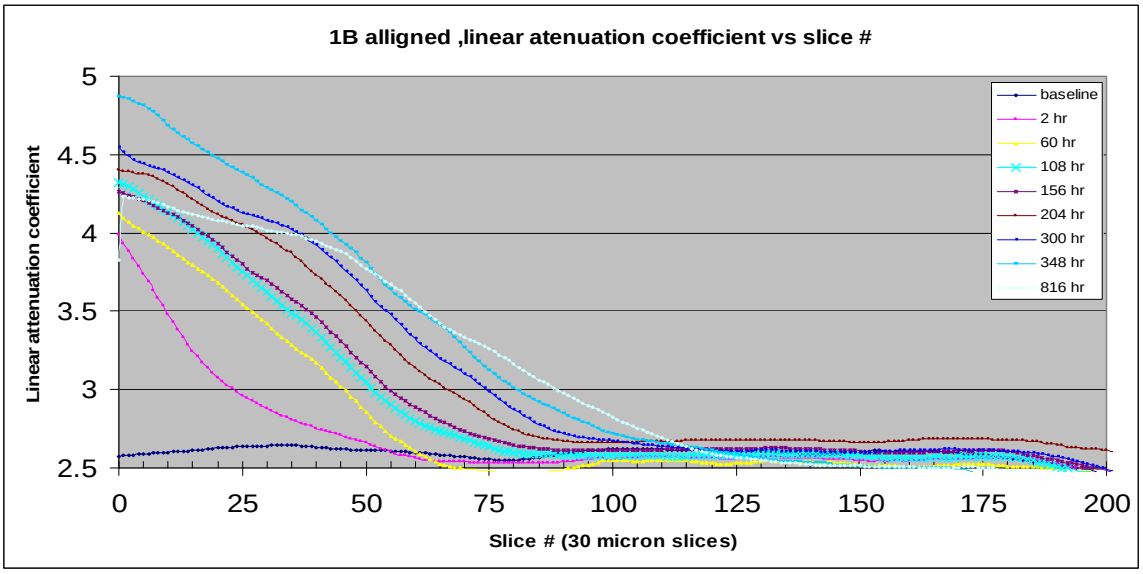

Figure 47: 3M KI intrusion into saturated sample 1B.

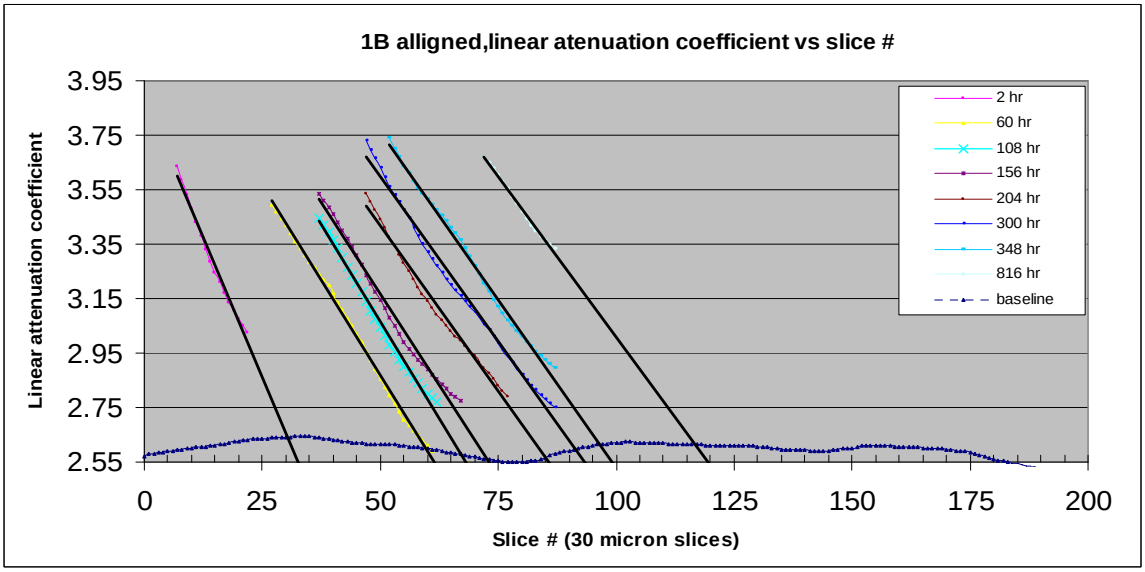

Figure 48: Intrusion profile determination for sample 1B.

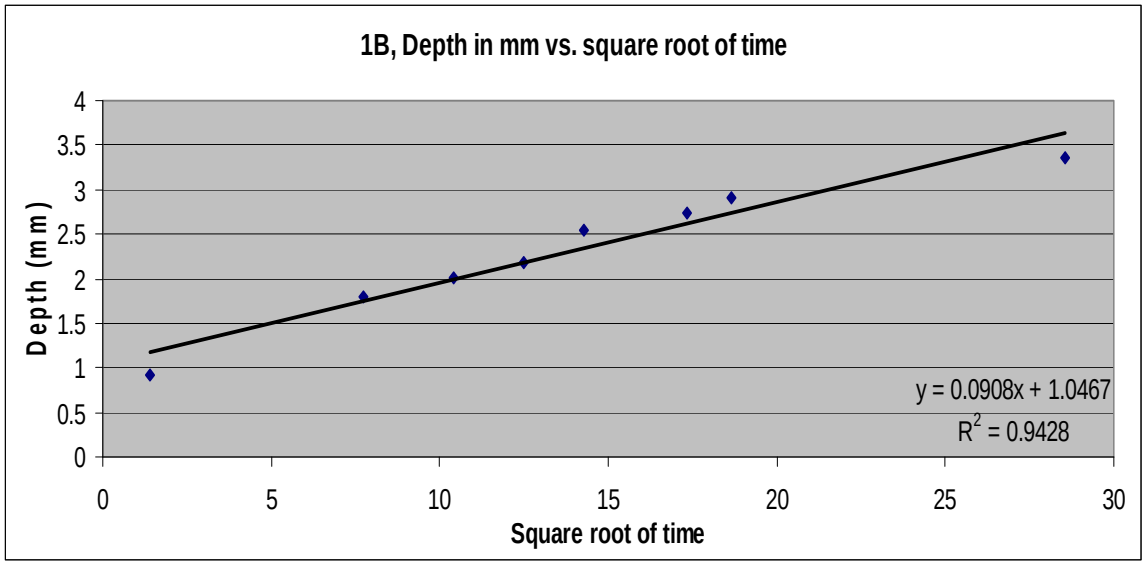

Figure 49: Intrusion front penetration as a function of $t^{1/2}$ for sample 1B.

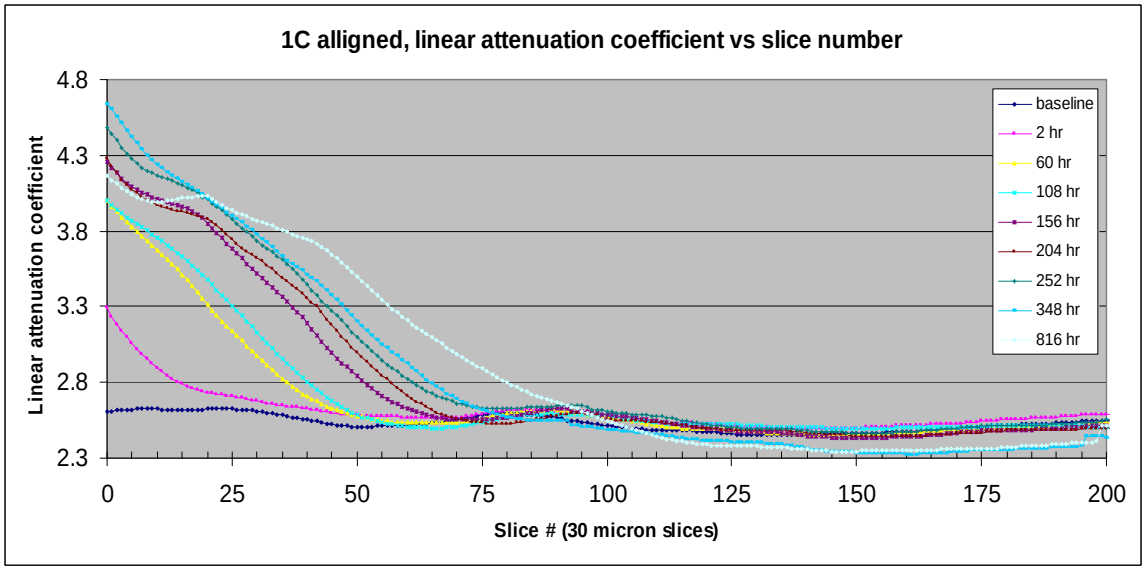

Figure 50: 3M KI intrusion into saturated sample 1C.

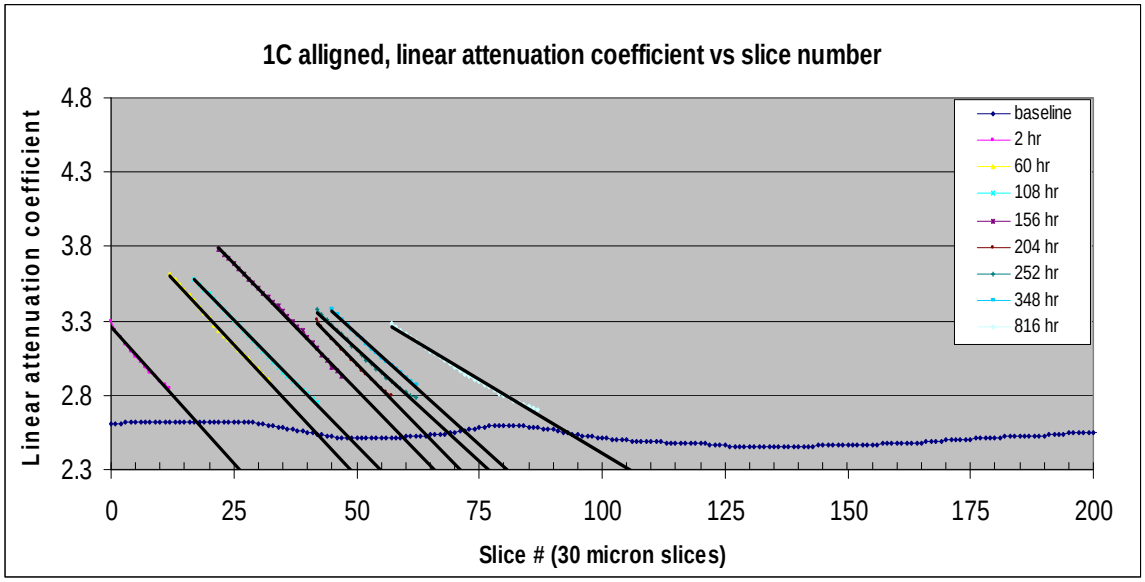

Figure 51: Intrusion profile determination for sample 1C.

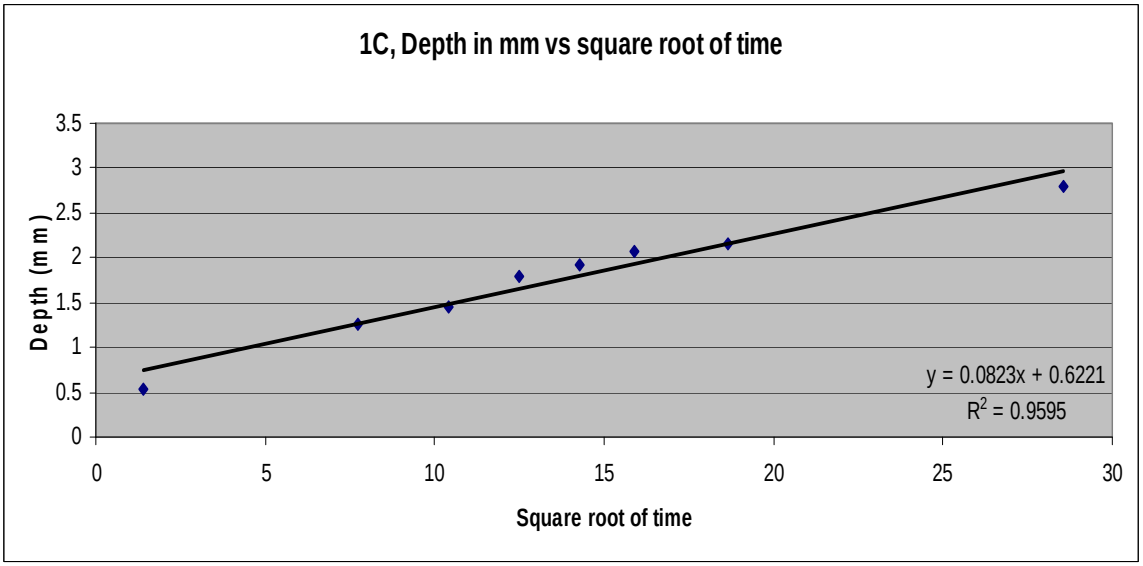

Figure 52 : Intrusion front penetration as a function of $t^{1/2}$ for sample 1C.

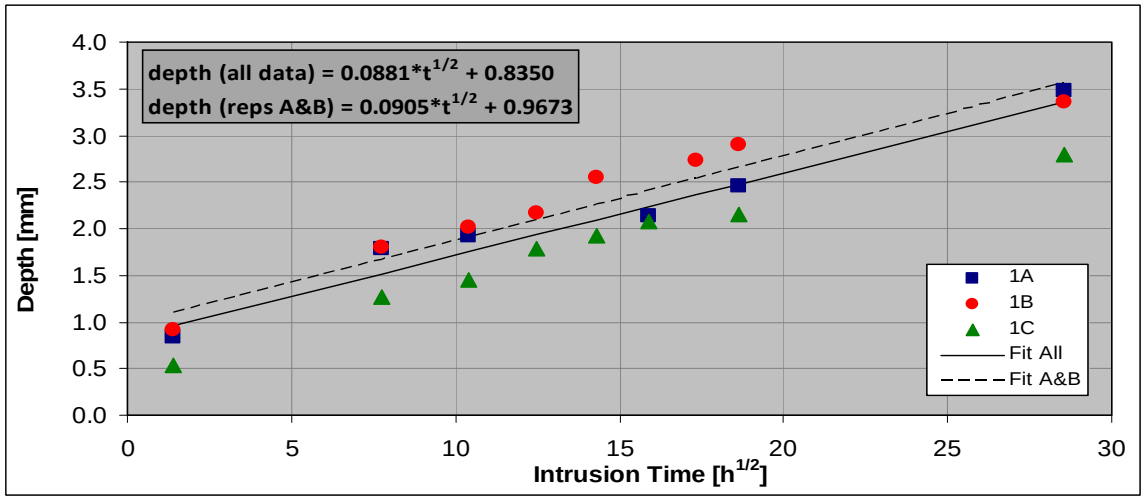

Figure 53: Replicates, intrusion depth as a function of $t^{1/2}$.

Ion Spike Intrusion into an Unsaturated Sample

This experiment was represented by samples 2A and 2B and involved measuring the intrusion of a 7.71 M KI spike of approximately 0.25 ml into a sample equilibrated to 70% RH. Since the ion saturation level was so high and the water content so low, this experiment's purpose was to show intrusion profiles due to pure ionic diffusion into an unsaturated cement material (without a significant water gradient) after a rapid water equilibration phase. These curves are shown in Figures 54-59. These curves produced intrusion depths of 3.165 and 3.045 mm for samples 2A and 2B, respectively, for a total spread of only 0.12 mm over 840 hours. These intrusion curves displayed prominent shoulders and steep slopes with only minimal tailing. This experiment also agreed well with the generalized diffusion equation and produced an average R^2 value of 0.984 with sample 2A having the very high R^2 value of 0.9926 (see Figure 56). This high molarity solution lent itself well to the "steep slope" depth determination method and the data

seemed very consistent, with the curves falling in an ordered predictable manner. When the intrusion depth as a function of $t^{1/2}$ for the replicates 2A and 2B were plotted a single fitted function adequately described the data (see Figure 60).

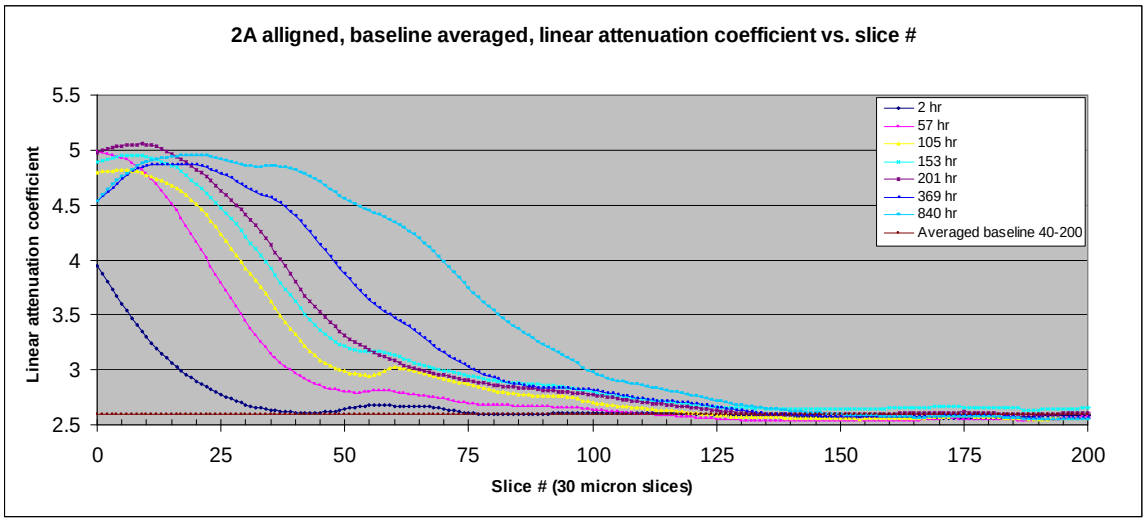

Figure 54: 7.71 M KI (.25 ml) intrusion into 70 % RH Sample 2A.

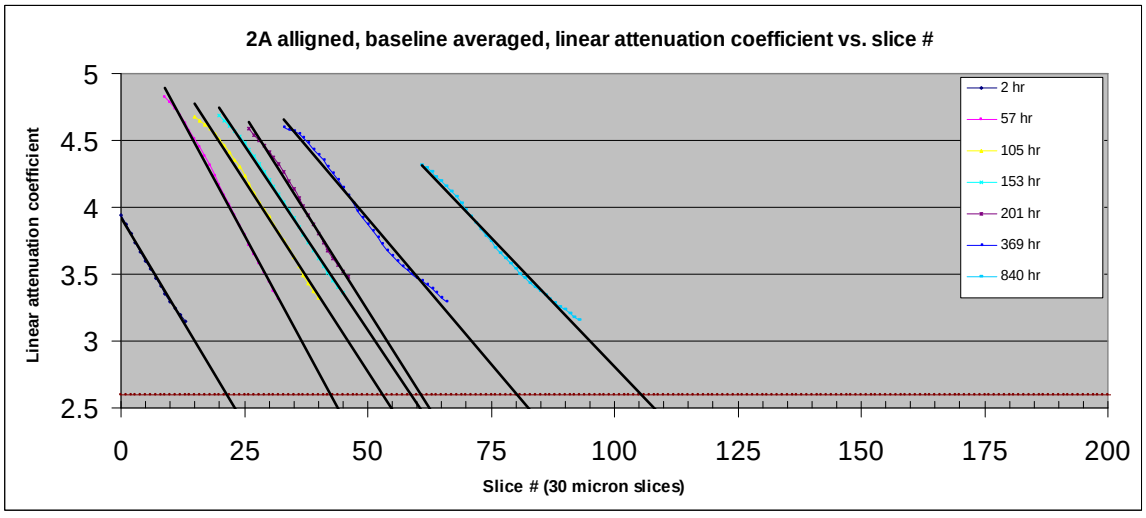

Figure 55: Intrusion profile determination for sample 2A.

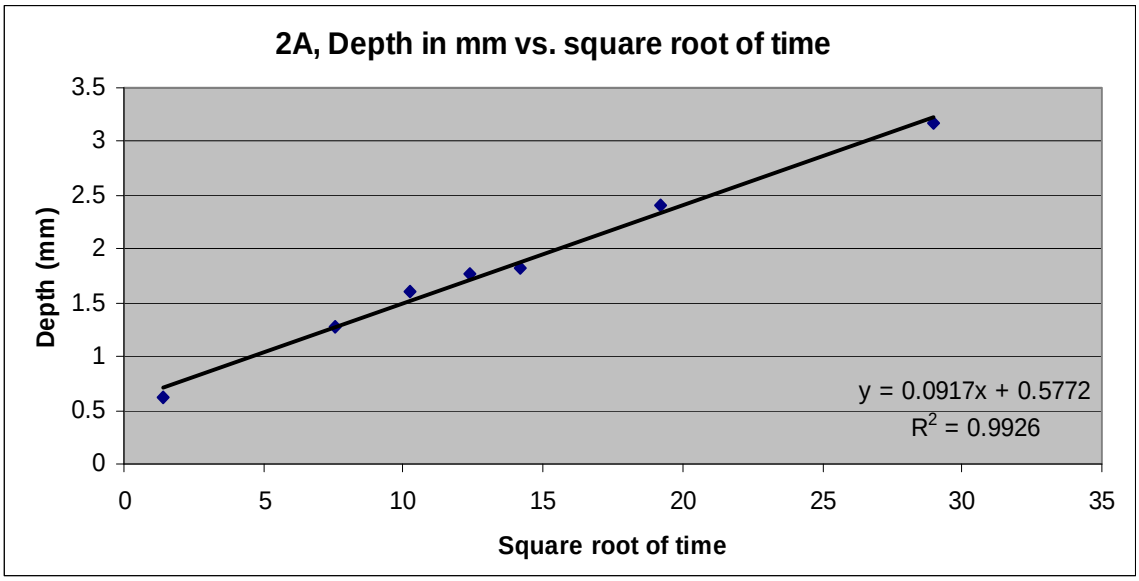

Figure 56: Intrusion front penetration as a function of $t^{1/2}$ for sample 2A.

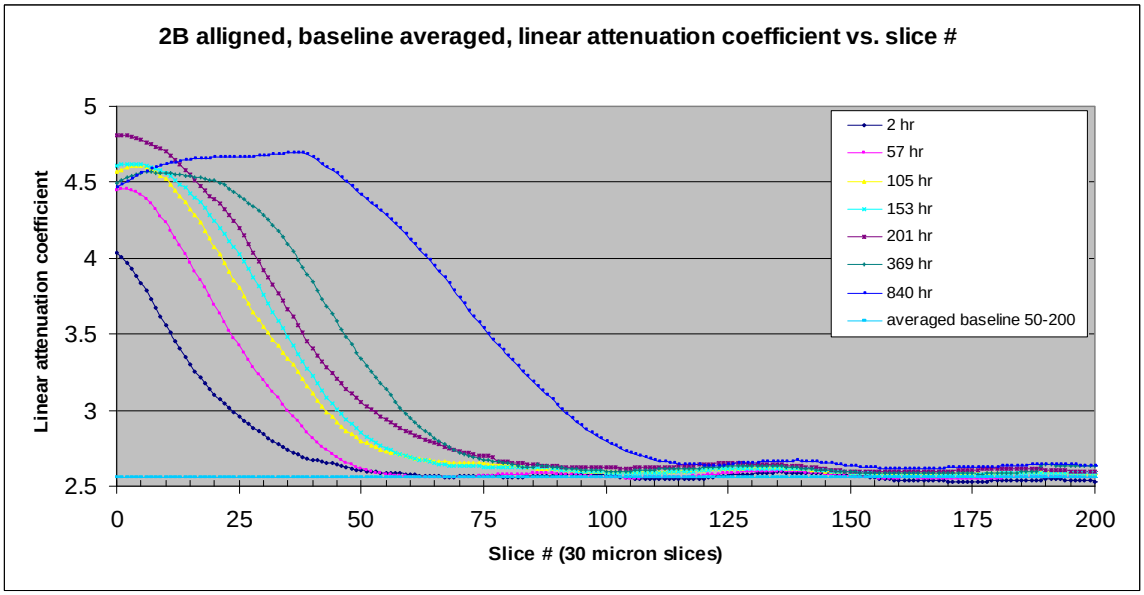

Figure 57: 7.71 M KI (.25 ml) intrusion into 70 % RH sample 2B.

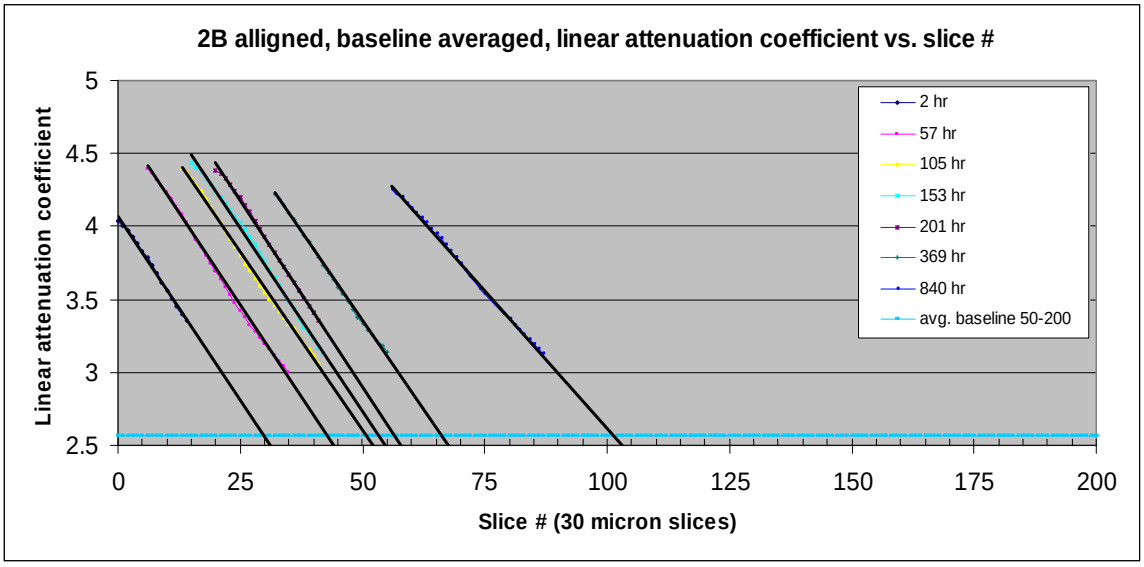

Figure 58: Intrusion profile determination for sample 2B.

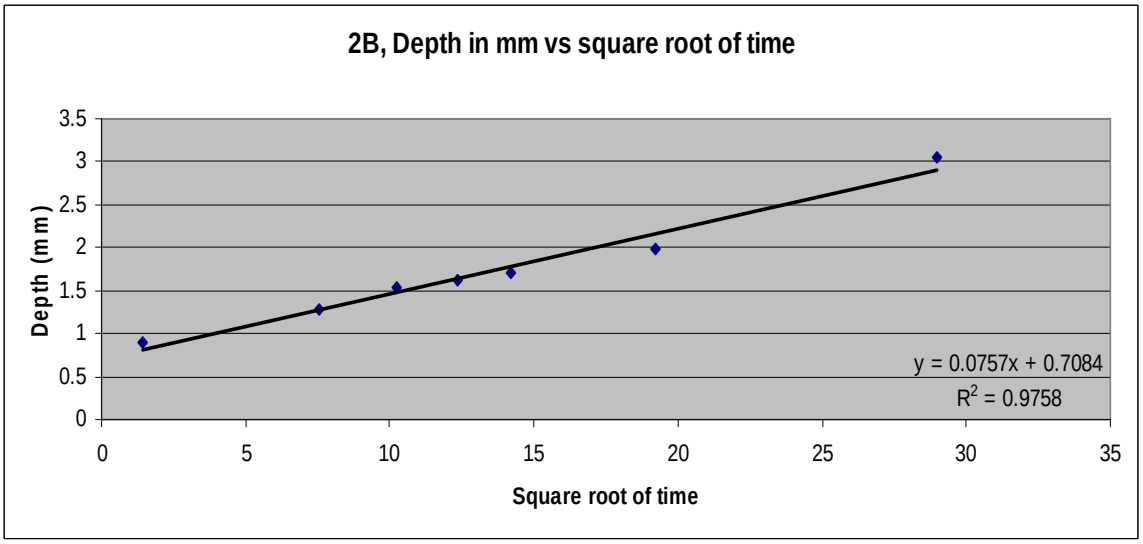

Figure 59: Intrusion front penetration as a function of $t^{1/2}$ for sample 2B.

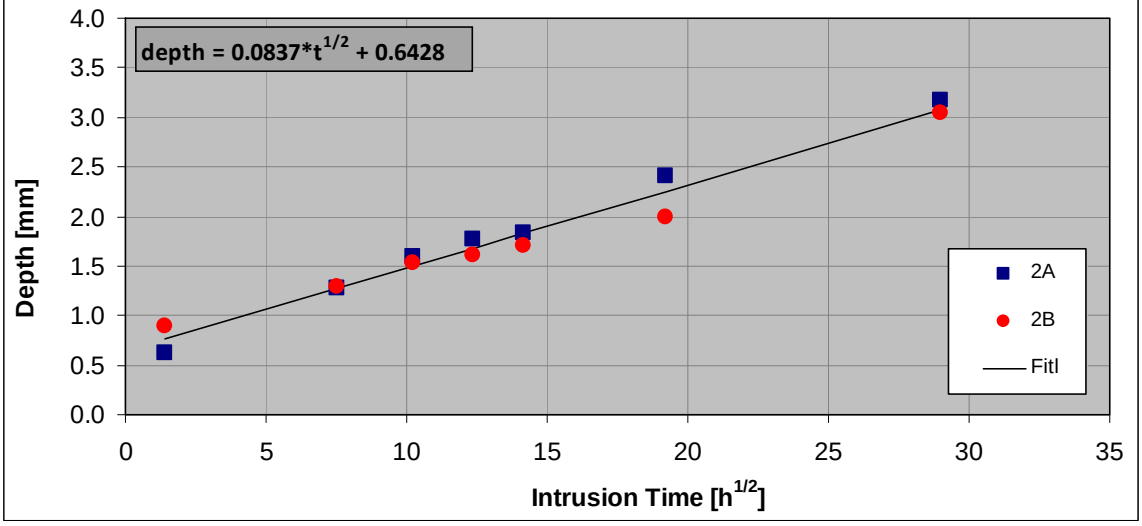

Figure 60: Replicates, intrusion depth as a function of $t^{1/2}$.

Water Migration with Ionic Diffusion, Intrusion Experiment

This experiment examined intrusion profiles of a 3M KI and 1 M KI solution into samples 3A and 3B respectively, which were equilibrated to 32 % RH. This experiment had two purposes. First, since the water gradient in this experiment was considerable, almost all depth penetration was deemed to be driven by the water gradient not the ionic gradient; thus the experiment was to measure water intrusion profiles with the ions considered to be carried by advection. Second, sample 3B was used to determine how lowering the concentration of the intruding KI solution would affect the curve shape and to determine if the steep slope method would still predict depth consistently with the lower concentration.

Figures 61-63 show the result for sample 3A which utilized the 3M KI intrusion solution. Sample 3A displayed the fastest intrusion rate of any sample with an intrusion

depth of 3.855 mm recorded in only 451 hours (see Figure 64). The next greatest depth was recorded on sample 1A, but this took 816 hours to achieve this penetration level. Thus this method indicated that water migration with a significant moisture gradient occurs more quickly than pure ionic diffusion. Lastly, sample 3A results once again yield high R^2 values when intrusion is plotted against $t^{1/2}$ with a R^2 of .988 being produced.

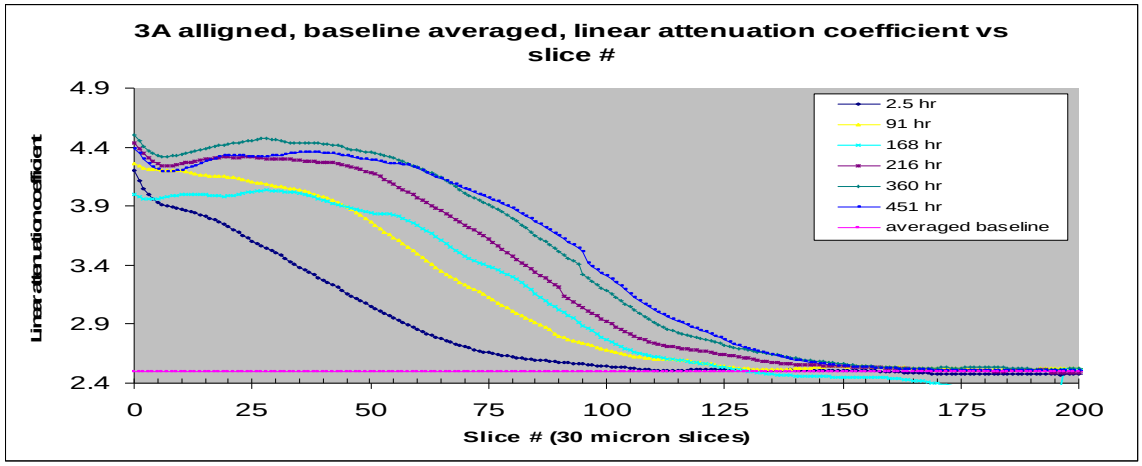

Figure 61: 3M KI intrusion into 32% RH sample 3A.

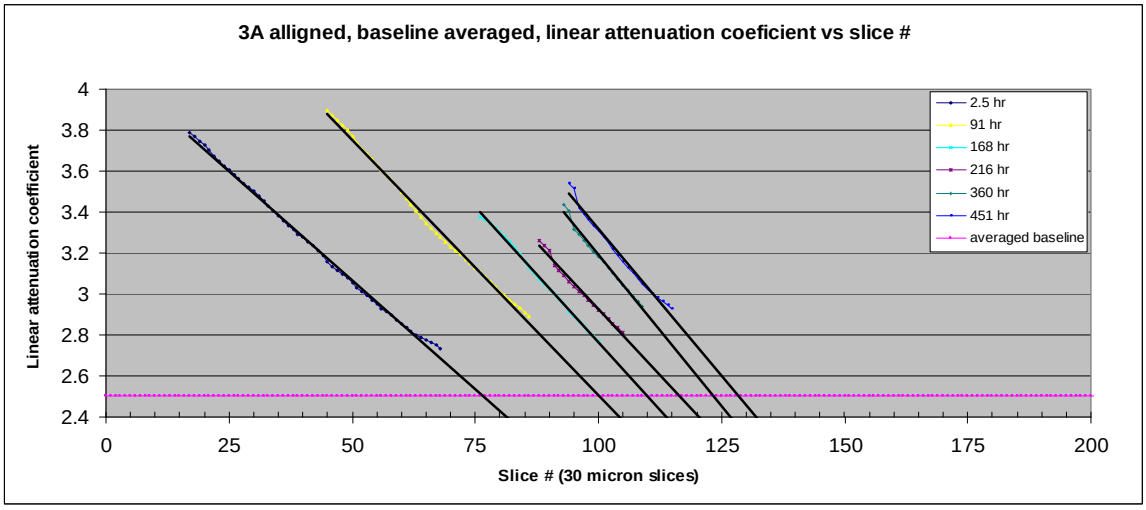

Figure 62: Intrusion profile determination for sample 3A.

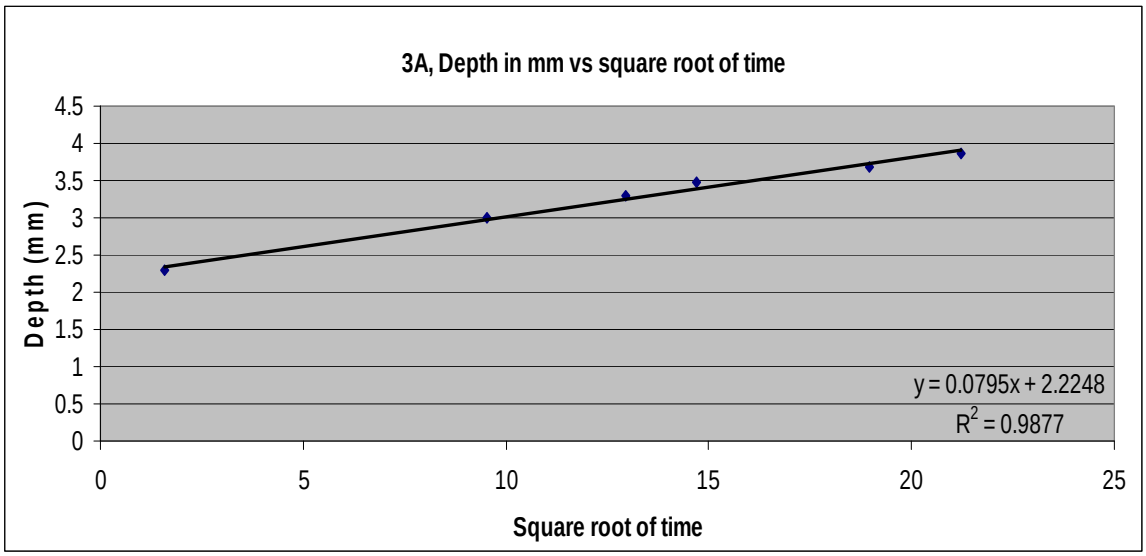

Figure 63: Intrusion front penetration as a function of $t^{1/2}$ for sample 3A.

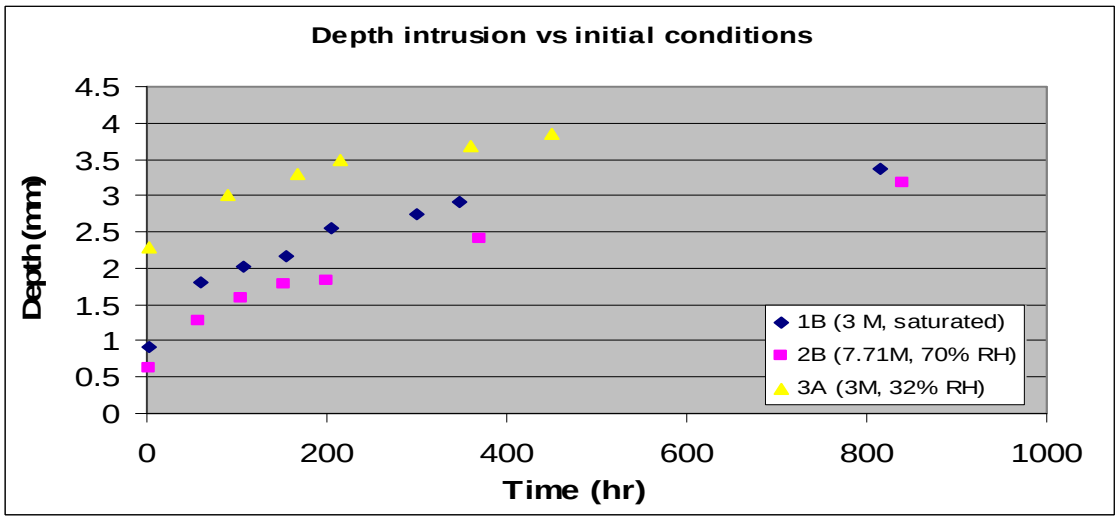

Figure 64: Fastest sample of each group, comparison of intrusion vs. time.

Effect of Contrast Agent Concentration on Intrusion Curves

In each sample except 3B, the plots of depth versus $t^{1/2}$ displayed R^2 values of 0.943 to 0.993 with an average R^2 value of 0.971 for the six samples. This indicates that the developed technique does in fact produce data that corresponds to the commonly used

one dimensional diffusion equation which predicts this result. The initial R^2 value of sample 3B was 0.890. This value was considered abnormally low in relation to the higher values of the other samples. Because of this, the data was reexamined. Since a 1 M KI solution was used in sample 3B instead of a 3M or 7.71 M solution the resulting curves for sample 3B did not exhibit a noticeable shoulder or an easily distinguishable steep and shallow slope. It was determined that the morphology of the curve had changed significantly enough to preclude the use of the steep slope method. For example in Figure 65 if the steep slope method was used; this method would locate the front for the 280 hr scan after that of the 360 hour scan. These curves were eliminated from the data set and the remaining data still produced the lower 0.8897 R^2 value (see Figures 66, 67). When the alternate method was used, which raised the baseline from the mean of the combined backgrounds (2.55 cm^{-1}) to 2.65 cm^{-1}, and then extrapolated the shallow slope to the baseline, the R^2 value rose to 0.997 (see Figure 68, 69). For all 3B curves except the 168 hr curve, the curves were merely followed across the elevated baseline (as this was the same as extrapolation in these cases); but since the 168 hour curve exhibited a long tail that was believed to be part of the baseline, shallow slope extrapolation was performed on this curve. Depth data from this alternate method produced the noticeable rise in R^2 value, and demonstrates that the application of the steep slope method appears to be bounded on the lower end by the concentration of the contrast agent.

These two methods do not predict the exact same front depth however. The “steep slope” method does not predict the absolute far point of ingress but is conservative since it ignores the fringe of the curve, while the ‘shallow slope’ method used in sample 3B with the raised averaged baseline, should predict a more extreme point on the front. The

issue is, whether having a method that predicts the extreme intrusion depth even if it is only a thin penetrating spike of fluid or ions, is more important than finding a more conservative front that contains a greater mass of the intruding substance. If time to corrosion initiation is the metric, then the 'shallow slope' method might be preferable, but if the event requires a larger amount of contaminant contact, then the 'steeper slope' method may be more prudent. The higher the molarity of the intruding solution, the less difference there is in these determination methods, as curves generated with the higher molarity solutions exhibit shorter tails than curves produced with lower molarity solutions. In addition if the 'shallow slope' method is used the average baseline must be raised above the noise level or the tails of the intrusion curves will cross. With better baseline stability this problem should be minimal and trials are underway to characterize the parameters that affect baseline stability.

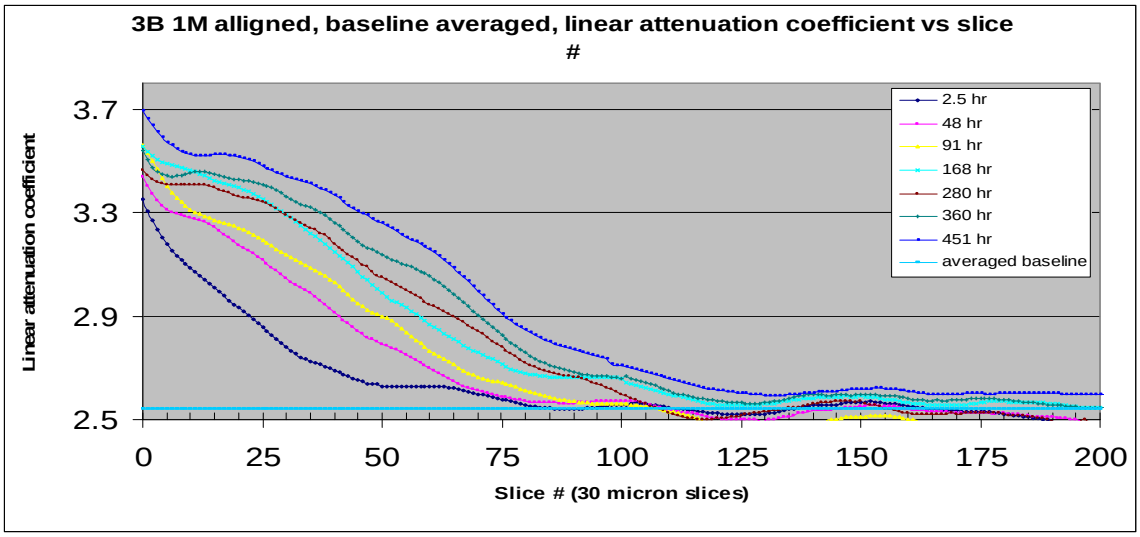

Figure 65: 1M KI intrusion into 32% RH sample 3B.

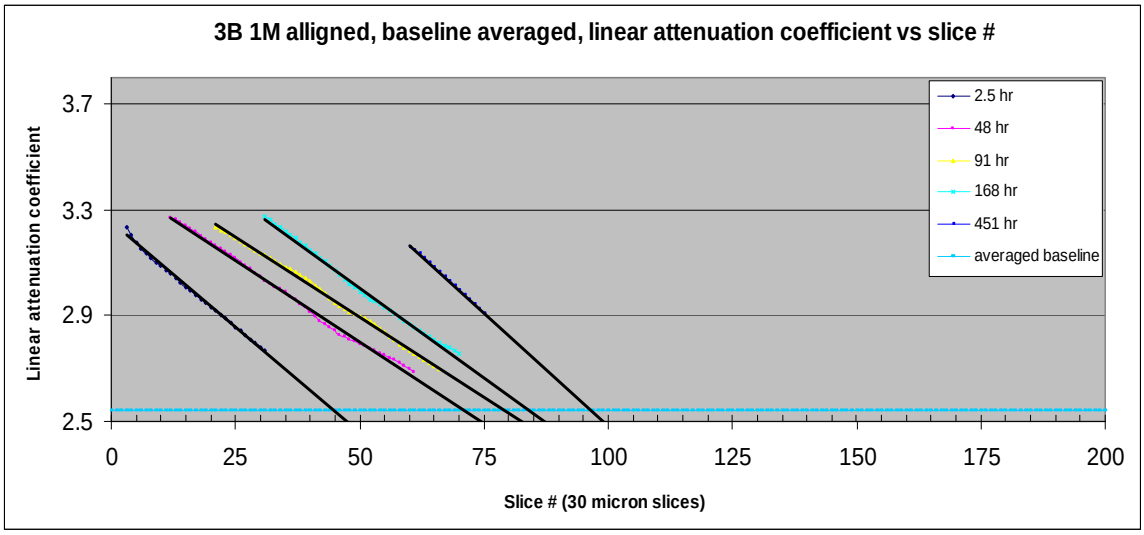

Figure 66: Intrusion profile determination for sample 3B.

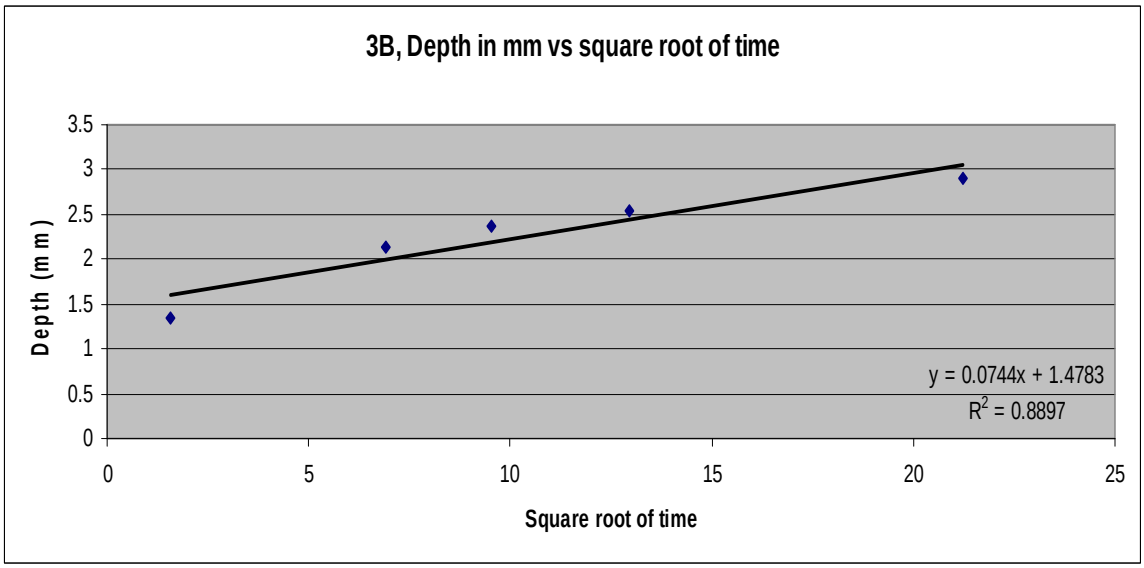

Figure 67: Intrusion front penetration (steep slope method used) as a function of $t^{1/2}$ for sample 3B.

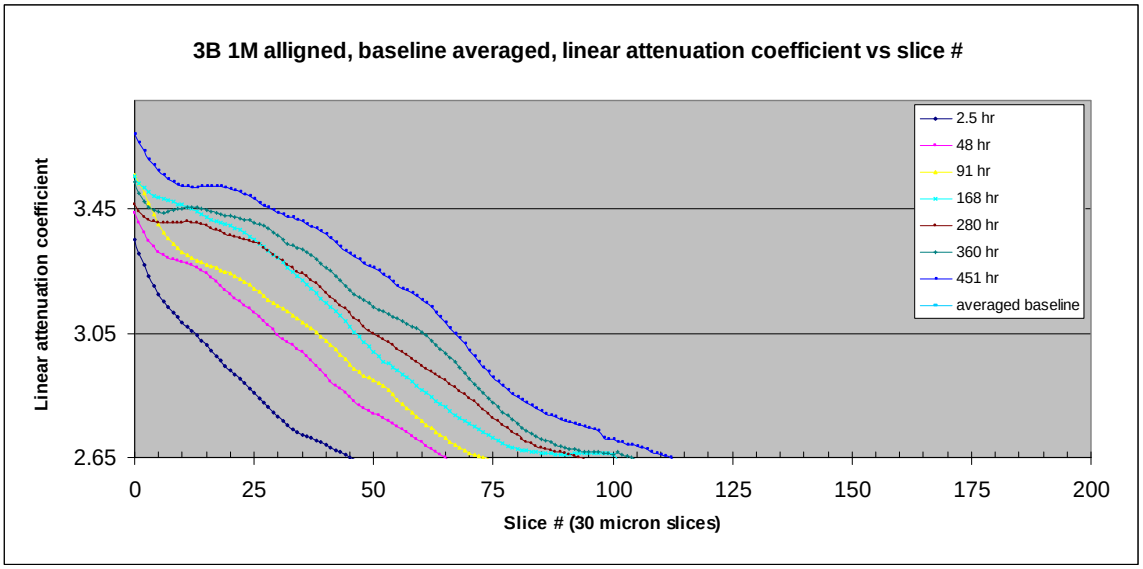

Figure 68: Sample 3B, baseline taken as 2.65 cm^{-1} for depth recalculation.

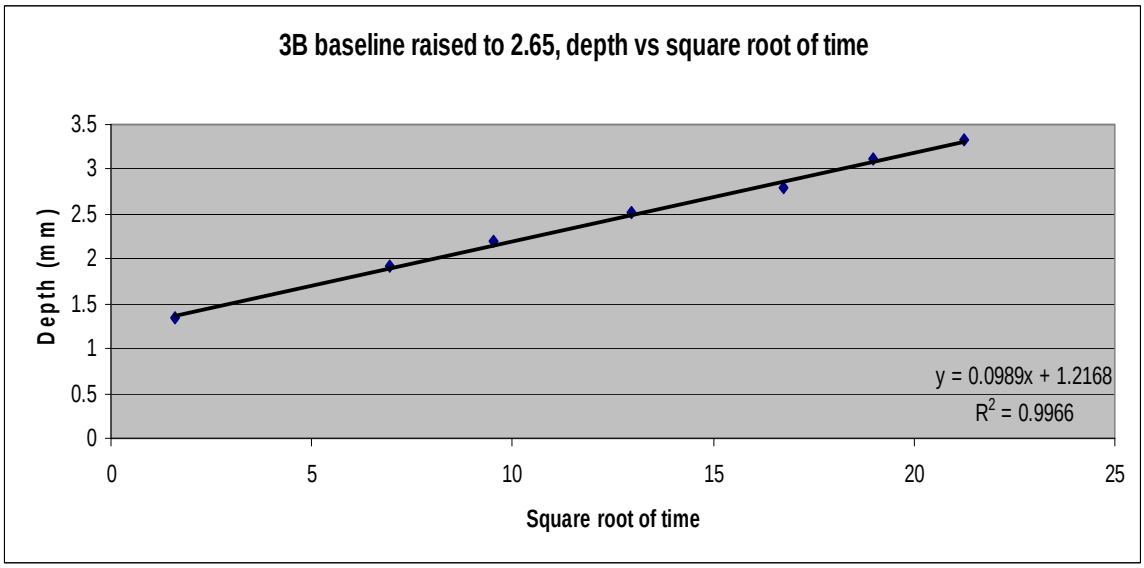

Figure 69 Intrusion front penetration (alternate method used) as a function of $t^{1/2}$ for sample 3B.

Curve Inconsistencies

On most occasions, a noted increase in the linear attenuation coefficient of the early slices was observed with time (see Figures 47and 50 above as examples). This was believed to be due to ionic migration into the less well connected pores over time, which would cause higher x-ray absorption and wider shoulders as the scans progressed in time. The width of the shoulder of the curve is believed to be directly related to the percentage of total pore space filled and concentration of contrast agent in the pores. It was also noted that for the samples run at extended times, the starting linear attenuation coefficient was lower in several cases (but the shoulder still widened), which does not agree with the previous trend of an increasing starting slice value with time. This was believed to be from loses in concentration due to evaporation to the external environment (as the Parafilm M did not provide a perfect seal), and dilution as it encountered the pore water in the sample. The evaporation loss could be minimized by an improved reservoir sealing technique, and the percent concentration loss by dilution can be minimized by using a larger KI reservoir, although this comes at the expense of shortening the cement cylinder. Once more precise samples are cut, better sealing methods, appropriate reservoir sizes, and an optimized KI molarity can be determined. From preliminary studies it appears that anything over 1.5 M is probably unnecessary even for visual examination of the images.

Figure 61 also shows an inconsistency but this is believed to have resulted from operator error. This occurred with sample 3A on the 168 hr scan. If one looks at the 168 hr scan in Figure 61 it is clear that the 168 hr intrusion curve looks out of place as its initiation point is below both the 2.5 and 91 hr scans. This does not match the observed trend shown in the other samples and runs; that higher initial attenuation readings with

occur with time progression. This is easily explained however, as after the 91 hr scan the capping Parafilm M apparently became dislodged breaking the seal, when the sample was retrieved from the environmental chamber for the 168 hr scan, the Parafilm M displayed significant salt crust on its surface. The sample was recapped with new Parafilm M and the 168 hr scan was performed. It is believed that a significant reduction in I^- concentration occurred, which would explain the abnormally low starting point for the 168 hr intrusion curve. Due to this, the old solution in the reservoir was exchanged for fresh 3M KI solution immediately after the 168 hr scan. As can be seen by Figure 61, the 216 hr and later scans returned to their expected curve initiation points, this reinforced the belief that the low initiation point of the 168 hr curve was indeed from evaporation losses which resulted in a lower iodine concentration.

Observations from 2D Image Analysis

Several things of note were observed during these experiments. Of particular interest were the intrusion patterns that could be visually seen at different depths (Figures 70A-D). These patterns clearly show that the complete sample area does not contribute to intrusion at a uniform rate. Some areas showed little to no intrusion after approximately one mm while other areas appeared to transmit contrast in an accelerated manner. Additionally it was interesting to note that while some air voids seemed open to fluid intrusion, others appeared less permeable and displayed a 'halo' of contrast around the air void. These 'halos' are evident in two places in Figure 70B. It is also interesting to observe that in Figure 70B several larger air voids are completely filled with contrast

while others contain no contrast at all. This suggests that connectivity of the air voids with the matrix pores varies considerably even in small samples. Because of this inconsistent intrusion behavior the concept of a uniform intrusion front is suspect.

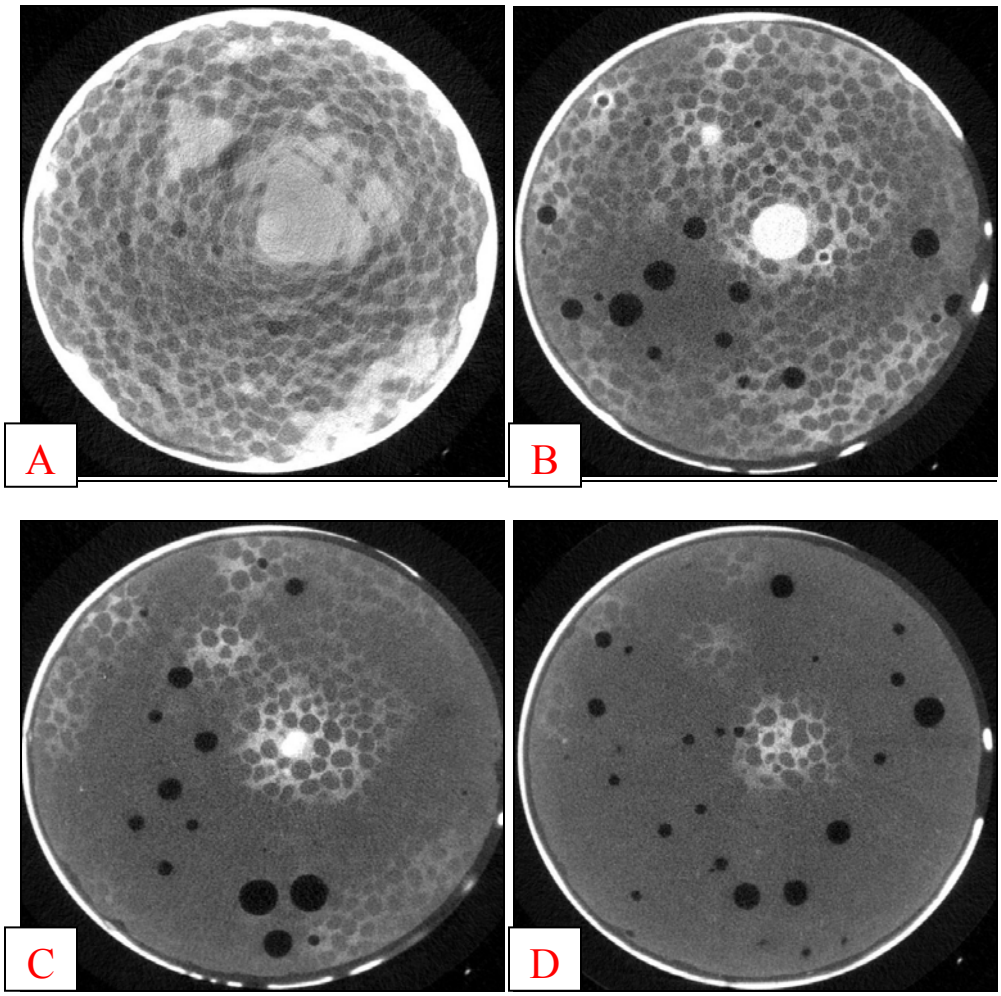

Figure 70: 2D image analysis of x-ray contrast agent intrusion as a function of depth: A) 0.9 mm, B) 1.8 mm, C) 2.4 mm and D) 3.0 mm from the intrusion surface

Fingering clearly occurs in cementitious samples. In some experimental images thin fingers of contrast were seen to penetrate as far as 50 slices deeper (1.5 mm) than an area with a large percentage of contrast intrusion. The experimental images imply that fingers of solution intrude into the sample and then a more uniform 'backfilling' front

forms behind the 'fingers'. This hypothesis is reinforced by the continuing increase in the linear attenuation coefficient for beginning slices with time.

Recommendations for Method Improvement

For the method as presented, several parameters were found to be important to the accuracy or ease of use. When preparing samples for conditioning and scanning, the surface flatness and how parallel the surface is in contact with the intruding substance is a key concern, due to slice alignment issues in the μCT. The flatter and more level the top surface is, the easier it is to align the curves and achieve accurate measurements over an ROI. For example, the initial samples were cut on a tile saw with relatively low (~1 mm) tolerances for flatness and perpendicularity to the central axis. Since the μCT scans in 30 μm slices, approximately 30 or so slices could be taken before the μCT would "cut" a level slice containing only cementitious material. These first slices might contain scans of significant amounts of air or contrast which would then bias the recorded LAC. Thus, a protocol to identify and align the first level slice within the material had to be developed. Although the developed alignment protocol was reasonably accurate, the resulting scans still injected bias, as the contrast agent might have to traverse a greater distance on one side of the sample to reach the first level slice. Although the initial intrusion is fairly rapid and the importance of this issue is debatable, the μCT method would be greatly improved if the surface flatness was maintained within a few μm and the surface levelness to the central beam could be kept to around 10 μm. If this tolerance was

achieved, the sample could be scanned with the initial slice being in pure contrast (or air, in a baseline scan) and the alignment could be made within the first few slices.

Optimization of the contrast agent concentration may yield further improvement to the technique. A reduction in molarity would decrease gradient influence and streak artifact in images, while more truly representing water intrusion. Higher concentrations could still be used for ion studies so as to match suspected concentration gradients.

The degree of baseline noise is an important factor in determining how the intrusion depth is calculated. Baseline noise and shift was one of the key factors for choosing the "steep slope" method. If the baseline noise and drift could be stabilized shallow slope methods may become more practical.

The instrument is somewhat temperature sensitive and ongoing experiments are in progress to determine the repeatability of the baseline under more uniform temperature conditions. It is believed that with more controlled room temperatures this baseline variance will decrease considerably. These initial scans were taken on a unit that was extensively, if not excessively, used and at various times of day and night. Another unit may be obtained that should reduce the workload and allow for more consistent testing conditions and thermal control. Additionally a new unit is being developed by the vendor that will have higher kVp potentials and tube current limits which should allow the unit to function more effectively; this may improve stability and reproducibility.

The motion artifact caused by loosely secured samples is an issue which can significantly affect image quality. If the sample is not securely pinned, it may shift during sample rotation causing artifacts as seen in the image in Figure 71. These artifacts need to be eliminated or minimized if crisp images are required.

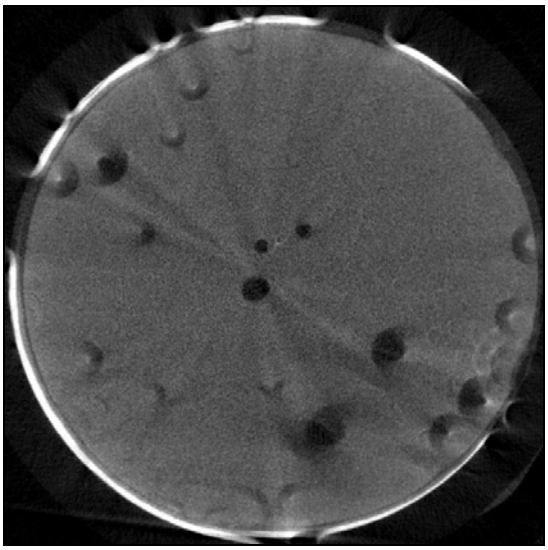

Figure 71: Motion artifact in cement sample

In our investigation a standard cortical bone, beam hardening correction was employed. This is a reasonable approximation for use with cement matrices but is not exact. According to the National Institute of Standards and Technology (NIST) cortical bone has a density of 1.92 g/cm^3 while the density of ordinary concrete is listed at approximately 2.3 g/cm^3. Since the current investigation only used these values in a relational way this was not an issue; however, a customized BHC for cementitious materials would be desirable to optimize images and more accurately represent the densities of the sample constituents.

Several things should be done to enhance this method including:

1. the design of a better sample immobilizer to prevent motion artifact,
2. the design of an air tight, durable cap for the contrast reservoir (replacing the Parafilm M) to prevent evaporation,
3. a protocol for cutting and measuring the samples to ensure levelness within a tight tolerance,

4. the optimization of the contrast agent's molarity to reduce streak artifact while still providing adequate attenuation,
5. the minimization of baseline shift and noise, due to electronics, thermal or other issues, and
6. the creation of a customized BHC.

CHAPTER VI

CONCLUSIONS

In this investigation a technique was developed utilizing μCT with a contrast agent of KI that can be used to predict intrusion depths of water and ions in a representative grout at varying levels of moisture content. The development of a μCT method utilizing contrast agent is significant, as methods to characterize the performance of high iron content cementitious materials are needed for use in critical applications such as radioactive waste disposal, stabilization, and nuclear power plant construction. Currently methods employing magnetic resonance techniques have proven unsuitable for use with high iron content cementitious materials and neutron imaging while promising does not show a wide variety of structural information, nor is it as readily available or easily implemented on a large scale.

Following scoping and "proof-of-concept" studies used to develop methods and techniques, three scenarios were used to demonstrate the method for: (i) ion intrusion into a saturated material, (ii) ion intrusion into a partially-saturated material, and (iii) water intrusion into a partially-saturated material. In all cases, the developed method was successful in clearly tracking intrusion profiles for the intruding substance. Considerations for future refinement of the method and post-analysis techniques were proposed.

REFERENCES

1. Cravens G. Power to save the world: the truth about nuclear energy. New York: Alfred A. Knopf; 2008.

2 Frame P. Radioluminescent paint [document on the Internet]. [cited 2009 Jun 26]. Availablefrom :http ://www.orau.org/ptp/collection/radioluminescent/radioluminescentinfo.htm

3 Asmus A. Early history of x-rays [document on the Internet]. [cited 2009 Jun 26]. Available from: http://www.slac.stanford.edu/pubs/beamline/25/2/25-2-assmus.pdf.

4. Kamble VB. Antoine Henri Becquerel: discovery of radioactivity [document on the Internet]. [cited 2009 Jun 27]. Available from: http://www.vigyanprasar.gov.in/scientists/AntoineHenriBecquerel.htm

5 Important moments in the history of nuclear medicine [document on the Internet]. [cited 2009 Jun 27]. Available from: http://interactive.snm.org/index.cfm?PageID=1107&RPID=924.

6. Gephart RE. Hanford: a conversation about nuclear waste and cleanup. Columbus (OH): Battelle Press; 2003.

7 Stabin MG. Radiation protection and dosimetry: an introduction to health physics. New York: Springer; 2007.

8 National Academy of Sciences, Committee on the Biological Effects of Ionizing Radiation VII. Health risks from exposure to low levels of ionizing radiation. Washington D.C.: The National Academies Press; 2006.

9. American Institute of Physics. Marie Curie: the discovery of radium [document on the Internet]. [cited 2009 Jun 27]. Available from: http://www.aip.org/history/curie/brief/03_radium/radium_3.html.

10. Adelstein DJ. Squamous cell head and neck cancer. Humara Press; 2005. p. 94.

11. Kovarik B. The radium girls [document on the Internet]. [cited 2009 Jun 26]. Available from: http://www.runet.edu/~wkovarik/envhist/radium.html.

12. Nobel Prize Organization. Biography of James Chadwick. [document on the Internet]. [cited 2009 Jun 26]. Available from: http://nobelprize.org/nobel_prizes/physics/laureates/1935/chadwick-bio.html

13. U.S. Department of Energy, Office of History and Heritage Resources. The manhattan project: the discovery of fission [document on the Internet]. [cited

2009 Jun 27]. Available from: http://www.cfo.doe.gov/me70/manhattan/discovery_fission.htm.

14. Serber R. The Los Alamos primer: the first lectures on how to build an atomic bomb. Berkeley (CA): University of California Press;1992.

15. The manhattan project: making the atomic bomb. Atomic archive [document on the Internet]. [cited 2009 Jun 27]. Available from: http://www.atomicarchive.com/History/mp/p3s1.shtml

16. Swords to plowshares: A short history of oak ridge national laboratory [document on the Internet]. [cited 2009 Jun 26]. Available from: http://www.ornl.gov/info/swords/swords.shtml.

17. Truman Library. Atomic bomb [document on the Internet]. [cited 2009 Jun 26]. Available from: http://www.trumanlibrary.org/teacher/abomb.htm.

18. United States Department of Energy. The history of nuclear energy DOE/NE-0088.

19. World Nuclear Organization. Uses of radionuclides [document on the Internet]. [cited 2009 Jun 26]. Available from: http://www.world-nuclear.org/info/inf56.html.

20. United States Congress. Atomic energy act of 1954.

21. Nuclear technologies timeline [document on the Internet]. [cited 2009 Jun 26]. Available from: http://www.greatachievements.org/?id=3691.

22. Institute of Medicine. Committee for Review and Evaluation of Medical Use Program of the Nuclear Regulatory Commision. Radiation in medicine: a need for regulatory reform. Washington D.C.:National Academy Press; 1996.

23. United States Congress. Energy Reorganization Act of 1974.

24. Becker CD. Aquatic bioenvironmental studies: the Hanford experience 1944-1984. New York: Elsevier;1990.

25. United States Congress. Resource conservation and recovery act 1976.

26. Statement on nuclear power policy. Jimmy Carter Library, Records of Speech Writer's Office. 1977 Apr 7.

27. United States Congress. Comprehensive environmental response, compensation, and liability act (CERCLA) 1980, SARA amendments 1986.

28. United States Congress. Nuclear waste policy act of 1982 as amended.

29. United States Congress. Low level radioactive waste policy act as amended 1985.

30. United States Congress. Federal facilities compliance act of 1992.

31. Usdin S. DOE lifts the plutonium veil. Nuclear Remediation Week. 1996;3(7).

32. Nuclear Energy Institute. US nuclear power generation [document on the Internet]. [cited 2009 Jun 26]. Available from: http://www.nei.org./resourcesandstats/documentlibrary/reliableandaffordableenergy/graphicsandcharts/usnucleargeneratingstatistics/.

33. United States Department of Energy. Final version dry cask storage study DOE/RW-0220.

34. Nuclear Regulatory Commission. High-level waste [document on the Internet]. [cited 2009 Jun 26]. Available from: http://www.nrc.gov/waste/high-level-waste.html.

35. US Code of Federal Regulations, Rules of general applicability to domestic licensing of byproduct material: 10CFR part 30 [document on the Internet]. [cited 2009 Jun 26]. Available from: http://www.nrc.gov/reading-rm/doc-collections/cfr/part030/.

36. Kirk B. Decommissioning and disposal options for Cs-137 blood irradiators [document on the Internet]. 2001 Sept 28 [cited 2009 Jun 26]. Available from: http://www.radjournal.com/articles/Cesium/Cesiumdisposal.htm.

37. US Code of Federal Regulations, 10 CFR 61.55 [document on the Internet]. [cited 2009 Jun 26]. Available from: http://edocket.access.gpo.gov/cfr_2003/10CFR61.55.htm.

38. Sandman P. When people are overreacting to risk [document on the Internet]. [cited 2009 Jun 26]. Available from: http://www.psandman.com/col/over-re.htm.

39. United States Department of Energy Office of Environmental Management. Low-level radioactive waste basics DOE/EM-0195.

40. Andrews A. Radioactive waste streams: waste classification for disposal. 2006. Congressional Research Service. Order code RL32163.

41. American Thyroid Association. Radioactive iodine uses for thyroid diseases [document on the Internet]. [cited 2009 Jun 26]. Available from: http://www.thyroid.org/patients/patient_brochures/radioactive.html.

42. Sodium chromate uses, fact sheet [document on the Internet]. [cited 2009 Jun 26]. Available from: http://www.nuclearonline.org/PI/bracco%20Cr-51%20doc.pdf.

43. U.S. Nuclear Regulatory Commission. The regulation and use of radioisotopes in today's world. 2000. US NRC NUREG/BR-0217 Rev 1.

44. Phillips WT, Lemen L, Goins B, Rudolph AS, Klipper R, Fresne D, Jerabek PA, Emch ME, Martin C, Fox PT, McMahan CA. Use of Oxygen-15 to measure oxygen carrying capacity of blood substitutes in vivo. American Journal of Physiology. 1997; 272 (41) . Also available from: http://ajpheart.physiology.org/cgi/reprint/272/5/H2492.pdf

45. Department of Energy. The report to the president and congress by the secretary of energy on the need for a second repository. 2008. U.S. Department of Energy. DOE/RW-0595 DEC 2008.

46. World Nuclear Organization. Waste management in the nuclear fuel cycle [document on the Internet]. 2008 Aug [cited 2009 Jun 26]. Available from: http://www.world-nuclear.org/info/inf04.html.

47. Andrews A. Congressional report for congress: nuclear fuel reprocessing: US policy development. 2008. Congressional Research Service. Order code RS22542.

48. Environmental Protection Agency. Uranium mines [document on the Internet]. 2006. [cited 2009 Jun 26]. Available from: www.epa.gov/radtown/uranium-mines.htl.

49. Uranium mill tailings. U.S. NRC Backgrounder [newsletter on the Internet]. 2006 [cited 2009 Jun 26]. Available from: http://www.nrc.gov/reading-rm/doc-collections/fact-sheets/mill-tailings.html.

50. Diehl P. Uranium mining and milling wastes: an introduction. [2004 Aug, cited 2009 Jun 26] . Available from: http://www.wise-uranium.org/uwai.html

51. United States Congress. Uranium mill tailings radiation control act of 1978 (UMTRCA).

52. Idaho State University. Depleted uranium [document on the Internet]. [cited 2009 Jun 26]. Available from: http://www.physics.isu.edu/radinf/du.htm.

53. Nuclear Regulatory Agency. Light water reactor low-enriched uranium fuel [document on the Internet]. [cited 2009 Jun 26]. Available from: http:// www.nrc.gov/materials/fuel-cycle-fac/fuel-fab.html

54. World Health Organization. Depleted uranium [document on the Internet]. [cited 2009 Jun 26]. Available from: http://www.who.int/mediacentre/factsheets/fs257/en/.

55. U.S. Department of Energy Office of Environmental Management. The current and planned low-level waste disposal capacity report revision 2. 2000.

56. United States Department of Energy. Waste isolation pilot plant. [document on the Internet]. [cited 2009 Jun 26]. Available from: http://www.wipp.energy.gov/.

57. United States Congress. The national environmental policy act of 1969, as amended (P.L. 91-190, 42 U.S.C. 4321-4347, P.L. 94-52, P.L. 94-83, P.L. 97-258).

58. George Washington University. Advisory committee staff memo prepared for advisory committee on human radiation experiments [document on the Internet]. [cited 2009 Jun 26]. Available from :http ://www.gwu.edu/~nsarchiv/radiation/dir/mstreet/commeet/meet8/brief/tab_h/br8h3.txt

59.. Nixon R. reorganization plan no. 3 of 1970. Federal Register, 35 FR 15623-15626; 1970.

60. Environmental Protection Agency. An agency for the environment [document on the Internet]. [cited 2009 Jun 26]. Available from: http://www.epa.gov/history/publications/origins6.htm.

61. Environmental Protection Agency. Summary of the clean air act [document on the Internet]. [cited 2009 Jun 26]. Available from: http://www.epa.gov/lawsregs/laws/caa.html.

62. Environmental Protection Agency. Introduction to the clean water act [document on the Internet]. [cited 2009 Jun 26]. Available from: http://www.epa.gov/watertrain/cwa/.

63. United States Congress. Federal water pollution control act a.k.a. “clean water act”. [cited 2009 Jun 26]. Available from: http://epw.senate.gov/water.pdf.

64. United States Congress. Safe drinking water act P.L. 93-523.

65. Environmental Protection Agency. Understanding the safe drinking water act [document on the Internet]. [cited 2009 Jun 26]. Available from: http://www.epa.gov/ OGWDW/sdwa/30th/factsheets/pdfs/fs_30ann_swda_web.pdf

66. Environmental Protection Agency. Mixed-waste page [document on the Internet]. [cited 2009 Jun 26]. Available at: http://www.epa.gov/rpdweb00/mixed-waste/.

67. Environmental Protection Agency. Summary of the resource conservation and recovery act [document on the Internet]. [cited 2009 Jun 26]. Available from: http://www.epa.gov/lawsregs/laws/rcra.html

68. Environmental Protection Agency. Summary of the comprehensive environmental response, compensation, and liability act [document on the Internet]. [cited 2009 Jun 26]. Available from: http://www.epa.gov/lawsregs/laws/cercla.html.

69. Environmental Protection Agency. Emergency planning and community right-to-know act [document on the Internet]. [cited 2009 Jun 26]. Available from: http://www.epa.gov/agriculture/lcra.html.

70. Colglazier EW, Langum RB. Policy conflicts in the process for siting nuclear waste repositories. Annual Review Energy. 1988;(13):317-57.

71. U.S. Department of the Interior: Bureau of Land Management. Summary of federal compliance act of 1992, P.L 102-368 [document on the Internet]. [cited 2009 Jun 26]. Available from: http://www.ntc.blm.gov/learningplace/res_FFCA.html

72. Poursaee A, Hansson CM. Potential pitfalls in assessing chloride-induced corrosion of steel in concrete. Cement and Concrete Research. 2009;(39): 391-400.

73. Cano F. de J, Bremner TW, McGregor RP, Balcom BJ. Magnetic resonance imaging of ^{1}H, 23Na, and 35Cl penetration in Portland cement mortar. Cement and Concrete Research. 2002;(32):1067-70.

74. Glasser F, Marchand J, Samson E. Durability of concrete: degradation phenomena involving detrimental chemical reactions. Cement and Concrete Research. 2008;(38): 226-46.

75. Mu R, Miao C, Luo X, Sun W. Interaction between loading, freeze-thaw cycles, and chloride salt attack of concrete with and without steel fiber reinforcement. Cement and Concrete Research. 2002;(32):1061-66.

76. Hall C, Hoff W. Water transport in brick, stone and concrete. London and New York: Spon press; 2002.

77. Jaffer SJ, Hansson CM. Chloride-induced corrosion products of steel in cracked-concrete subjected to different loading conditions. Cement and Concrete Research. 2009; (39):116-25.

78. Trejo D, Monteiro PJ. Corrosion performance of conventional (ASTM A615) and low-alloy (ASTM A706) reinforcing bars embedded in concrete and exposed to chloride environments. Cement and Concrete Research. 2005; (35):562-71.

79. Poupard O, L'Hostis V, Catinaud S, Petre-Lazar I. Corrosion damage diagnosis of a reinforced concrete beam after 40 years natural exposure in marine environment. , Cement and Concrete Research. 2006;(36):504-20.

80. Shanahan N, Zayed A. Cement composition and sulfate attack part I. Cement and Concrete Research. 2007; (37):618-23.

81. Zuquan J, Wei S, Yunsheng Z, Jinyang J, Jianzhong L, Interaction between sulfate and chloride solution attack of concretes with and without flyash. Cement and Concrete Research.2007; (37):1223-32.

82. Hekala EE, Kishar E, Mostafa H,.Magnesium sulfate attack on hardened blended cement pastes under different circumstances. Cement and Concrete Research. 2002;(32):1421-7.

83. Dow C, Glasser FP. Calcium carbonate efflorescence on Portland cement and building materials. Cement and Concrete Research. 2003;(33):147-54.

84. Sanchez F, Gervais C, Garrabrants AC, Barna R, Kosson DS. Leaching of inorganic contaminants from cement-based waste materials as a result of carbonation during intermittent wetting. Waste Management. 2002;(22):249-60.

85. Gummerson RJ, Hall C, Hoff WD. Unsaturated water flow within porous materials observed by NMR imaging. Nature. 1979; (281).

86. Pel L, Kazrati LK, Kopinga K, Marchland J. Water absorption in mortar determined by NMR. Magnetic Resonance Imaging. 1998;16(5/6): pp 525-8.

87. Feng X, Balcom BJ, Thomas MA, Bremner TW. Na and Li ion diffusion in modified ASTM C 1260 test by magnetic resonance imaging (MRI). Cement and concrete research. 2008;(38):1409-15.

88. Lura P, Bentz DP, Lange DA, Kovler K, Bentur A, Breugel KV. Measurement of water transport from saturated pumice aggregates to hardening cement paste. Materials and Structures. 2006; 39(9):861-8.

89. Bentz DP, Hansen KK. Preliminary observations of water movement in cement pastes during curing using X-ray absorption. Cement and Concrete Research. 2000;(30): 1157-68.

90. Henkensiefken R, Briatka P, Bentz D, Nantung T, Weiss J. Plastic shrinkage cracking in internally cured mixtures made with pre-wetted lightweight aggregate.

NIST; [cited 2009 Jun 26]. Available from: http://ciks.cbt.nist.gov/~bentz/LWAplasticshrinkagepaper.pdf

91. Kroning M, Jentsch T, Maisl M, Reiter H. Non-destructive testing and process control using x-ray methods and radioisotopes. QNET [document on the Internet]. [cited 2009 Jun 26]. Available from: http://www.qnetworld.com/pdfs/X-ray%20NDT.pdf

92. Kaufmann J, Studer W. One-dimensional water transport in covercrete-application of non-destructive methods. Materials and Structures. 1995; 28(2): 115-24.

93. Hoff WD, Wilson MA, Benton DM, Hawkesworth MR, Parker DJ, Fowles P. The use of positron emission tomography to monitor unsaturated water flow within porous construction materials. Journal of Materials Science Letters. 1996; (15):1101-4.

94. de Beer FC, Middleton MF. Neutron radiography imaging, porosity and permeability in porous rocks. South African Journal of Geology. 2006; 109(4):541-50.

95. Pel L, Ketelaars AAJ, Adan OCG, Van Well AA. Determination of moisture diffusivity in porous media using scanning neutron radiography. International Journal of Mass Tranfer. 1993; 36(5): 1261-7.

96. Synchrotron Radiation. All physics [document on the Internet]. [cited 2009 Jun 26]. Available from: http://all-physics.net.

97. Synchrotron Radiation. Hyper physics [document on the Internet]. [cited 2009 Jun 26]. Available from: http://hyperphysics.phy-astr.gsu.edu/hbase/particles/synchrotron.html.

98. Radiology Rounds PET /CT for Tumor Imaging. Radiology Rounds Massachusetts General Hospital [newsletter on the Internet]. 2004 May [cited 2009 Jun 26]; Available from: http://www.massgeneralimaging.org/newsletter/may_2004/may_2004.pdf.

99. Bodansky D. Nuclear energy: principles practices and prospects. 2cd ed. New York: Springer; 2004.

100. Knoll G. Radiation detection and measurement 3rd ed. NY: Wiley and Sons; 2000.

101. Badawi R. University of Washington Department of Nuclear Medicine. Introduction to PET physics [document on the Internet]. [updated 1999 Jan 12; cited 2009 Jun 26]. Available from: http://depts.washington.edu/nucmed/IRL/pet_intro/intro_src/section2.html.

102. Hendee WE, Ritenour R. Medical Imaging Physics 4th edition. New York (NY): Wiley-Liss; 2002.

103. Bruce RR, Klute A. Proc. Soil Sci. Soc. Amer. 1956; (20):458.

104. Turkington TG. Introduction to PET instrumentation. Journal of Nuclear Medicine Technology. 2001; 29(1): 4-11.

105. Basic Nuclear Magnetic Resonance. Simply Physics [document on the Internet]. [cited 2009 June 26]; Available from: http://www.simplyphysics.com/page2_1.html

106. Kalliopi K. Aligizaki . Pore structure of cement-based materials: testing interpretation and requirements, New York: Taylor and Francis; 2006. p. 219.

107. Zhang, J, Chou C, Jensen T, Gray J. Development of a high resolution 3D computed tomography system: data acquisition, reconstruction and visualization. Masters Thesis. Ames (IA): Iowa State University; 2003.

108. Seol Y, Kneafsey T. Fluid flow through heterogeneous methane hydrate-bearing sand: Observations using x-ray CT scanning, In: Proceedings of the 6th International Conference on Gas Hydrates (ICGH 2008); 2008 July 6-10; Vancouver, Canada

109. Partial volume averaging. Medcyclopaedia [online technical/medical resource]. [cited 2009 Jun 26]. Available from: http://www.medcyclopaedia.com/library/topics/volume_i/p/partial_volume_averaging.aspx.

110. Optiray 320 [document on the Internet]. [cited 2009 Jun 26]. Available from: http://www.drugs.com/pro/optiray.html.

111. Glasser FP. Fundamental aspects of cement solidification and stabilization. Journal of Hazardous Materials. 1997;52(2-3);151-70.

112. Crank J. The mathematics of diffusion 2cd ed. Oxford: Clarendon Press;1975. p 37.

113. Diamond S. The patch microstructure in concrete: effect of mixing time. Cement and Concrete Research. 2005;(35) :1014-6.

References for Figures

Figure 1. Aurora Borealis by Terry Lutz [photo available on the Internet]. [cited 2009 Jun 27]. Available from: http://einstein.stanford.edu/highlights/sb4-111204-aurora-lutz.jpg.

Figure 2. Minutes count Oak Ridge billboard by James Westcott [photo available on the Internet].[cited 2009 Jun 26]. Available from: http://www.amse.org.

Figure 3. 1920's breast brachytherapy [photo available on the Internet]. [cited 2009 Jun 27]. Available from: http://radonc.ucsd.edu/PatientInformation/history.asp.

Figure 4. Fission discovery cartoon [image available on the Internet]. [cited 2009 Jun 27]. Available from: http://www.cfo.doe.gov/me70/manhattan/adventures_atom.htm#8

Figure 5. USS Nautilus SSN 571, first nuclear powered submarine [photo available on the Internet]. [cited 2009 Jun 27]. Available from: http://pictopia.com/perl/get_image?provider_id=319&size=550x550_mb&ptp_photo_id=312458.

Figure 6. Engineered liner at a CERCLA facility [image on the Internet]. [cited 2009 Jun27]. Available from: http://www.doedigitalarchive.doe.gov/enter.cfm

Figure 7. NaI I-131 gel capsules for thyroid therapy [photo available on the Internet]. [cited 2009 Jun 27]. Available from: http://imaging.covidien.com/imageServer.aspx/doc133546.jpg?contentID=8012&contenttype=image/jpeg.

Figure 8. 20 year tritium exit sign [photo on the Internet]. [cited 2009 Jun 26]. Available from: http://www.tritiumexitsigns.com.

Figure 9. Fission fragment distribution [image on the Internet]. [cited 2009 Jun 27]. Available from : http ://www.kayelaby.npl.co.uk/atomic_and_nuclear_physics/4_7/4_7_1.html.

Figure 10. Diagram of in situ leaching for uranium [image on the Internet]. [cited 2009 Jun 27]. Available from: http://www.uraniuminfo.org/files/images/Diagram%20of%20In%20Situ%20mine.inline.jpg.

Figure 11. Uranium mill tailings sites [image on the Internet]. [cited 2009 Jun 27]. Available from: http://www.nrc.gov.

http ://depts.washington.edu/nucmed/IRL/pet_intro/intro_src/section2.html.

Figure 26. Types of coincidence [image on the Internet]. [cited 2009 Jun27]. Available from: http://depts.washington.edu/nucmed/IRL/pet_intro/intro_src/section2.html

Figure 27. One photon being detected in 3 detectors [image on the Internet]. [cited 2009 Jun 27]. Available from: http://tech.snmjournals.org/cgi/content/full/29/1/4.

Figure 28. Top exhibiting rotation, precession, and the angle of precession [image on the Internet]. [cited 2009 Jun 27]. Available from:http://www.papimi.gr/NMR.htm.

Figure 29. Magnetic moments before and after a strong magnetic field is applied [image on the Internet]. [cited 2009 Jun 27]. Available from: http://www.easymeasure.co.uk/webs/3/html/510/fig2.gif.

Figure 30. Precession in parallel and antiparallel states [image on the Internet]. [cited 2009 Jun 27]. Available from: http://www.easymeasure.co.uk/principlesmri.aspx.

Figure 31. Tipping of bulk magnetization into xy plane [image on the Internet]. [cited 2009 Jun 27]. Available from: http://www.simplyphysics.com/page2_4.html.

Figure 32. Emission of radiofrequency [image on the Internet]. [cited 2009 Jun 27]. Available from: http://www.simplyphysics.com/page2_1.html.

Figure 33. How microCT takes an image [image on the Internet]. [cited 009 Jun 27]. Available from: http://www.skyscan.be/company/methods.htm.

Figure 34. Penumbra caused by finite sized focal spot. Drawn by author.

Figure 35. Cores and core-bit. Taken by author.

Figure 36. Plastic pour box. Taken by author.

Figure 37. Small sample book-mold. Taken by author.

Figure 38. Vacuum apparatus. Taken by author.

Figure 39. Scanco μCT 40. Taken by author.